

AD-A246 437



# NAVAL POSTGRADUATE SCHOOL

## Monterey, California

2



DTIC  
ELECTE  
FEB 26 1992  
S B D

## THESIS

**OBSERVATIONS OF WIND FORCED  
CIRCULATION ON THE CONTINENTAL  
SHELF OFF POINT SUR, CALIFORNIA FROM  
A SELF-CONTAINED ACOUSTIC DOPPLER  
CURRENT PROFILER**

by

Christopher Lynn Abbott

December 1991

Thesis Advisor: Steven R. Ramp

Approved for public release; distribution is unlimited.

92 04585

92-04585



Unclassified

SECURITY CLASSIFICATION OF THIS PAGE

## REPORT DOCUMENTATION PAGE

1. REPORT SECURITY CLASSIFICATION Unclassified		1b. RESTRICTIVE MARKINGS	
2. SECURITY CLASSIFICATION AUTHORITY		3. DISTRIBUTION/AVAILABILITY OF REPORT Approved for public release; distribution is unlimited.	
4. DECLASSIFICATION/DOWNGRADING SCHEDULE		5. MONITORING ORGANIZATION REPORT NUMBER(S)	
6. PERFORMING ORGANIZATION REPORT NUMBER(S)		7a. NAME OF MONITORING ORGANIZATION Naval Postgraduate School	
7. NAME OF PERFORMING ORGANIZATION Naval Postgraduate School	6b. OFFICE SYMBOL (If Applicable)	7b. ADDRESS (city, state, and ZIP code) Monterey, CA 93943-5000	
8. ADDRESS (city, state, and ZIP code) Monterey, CA 93943-5000	6c. OFFICE SYMBOL (If Applicable)	9. PROCUREMENT INSTRUMENT IDENTIFICATION NUMBER	
10. NAME OF FUNDING/SPONSORING ORGANIZATION	10a. SOURCE OF FUNDING NUMBERS	10b. WORK UNIT ACCESSION NO.	
10c. ADDRESS (city, state, and ZIP code)	10d. PROGRAM ELEMENT NO.	10e. PROJECT NO.	10f. TASK NO.
11. TITLE (Include Security Classification) OBSERVATIONS OF WIND FORCED CIRCULATION ON THE CONTINENTAL SHELF OFF POINT SUR, CALIFORNIA FROM A SELF-CONTAINED ACOUSTIC DOPPLER CURRENT PROFILER			
12. PERSONAL AUTHOR(S) ABBOTT, CHRISTOPHER, L.			
13a. TYPE OF REPORT Master's Thesis	13b. TIME COVERED FROM TO	14. DATE OF REPORT (year, month, day) December 1991	15. PAGE COUNT 105
16. SUPPLEMENTARY NOTATION The views expressed in this thesis are those of the author and do not reflect the official policy or position of the Department of Defense or the U.S. Government.			
17. COSATI CODES		18. SUBJECT TERMS (continue on reverse if necessary and identify by block number)	
17a. FIELD	17b. GROUP	SC-ADCP, acoustic velocity profiler, coastal upwelling, Ekman layer, California Current, coastal circulation	
17c. SUBGROUP			
19. ABSTRACT (Continue on reverse if necessary and identify by block number)			
<p>To study the current structure of the California Current as it manifests itself on the continental shelf a subsurface mooring, P1, was anchored 5 km west of Point Sur at 36° 17' N, 121° 59' W from 28 February through 11 May 1990. The P1 mooring, placed on the 84 m isobath, consisted of a Self-Contained Acoustic Doppler Current Profiler (SC-ADCP) housed in a syntactic foam sphere and secured to an anchor. The mooring geometry placed the transducer heads at 80 m depth. The instrument operated at 307 Hz with each beam inclined 30° from the vertical. An ensemble average of 170 one-second pings were recorded every 15 minutes for 10 days. Good velocity data to within 15 m of the surface were obtained at 4 m intervals throughout the record.</p> <p>Low-pass filtered data indicate high coherence between the observed currents and the local wind forcing measured at the Monterey Bay NOAA buoy located 53 km to the northwest. During equatorward wind events the current response was vertically sheared and time-lagged at depth with near surface speeds up to 35 cm s<sup>-1</sup>. During wind relaxations (periods of no wind) and poleward winds a pressure induced barotropic poleward flow, on the order of 10 cm s<sup>-1</sup>, developed throughout the water column. These poleward currents became more frequent and better developed later in the record. Analysis of adjusted sea level (ASL) differences between</p>			
20. DISTRIBUTION/AVAILABILITY OF ABSTRACT <input checked="" type="checkbox"/> UNCLASSIFIED/UNLIMITED <input type="checkbox"/> DTIC USERS <input type="checkbox"/> SAME AS		21. ABSTRACT SECURITY CLASSIFICATION Unclassified	
22a. NAME OF RESPONSIBLE INDIVIDUAL Steven R. Ramp		22b. TELEPHONE (Include Area Code) 408 646-3162	22c. OFFICE SYMBOL OC/Ra

DD FORM 1473, 84 MAR

83 APR edition may be used until exhausted

SECURITY CLASSIFICATION OF THIS PAGE

All other editions are obsolete

Unclassified

Inclassified

Security Classification of this page

Line # 19 Continued

ations located to the north and south of mooring P1 suggest an increasing poleward pressure gradient during the span of the record. Alongshore differences in the alongshore wind stress component contributed to the increasing difference in ASL.

A simple wind forced theoretical model adapted from Ekman (1905) and Csanady (1982), was used to describe the flow in the coastal regime. The model consists of surface and bottom boundary layers superimposed on a mostly geostrophic interior flow driven by set-up and set-down of the sea surface near the coast. The magnitude, direction, and sense of rotation of the current vectors with depth were reproduced well by the model when it was forced by the actual magnitude of the surface wind stress and a realistic vertical eddy coefficient ( $A_z$ ). Differences between the model and the observations can be accounted for by other elements of the coastal circulation not included in the model.

S/N 0102-LF-014-6601

Security Classification of this page

Unclassified

Approved for public release; distribution is unlimited.

Observations of Wind Forced Circulation on the Continental Shelf off  
Point Sur, California from a Self-Contained Acoustic Doppler Current  
Profiler

by

Christopher Lynn Abbott  
Lieutenant, United States Navy  
B.S., Virginia Military Institute, 1982

Submitted in partial fulfillment of the requirements for  
the degree of

MASTER OF SCIENCE IN METEOROLOGY AND  
PHYSICAL OCEANOGRAPHY

from the

NAVAL POSTGRADUATE SCHOOL  
December 1991

Author:

*Christopher L. Abbott*  
Christopher Lynn Abbott

Approved by:

*Steven R. Ramp*  
Steven R. Ramp, Thesis Advisor

*P. C. Chu*  
P.C. Chu, Second Reader

*Curtis A. Collins*  
Curtis A. Collins, Chairman, Department of Oceanography

iii



Accession For	
NTIS GRA&I	<input checked="checked" type="checkbox"/>
DTIC TAB	<input type="checkbox"/>
Unannounced	<input type="checkbox"/>
Justification	
By	
Distribution/	
Availability Codes	
Avail and/or	
Dist	Special
A-1	

## ABSTRACT

To study the current structure of the California Current as it manifests itself on the continental shelf a subsurface mooring, P1, was anchored 5 km west of Point Sur at  $36^{\circ} 17' \text{ N}$ ,  $121^{\circ} 59' \text{ W}$  from 28 February through 11 May 1990. The P1 mooring, placed on the 84 m isobath, consisted of a Self-Contained Acoustic Doppler Current Profiler (SC-ADCP) housed in a syntactic foam sphere and secured to an anchor. The mooring geometry placed the transducer heads at 80 m depth. The instrument operated at 307 kHz with each beam inclined  $30^{\circ}$  from the vertical. An ensemble average of 170 one-second pings were recorded every 15 minutes for 70 days. Good velocity data to within 15 m of the surface were obtained at 4 m intervals throughout the record.

Low-pass filtered data indicate high coherence between the observed currents and the local wind forcing measured at the Monterey Bay NOAA buoy located 53 km to the northwest of P1. During equatorward wind events the current response was vertically sheared and time-lagged at depth with near surface magnitudes up to  $35 \text{ cm s}^{-1}$ . During wind relaxations (periods of no wind) and poleward winds a pressure induced barotropic poleward flow, on the order of  $10 \text{ cm s}^{-1}$ , developed throughout the water column. These poleward currents became more frequent and better developed later in the record. Analysis of adjusted sea level (ASL) differences between stations located to the north and south of mooring P1 suggest an increasing poleward pressure gradient during the span of the record. Alongshore differences in the alongshore wind stress component contributed to the increasing difference in ASL.

A simple wind forced theoretical model adapted from Ekman (1905) and Csanady (1982), was used to describe the flow in the coastal regime. The model

consists of surface and bottom boundary layers superimposed on a mostly geostrophic interior flow driven by set-up and set-down of the sea surface near the coast. The magnitude, direction, and sense of rotation of the current vectors with depth were reproduced well by the model when it was forced by the actual magnitude of the surface wind stress and a realistic vertical eddy coefficient ( $A_z$ ). Differences between the model and the observations can be accounted for by other elements of the coastal circulation not included in the model.

## TABLE OF CONTENTS

<b>I</b>	<b>INTRODUCTION .....</b>	<b>1</b>
A.	THE CALIFORNIA CURRENT SYSTEM.....	1
B.	COASTAL UPWELLING .....	3
C.	PAST STUDIES .....	5
1.	Coastal Oceans Dynamics Experiment (CODE).....	5
2.	The Central California Coastal Circulation Study (CCCS).....	7
D.	PURPOSE OF STUDY.....	8
<b>II</b>	<b>DATA COLLECTION.....</b>	<b>10</b>
A.	PRINCIPALS OF OPERATION.....	10
1.	The SC-ADCP and mooring geometry.....	10
2.	Velocity calculation .....	10
B.	INSTRUMENT CONFIGURATION .....	12
C.	ERROR ANALYSIS .....	13
1.	Bias and random error .....	13
2.	Sound speed difference at transducer.....	14
3.	Conversion to earth coordinates .....	14
D.	DATA VELOCITY CHECKS .....	15
1.	Echo Amplitude.....	15
2.	Percent Good.....	18
<b>III</b>	<b>SUPPLEMENTAL DATA SETS .....</b>	<b>20</b>
A.	WIND STRESS DATA.....	20
B.	HYDROGRAPHIC DATA .....	22
C.	SYNTHETIC SUBSURFACE PRESSURE .....	22
<b>IV.</b>	<b>DATA PROCESSING.....</b>	<b>24</b>
A.	DATA FILTERING .....	24
B.	SPECTRAL ANALYSIS .....	26

<b>V. OBSERVATIONS.....</b>	<b>29</b>
A. SPATIAL AND TEMPORAL CHARACTERISTICS.....	29
B. EQUATORWARD EVENTS.....	34
C. POLEWARD EVENTS.....	40
D. COHERENCE AND PHASE.....	43
<b>VI THEORETICAL MODEL.....</b>	<b>48</b>
A. GOVERNING EQUATIONS.....	50
1. Surface Component.....	52
2. Interior Component.....	56
3. Bottom Component.....	65
4. Solutions.....	66
B. RESULTS.....	67
<b>VII. DISCUSSION.....</b>	<b>77</b>
A. MODEL RESULTS.....	77
1. Features.....	77
2. Causative factors for observed model discrepancies.....	77
a. Slight baroclinic effects and variable $A_z$ .....	78
b. Nonuniform wind stress.....	78
c. Bathymetric considerations.....	78
d. Remote influences.....	79
B. ANOMALOUS EQUATORWARD WIND EVENTS.....	80
1. Poleward pressure gradient.....	82
2. Alongshore variability in the alongshore wind stress.....	82
<b>VIII. CONCLUSIONS AND RECOMMENDATIONS.....</b>	<b>87</b>
A. CONCLUSIONS.....	87
B. RECOMMENDATIONS.....	88
<b>REFERENCES.....</b>	<b>90</b>
<b>INITIAL DISTRIBUTION LIST.....</b>	<b>94</b>



## LIST OF FIGURES

Figure 1. Geographical position of seasonal atmospheric high (H) and low (L) pressure systems over the eastern North Pacific and the west coast of North America.....	2
Figure 2. Schematic of two dimensional upwelling.....	4
Figure 3. Chart of the California coast off Point Sur locating the mooring positions of moorings P1, P2, P3.....	9
Figure 4. SC-ADCP configuration and P1 mooring geometry.....	11
Figure 5. Time series of heading, pitch, and roll from the SC-ADCP.....	16
Figure 6. SC-ADCP echo amplitude and percent good.....	17
Figure 7. SC-ADCP transducer beam characteristics.....	19
Figure 8. Chart of the California coast indicating geographic positions of NOAA buoys and tide stations.....	21
Figure 9. Example of filtering technique.....	25
Figure 10. Time series, in stick vector format, of the low-passed filtered local wind stress.....	30
Figure 11. Time series of v current component.....	32
Figure 12. Time series of u current component.....	33
Figure 13. Time series of vertical shear for v current component.....	35
Figure 14. Time series of vertical shear for u current component.....	36
Figure 15. Daily averaged equatorward wind forced current profiles in component format.....	38
Figure 16. Daily averaged equatorward wind forced current profiles in hodograph format.....	39
Figure 17. Daily averaged wind relaxation current profiles in component format.....	41
Figure 18. Daily averaged wind relaxation current profiles in hodograph format.....	42
Figure 19. Coherence between the alongshore component of the wind stress ( $\tau_y$ ) and the u and v current components.....	45
Figure 20. Coherence and phase between v current components at increasing depths.....	46
Figure 21. Coherence and phase between u current components at increasing depths.....	47

Figure 22. CTD surveys of site P1.....	49
Figure 23. Theoretical dynamic coastal current regime accompanying alongshore wind.....	51
Figure 24. Coastal transport schematic.....	61
Figure 25. Theoretical current structure.....	68
Figure 26. Theoretical current vs observed current .....	69
Figure 27. Solutions to governing equations utilizing variations of eddy viscosity ( $A_z$ ).....	71
Figure 28. Theoretical current structure.....	72
Figure 29. Theoretical current vs observed current .....	74
Figure 30. Theoretical current vs observed current .....	75
Figure 31. Theoretical current vs observed current hodographs .....	76
Figure 32. Time series showing equatorward wind stress events .....	81
Figure 33. $\Delta$ SSP vs wind stress .....	83
Figure 34. Alongshore component of the wind stress at Monterey Bay and the wind stress at Santa Maria.....	85
Figure 35. $\partial\tau_y/\partial y$ vs $\Delta$ SSP.....	86

## ACKNOWLEDGMENTS

The completion of this research project can be attributed to very hard work and the help and unwavering support of several individuals. My advisor, Dr. Steven Ramp, spent many hours with me as I worked through the theory and its physical implications involved in this study. He gave me a real appreciation of how demanding research work can be. My second reader, Dr. Pcheng Chu, provided me with insight on several particularly difficult concepts which aided greatly to my understanding. Technical support was provided by Mr. Todd Anderson who assisted me in mastering the VAX computer and in processing the seemingly endless SC-ADCP data set. I also would like to thank Mr. Paul Jessen who helped me with the never ending Fortran codeing questions and sometimes short notice graphical support.

## II. INTRODUCTION

### A. THE CALIFORNIA CURRENT SYSTEM

The California Current System (CCS), an eastern boundary current system, is characterized by a flow that is highly variable both temporally and spatially. The CCS is composed of the following components: the California Current (CC), the California Undercurrent (CUC), the Davidson Current (DC) and the Southern California Counter Current (SCCC). The CC, comprising the eastern limb of the north Pacific anticyclonic gyre, flows along the west coast of the United States and is characterized by predominantly equatorward mean flow with velocities on the order of  $1\text{-}10\text{ cm s}^{-1}$ . The majority of the equatorward transport occurs within 1000 km of the coast with the current reaching from the surface down to 300 m depth (Hickey, 1979). Flow over the continental shelf tends to be highly variable with equatorward and poleward surface currents superimposed on the mean flow (Chelton, 1984). At depths greater than 100 m, on the continental slope, the CUC is present throughout the year and consists of a poleward component with seasonally averaged velocities on the order of  $10\text{ cm s}^{-1}$  (Chelton, 1984) and maxima up to  $40\text{ cm s}^{-1}$  (Tisch, 1990). Only present in the fall and winter months, the DC is a poleward surface current north of Point Conception occurring within 80 km of the coast with a magnitude on the order of  $10\text{ cm s}^{-1}$  (McCreary et al., 1987). The companion to the DC is the SCCC which is also poleward and encompasses the area south of Point Conception (Hickey, 1979). The CCS is generated by large scale atmospheric forcing between the north Pacific high and the continental thermal low over the southwest U. S. The seasonal variation of

the winds is evident in Figure 1. The high pressure migrates from its most southerly position of  $30^{\circ}$  N,  $135^{\circ}$  W in the winter months to its most northerly position  $38^{\circ}$  N,  $145^{\circ}$  W in the summer. There is a corresponding building of the high in the summer months (1020 mb in November to 1025 mb in August). The low pressure over the southwest portion of the U. S. does not tend to migrate seasonally, however, there is a deepening in the summer months due to warming of the land (Huyer, 1983). The pressure gradient associated with these features then will also exhibit seasonal variation.

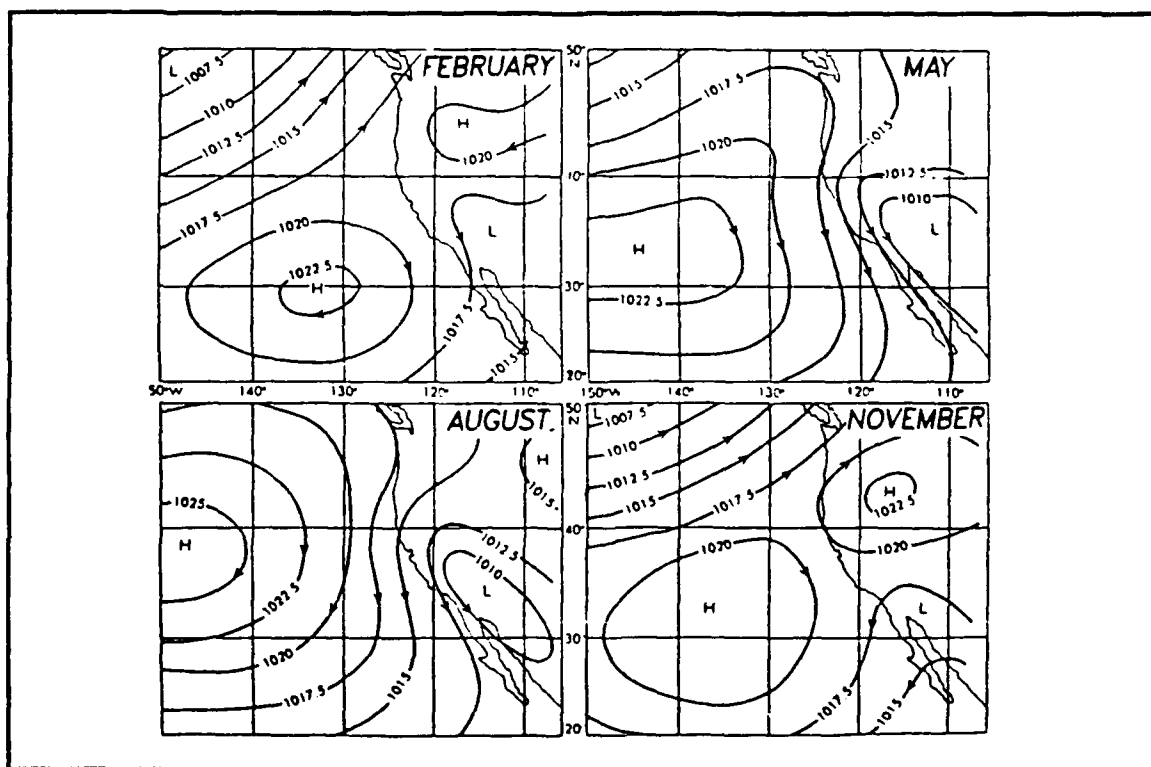


**Figure 1.** Geographical position of seasonal atmospheric high (H) and low (L) pressure systems over the eastern North Pacific and the west coast of North America. Isoheight pressure levels are contoured with the direction of flow indicated by arrows. Pressure is measured in mb (from Reid et al., 1958).

As the pressure gradient manifests itself by the wind field, in the summer months south of 40° N winds are generally steady, equatorward, and highly coherent in the alongshore direction (Chelton, 1984).

Steady equatorward winds produce offshore flow via the Ekman transport which generates dynamic sea level height differences perpendicular to the coast. This results in a geostrophically balanced surface flow parallel to the coast located typically within 5 - 25 km from the coast which typically encompasses the internal Rossby radius of deformation (Hickey, 1979). Since variations in the current regime respond to local wind forcing, changes can occur rapidly (on the order of days). The magnitude of the wind forcing is strongest approximately 200 km off shore. As a result, positive wind stress curl ( $\text{curl } \tau$ ) is present in the near shore region (Nelson, 1977), and may be important in driving poleward flow (McCreary et al., 1987).

## **B. COASTAL UPWELLING**

Coastal upwelling occurs seasonally along the entire west coast of the U. S. and is the result of equatorward winds generating offshore Ekman transport away from the coast (Huyer, 1983). Most of the knowledge regarding the structure and dynamics of the active upwelling zone is limited to a coastal strip a few tens of kilometers wide (Huyer, 1983). To help illustrate the dynamics of coastal upwelling circulation on the continental shelf a conceptual two dimensional model (no alongshore variation) is presented (Figure 2). Equatorward winds drive surface water off-shore in the Ekman layer. Below this layer, a compensating return drift is generated to conserve volume. This return flow will then surface in a band near shore. Near the surface, the surfacing thermocline produces a baroclinic jet, whose vertical shear is geostrophically

balanced by the across-shore density gradients induced by upwelling (Kosro, 1987). At greater depths there is a reversal of the along-shore currents, a poleward undercurrent, which flows counter to the wind (Kosro, 1987)

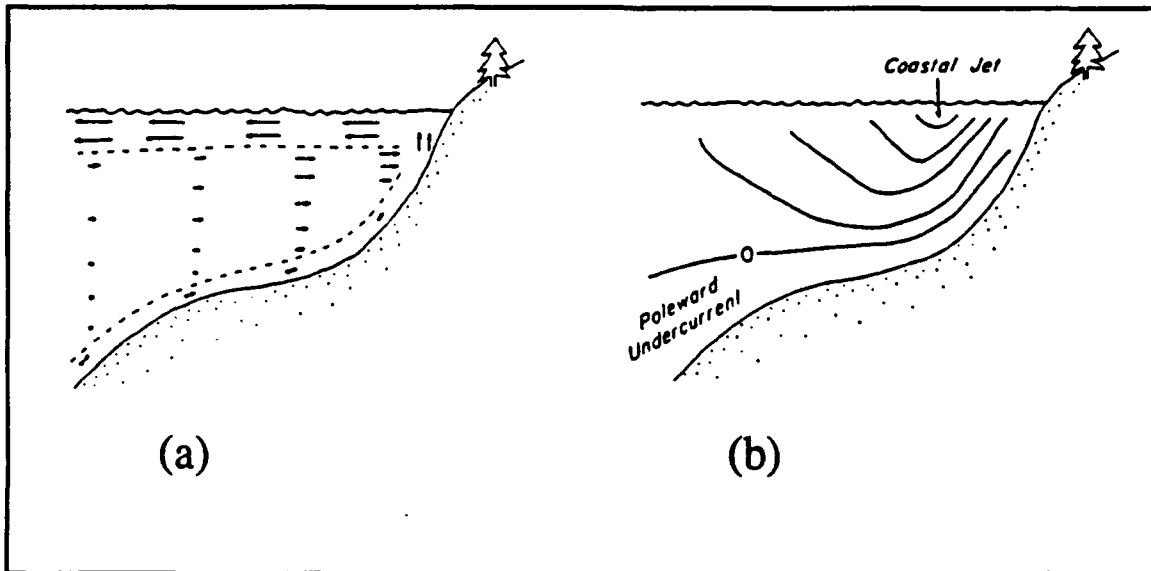


**Figure 2. Schematic of two dimensional upwelling.** (a) This figure represents the cross-shore ( $u$ ) component of flow. Current speed and direction are indicated by vectors. The surface and bottom Ekman layers are indicated by dashed lines. (b) This figure represents the alongshore ( $v$ ) component of flow. Velocity contours are indicated with equatorward flow occurring in the surface layers and a poleward undercurrent present near the sea floor (from Huyer, 1983).

In contrast to the two dimensional schematic, which is useful in describing the upwelling concept, in many applicable flow regimes it appears that coastal upwelling is always a three dimensional process (Brink, 1983), imposed by basin geometry or by external forcing imposed on a large scale. This results in certain areas ("upwelling centers") near coastal promontories where upwelling appears to be more vigorous than others. Based on satellite imagery (Tisch, 1990), Point Sur may act as an upwelling center.

### C. PAST STUDIES

Extensive study in the large scale circulation of the CCS was initiated in 1949 by the California Cooperative Fisheries Investigation (CalCOFI) to examine the ecosystem of the southern portion of the CCS (Chelton et al., 1988). An important aspect of this CalCOFI study was the maintenance of a geographically fixed sampling grid to take hydrographic surveys. This sampling grid consisted of parallel lines oriented perpendicular to the coast and covered a region from San Francisco to Southern Baja. With a typical cross-shelf grid spacing of 74 km, large-scale low-frequency variability in the current structure is well addressed (Chelton et al., 1988). However, detailed temporal and spatial analysis of smaller scale high-frequency events occurring along the coastal regions cannot be obtained from this study.

#### 1. Coastal Oceans Dynamics Experiment (CODE)

The Coastal Oceans Dynamics Experiment (CODE) was conducted along the continental shelf from Point Reyes to Point Arena in the spring and summer of 1981 (CODE 1), and 1982 (CODE 2). The goal of CODE was to obtain high quality data sets needed to dynamically describe the response of the continental shelf waters to wind forcing in the temporal band covering the 2-20 day variability (Beardsley and Lentz, 1987).

Atmospheric forcing during CODE 1 and 2 was characterized by periods of strong ( $7-15 \text{ m s}^{-1}$ ) upwelling favorable alongshelf winds lasting up to 30 d, interrupted by shorter periods of much weaker winds directed either poleward or equatorward. The periods of weak or reversed winds typically lasted several days and were primarily associated with coastally trapped perturbations of the



marine layer along the central California coast and not weakening of the North Pacific high. (Beardsley et al., 1987)

Maximum low frequency response in the water column to equatorward wind forcing was found at midshelf and near surface. The mean current during the summer upwelling season was strongly sheared in both vertical and horizontal cross shelf directions. The flow over the outer shelf was surface-intensified and directed off-shelf and equatorward. The flow over most of the water column over the inner shelf was directed poleward. In the absence of local wind forcing, a barotropic jet formed with the maximum amplitude forming over the inner continental shelf. The effect then, of strong equatorward wind forcing would be to counter the poleward flow so that currents on the shelf are everywhere equatorward. (Winant et al., 1987).

The coastal current was measured by a shipboard Doppler acoustic log during CODE (Kosro, 1987) and provided detailed information on the spatial structure of the current field. The nearshore current field was found to be anisotropic, varying more rapidly across-shore than alongshore. A surface-intensified equatorward jet was found in the average alongshore currents over much of the shelf. At depths greater than 80 m the average alongshore flow reversed producing a poleward undercurrent, with strongest amplitudes near the shelf break. Mean current fluctuations were strongly polarized along isobaths near the coast. (Kosro, 1987)

Two other CODE papers indicate the importance of remote forcing from the south along the California coast (Denbo and Allen, 1987; Davis and Bogden, 1989). The basic tenet in either case is that the local current dynamics are consistent with wind-forced, long, coastal trapped waves which are generated to

the south and propagate northward in the coastal waveguide. Denbo and Allen (1987) find that the short period ( $< 4 - 7$  d) are more locally forced, while the long periods ( $> 4 - 7$  d) are best correlated with the wind stress 170 - 300 km to the south. After removing the newly-discovered "Kelvinlike" wave from the sea level and bottom pressure observations, Davis and Bogden (1989) found that the maximum coherence between observed currents on the CODE site and coastal wind stress was with winds measured 500 km to the south.

## **2. The Central California Coastal Circulation Study (CCCS)**

To gain more understanding of the circulation on the continental shelf between Point Conception (PC) and San Francisco (SF), the Central California Coastal Circulation Study (CCCS) was conducted February 1984 through July 1985. Current meter moorings and high resolution hydrographic surveys with a cross-shore spacing of 20 km were conducted inshore of the continental shelf break to study the seasonal variability and spatial coherence of the flow over the continental shelf (Chelton et al., 1988).

From February 1984 through July 1984 there was strong mean poleward flow on the order of  $20 \text{ cm s}^{-1}$  at the 70 m level along the shelf between Point Sur (PS) and PC in opposition to equatorward wind stress with the mean flow north of PS which was equatorward. Fluctuations in alongshore currents over the shelf were highly correlated with the wind everywhere except PC. During periods of weak equatorward winds the poleward continental shelf flow south of PS spread further offshore to the continental slope. Similar nearshore flow had previously been observed off Point Sur throughout 1979 and 1980 (Wickham et al., 1987). The results of CCCS suggest that anomalous weak winds along the central California coast in June and July 1981 and 1984 may have been

responsible for the intensification of poleward flow on the continental shelf (Chelton et al., 1988).

#### **D. PURPOSE OF STUDY**

The Naval Postgraduate School (NPS) Department of Oceanography maintains current meter moorings at 800 m and 1800 m along  $36^{\circ} 20' N$  to measure the energetics of the CC and the CUC as they flow along the central California continental slope (Figure 3). The reader is referred to Sielbeck, (1991) for a complete description of these moorings and a discussion of the current meter accuracies and deployment procedures. To gain a better understanding of how the flow is coupled to the continental shelf a Self-Contained Acoustic Doppler Current Profiler (SC-ADCP) was deployed on the 84 m isobath from 28 February through 11 May 1990. The original intent was to place this mooring in line with the others, however, due to fishing activity the mooring was placed at  $36^{\circ} 17' N$ ,  $121^{\circ} 59' W$  approximately 5 km west of Point Sur.

The SC-ADCP over the past several years has been proven as a reliable means to obtain vertical profiles of horizontal ocean currents (Schott and Johns, 1987; Schott, 1986; Johns, 1988; Pettigrew, 1988). The SC-ADCP allows the user the flexibility to place the instrument in the relatively secure surroundings of the sea floor and still observe current in the upper water column. The purpose of this study is to observe the current structure off Point Sur, California using an SC-ADCP and relate these currents to the local and remote forcing. Data acquisition techniques are described in Chapter II. Data processing and supplemental data sets are discussed in Chapters III and IV. The current data set observations are presented in Chapter V and a theoretical coastal current model, forced by the

observed winds, is described in Chapter VI. Discussion, conclusions and recommendations conclude this paper.

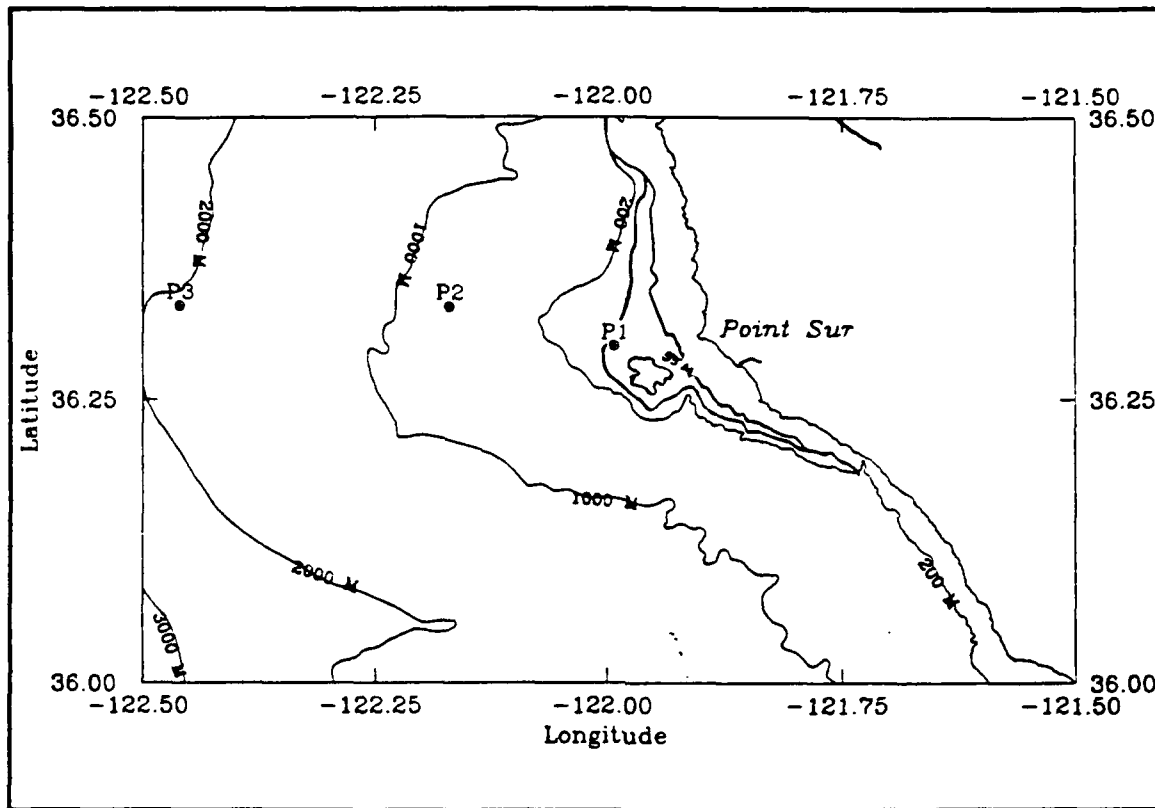


**Figure 3.** Chart of the California coast off Point Sur locating the mooring positions of moorings P1, P2, P3: P3 is located on the 1800 m isobath, P2 is located on the 800 m isobath, and P1 is located on the 84 m isobath.

## II. DATA COLLECTION

### A. PRINCIPALS OF OPERATION

#### 1. The SC-ADCP and mooring geometry

The SC-ADCP (Figure 4a), manufactured by RD Instruments Inc., is a modular instrument consisting of a water-tight transducer assembly which operates at an acoustic frequency of 307 KHz, and a pressure case that houses a magnetic tape recorder, battery packs, pitch and roll sensors, fluxgate magnetic compass, and a high resolution temperature sensor. The SC-ADCP was deployed from 28 Feb - 11 May 1990 at site P1. The mooring was in 84 m of water on a relatively flat section of the sea floor. A rocky shoal area 55 m deep was located about 500 m to the southeast (Figure 3).

The SC-ADCP was secured in a 49 inch syntactic foam sphere that provided approximately 1000 pounds of net buoyancy with the SC-ADCP in place (Figure 4b). The sphere was attached to an anchor via a chain assembly and dual acoustic releases. Because of the large net buoyancy force, the mooring acted essentially as a rigid body experiencing very little tilt ( $< 1^\circ$ ) or rotation throughout the deployment. The length of the mooring, approximately 4 m, placed the transducer heads at the 80 m depth.

#### 2. Velocity calculation

The SC-ADCP operates on the Doppler principal. Acoustic pulses are transmitted along the four vertically inclined beams and the backscattered frequency shifts from scatterers within the water column are measured at the transducer head (Johns, 1988). Since only radial motion relative to the transducer

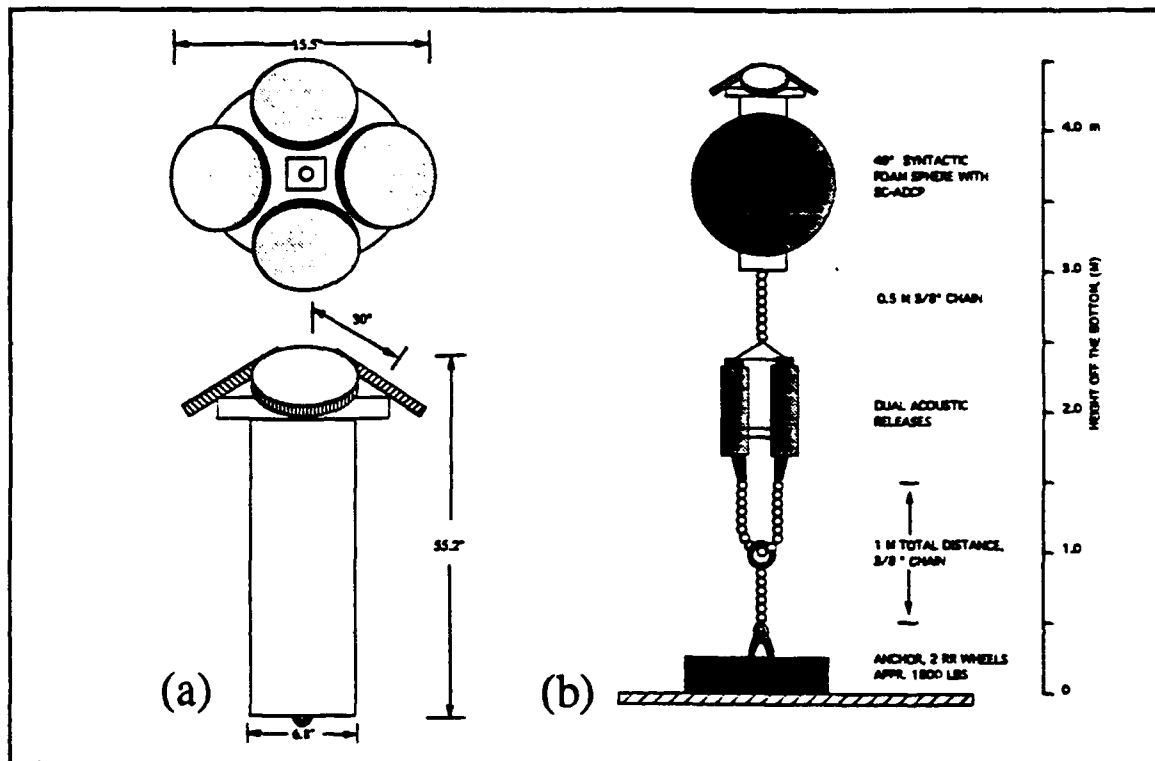


**Figure 4. SC-ADCP configuration and P1 mooring geometry:** (a) The SC-ADCP is a modular instrument consisting of a transducer assembly with four mutually orthogonal transducers at an angle of 30° from vertical and a pressure case that houses the electronics. (b) The SC-ADCP is housed in a syntactic foam sphere that provides 1000 pounds of net buoyancy.

head will cause a Doppler shift, only the velocity component in the direction of the line between the source and the receiver will be observed. The Doppler shifts of the beams are given by

$$f_{Di} = \frac{2V_i(f_t \sin \theta)}{c} \quad i = 1, 2, 3, 4 \quad (1)$$

where  $f_{Di}$  is the frequency shift along each beam,  $V_i$  is the relative velocity between source and receiver,  $f_t$  is the transducer transmit frequency,  $c$  is the speed of sound at the transducer head, and  $\theta$  is the angle of the transducer head from the vertical.

Equation (1) is solved to find the radial velocity component ( $V_i$ ) as a function of the observed Doppler shift ( $f_{Di}$ ) and further post processing is required to convert the radial velocity component into earth-based velocity components. Programming options are available that cause the SC-ADCP to automatically transform the radial velocities into earth coordinates for each ping, to allow in-situ vector averaging. Utilizing this option, and the known beam geometry, radial velocities from three beams are converted into east ( $u$ ), north ( $v$ ), and vertical ( $w$ ) velocity components. The fourth beam is redundant and is used for error checking (RD Instruments, 1989).

## B. INSTRUMENT CONFIGURATION

The SC-ADCP was configured to record an ensemble average of 170 acoustic pulses, or pings, every 15 minutes with a ping duration of one second. The SC-ADCP segmented the velocity profile into uniform depths called depth cells or bins by range-gating the return from each ping. Twenty 4-m bins were recorded for each of the 7025 usable ensembles (record length of 70 days). Adjacent cells

were not statistically independent, because of the overlap from the sliding digital filter which caused a correlation between adjacent cells of 0.15 (RD Instruments, 1989). In order to examine statistically independent current data, only every other bin was used for further processing. This in effect produced a vertical profile consisting of 10 independent current measurements centered at 8 m apart. The stored data consisting of header and current information were converted into ASCII format utilizing software provided by RD Instruments. The current data were then transferred to the NPS Vax 11/780 computer where the count formatted data were converted into engineering units. All subsequent analysis and graphical display was accomplished using the Vax computer.

### **C. ERROR ANALYSIS**

#### **1. Bias and random error**

The nature of Doppler velocity measurement will induce two kinds of errors that contribute to velocity uncertainty. These errors are bias and random error. Bias is typically on the order of  $0.5 - 1.0 \text{ cm s}^{-1}$ . The bias of the instrument depends on a variety of factors including temperature, mean current speed, signal/noise ratio, beam geometry errors etc. It is not yet possible to exactly measure SC-ADCP bias and to remove it in post-processing.

Single ping SC-ADCP operation will also introduce random error. Since random error is uncorrelated for each ping, averaging multiple pings will reduce the standard deviation of the error velocity. Because the external bias of the SC-ADCP is on the order of  $0.5 - 1.0 \text{ cm s}^{-1}$  it is not beneficial to average the ping data below this value. The number of pings per ensemble that must be averaged to reduce the standard deviation of the random error to a specified level is given by



$$P = \left( \frac{1.6 \times 10^7}{F B 2^L SD} \right)^{\frac{1}{2}} \quad (2)$$

where  $P$  is the number of pings per ensemble,  $F$  is the SC-ADCP transmission frequency,  $SD$  is the desired standard deviation in  $\text{cm s}^{-1}$ ,  $L$  is the depth cell length, and  $B$  is the beam angle coefficient (1.0 for a  $30^\circ$  beam). Equation (2) yields a 170 ping ensemble necessary to resolve the standard deviation of random error velocity to  $1.0 \text{ cm s}^{-1}$  which is equal to the bias of the instrument. (RD Instruments, 1989)

## 2. Sound speed difference at transducer

The SC-ADCP assumes a fixed sound speed of  $1536 \text{ m s}^{-1}$  over the entire water column. Since the recorded velocity values are scaled frequency shifts in Hertz, horizontal velocity errors will be introduced if there are variations in sound speed. To correct for variations in sound speed a constant multiplicative factor of  $C_0 / 1536 \text{ m s}^{-1}$  is used where  $C_0$  is the speed of sound at the transducer head. This correction is only required at the transducer head because variations in sound speed over the water column are exactly compensated for by ray bending (Johns, 1988). Snell's Law stipulates that horizontal wavenumber must be conserved when sound passes through horizontal surfaces. Since the frequency is constant, sound speed variation, as a function of depth will not affect the horizontal component of the sound velocity (RD Instruments, 1989).

## 3. Conversion to earth coordinates

The velocity data retrieved from the SC-ADCP deployed off Point Sur were stored on a magnetic tape in earth-based reference coordinates. The internal

processing required to convert the radial-coordinate beam data into earth-coordinate based system is described with emphasis placed on sources of potential error.

When the SC-ADCP is mounted on a mooring free to change orientation the automatic conversion of the radial velocity components to earth-based system is required. Recording the data in earth-coordinates reduces post-processing, although there may be a slight trade-off in data quality. The main loss can be attributed to the depth cell mapping feature of the instrument. The SC-ADCP automatically calculates velocity at particular depth cells that are at the same depth (RD Instruments, 1989). If excessive tilt is present, the SC-ADCP processing software will try to adjust for the deviation, from the normal orientation of straight up, by reassigning bins from each beam to different depth levels so that the velocity is always calculated from bins at about the same depth (Johns, 1988). This may cause some bins to be skipped. The observed tilt at mooring P1 (Figure 5), however, indicates that the current induced mooring tilt was negligible and that errors introduced would be insignificant.

#### **D. DATA VELOCITY CHECKS**

##### **1. Echo Amplitude**

Echo amplitude is a measure of the energy intensity of the backscattered echo for each depth cell. Useful in determining signal strength, it is also used as a check for data quality. Since echo amplitude is a function of the distance from the transducer and the number of scatterers in the water column, echo amplitude will normally decrease until the theoretical range of the instrument is reached. For the 307 KHz SC-ADCP this range is 120 m and the surface should be well within range of the instrument (RD Instruments, 1989).

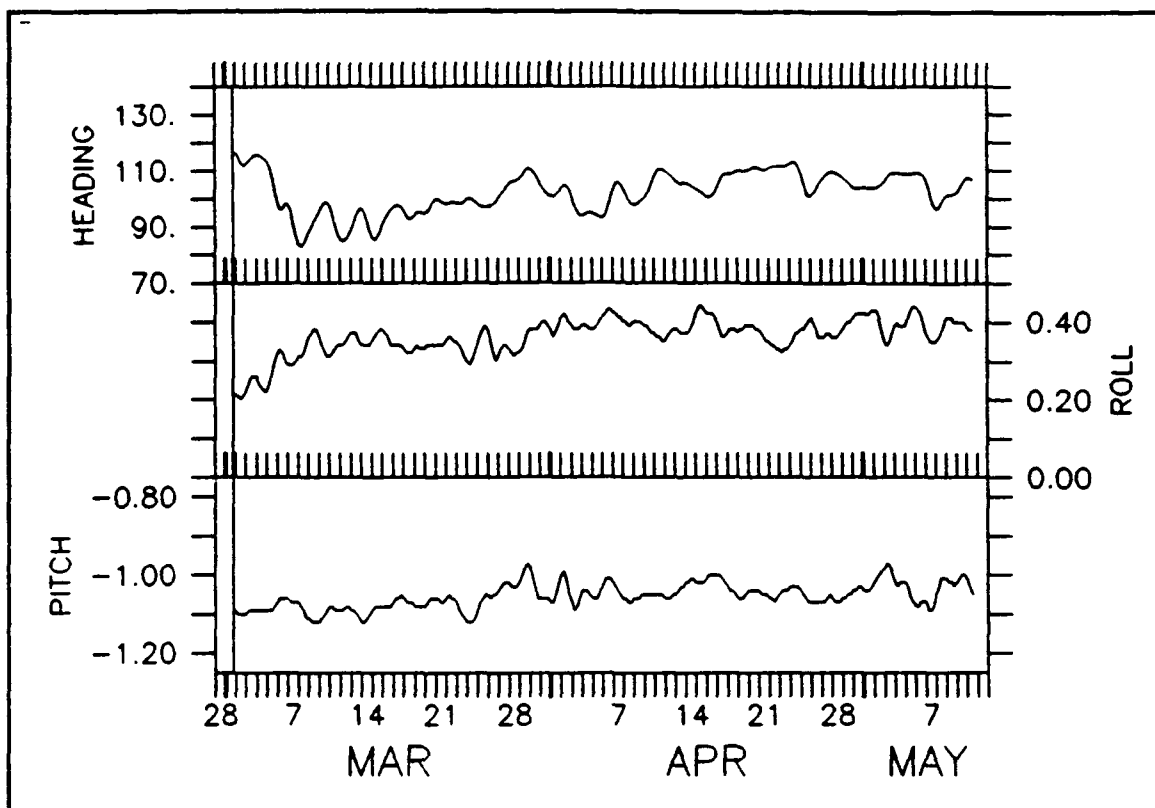


**Figure 5.** Time series of heading, pitch, and roll from the SC-ADCP: Heading is degrees magnetic, roll is in degrees and represents deviation in the u plane of motion, and pitch is in degrees and represents deviation in the v plane of motion. The constant offset of about  $1^\circ$  in pitch is due to the way the SC-ADCP was mounted in the buoy and was not induced by the current.

The values of echo amplitude for all four beams at each depth level, averaged over the entire deployment (Figure 6) show that the amplitude of the signal decreases as a function of range from the transducer heads. However, in the near surface bins, there is a substantial increase in amplitude. The large amplitudes can be accounted for by the characteristics of the acoustic pulses. Each pulse consists of a main lobe where most of the power is directed and sidelobes which contain the remaining power. The sidelobes are designed to be at least 40 dB below the main lobe and are found about  $40^\circ$  offset from the main

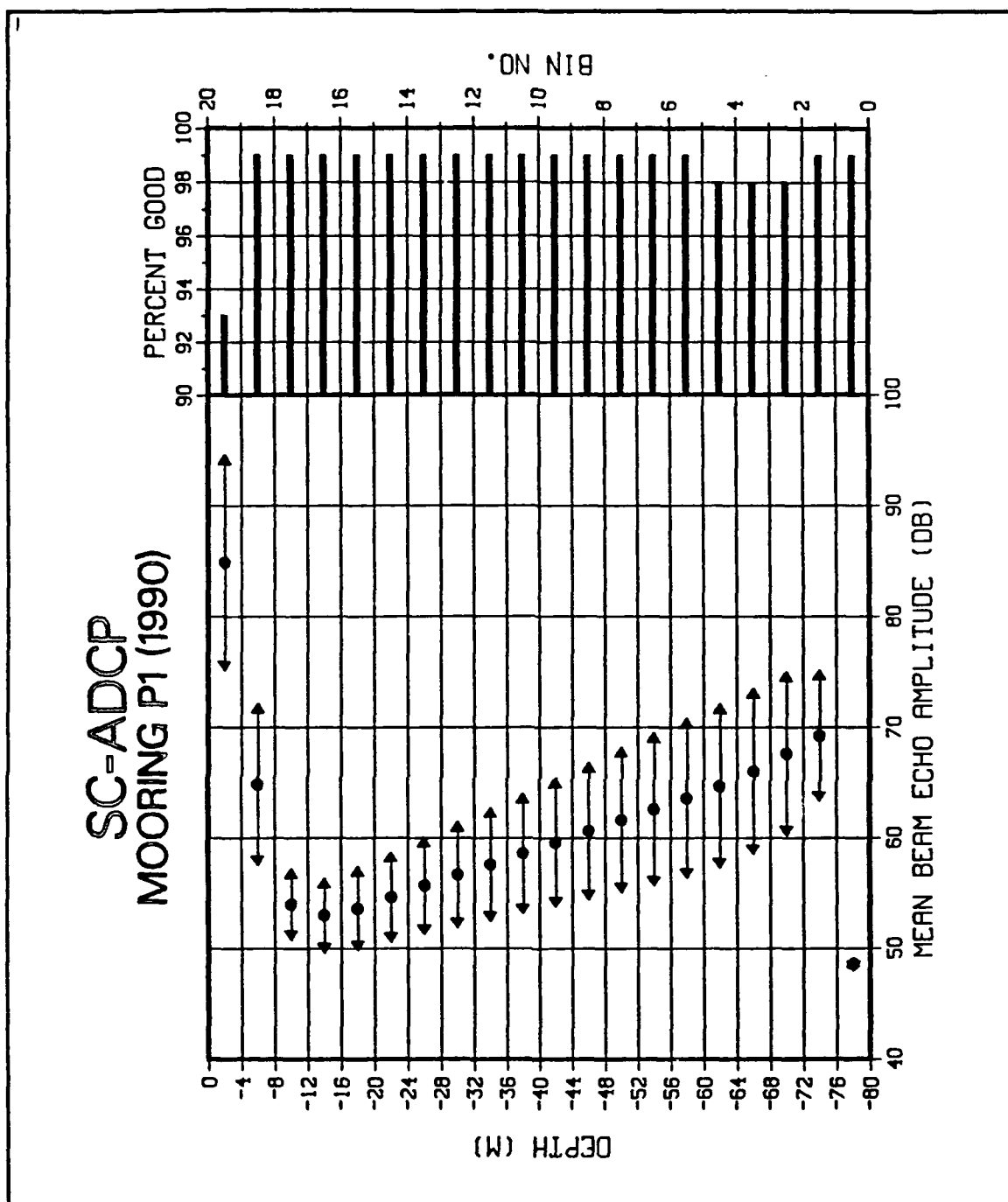


Figure 6. SC-ADCP echo amplitude and percent good: Dots represent average values of echo amplitude for all four beams averaged over the deployment with standard deviation superimposed over each value. Percentage of good pings are represented by percent bars and are averaged for all four beams (from RD Instruments, 1989).

lobe. The echo from a hard surface such as the sea surface is much stronger than the echo from the scatterers in the water. With each transducer oriented at 30° from the vertical, the echo from the side lobe facing the surface will return to the SC-ADCP at the same time as the echo from the main lobe at 85 percent of the distance to the surface (Figure 7), which overwhelms the side-lobe suppression and regulates the quality of the data. The equation that governs this is given by:

$$R_{\max} = D \cos \theta$$

where  $R_{\max}$  is the maximum range for acceptable data,  $D$  is the distance from the SC-ADCP to the surface, and  $\theta$  is the angle of the acoustic beam relative to vertical. For an SC-ADCP at 80 m depth with a 30° beam angle, the value of  $R_{\max} = 69$  m and data within 11 m of the surface will be contaminated and should be disregarded. This is indicated by the increase in echo amplitude in the upper three bins (Figure 6). (RD Instruments, 1989)

The low echo amplitude associated with bin 1, or the deepest level, can be attributed to a hardware problem in the receive circuitry of the SC-ADCP (RD Instruments, Personal Communication). Based on analysis covered in later sections, this data was determined to be usable.

## **2. Percent Good**

The percent good is a measure of the percentage of pings per ensemble that are greater than the signal-to-noise threshold programmed into the SC-ADCP. The threshold was set to 6 dB above background noise (RD Instruments, 1989). Each percent bar (0-99) (Figure 6) represents the percentage of good pings averaged over all four beams during the deployment of the instrument.

Values indicate high confidence in the data collected encompassing the water column. There is however, a difference of about seven percent near the surface probably due to side-lobe interference.

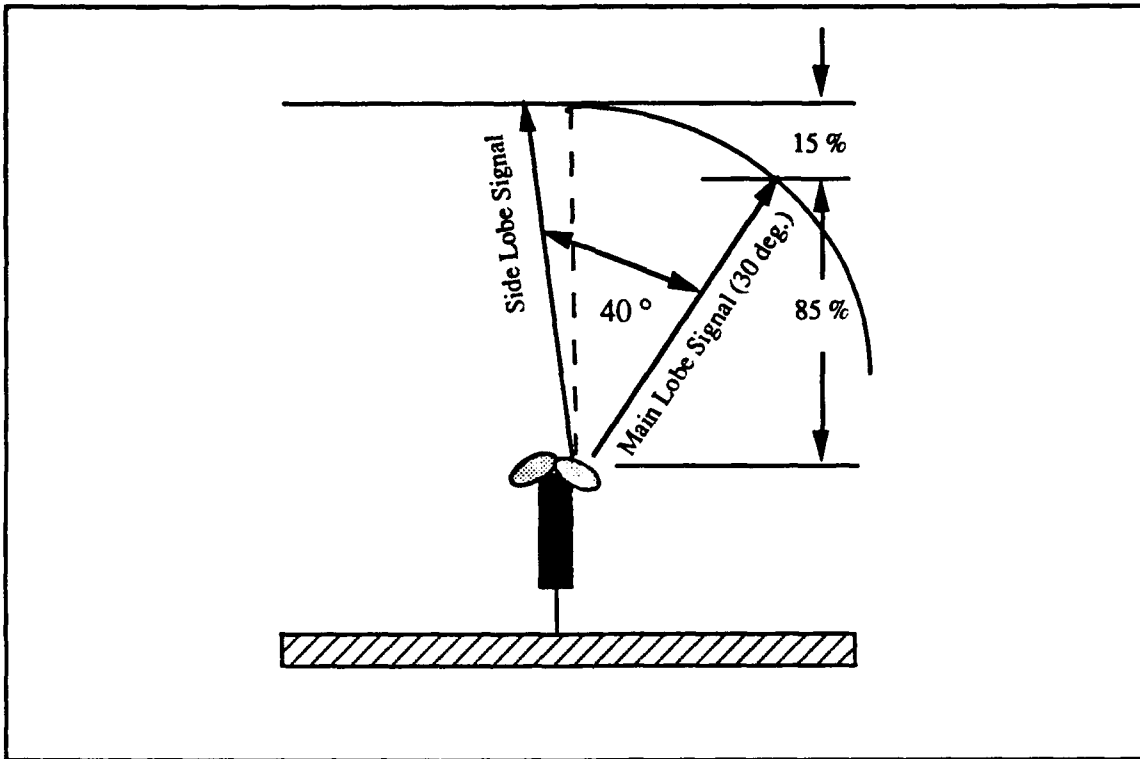


**Figure 7. SC-ADCP transducer beam characteristics:** The design specification for the side lobe is 40 dB below the main lobe and offset by 40°. (from RD Instruments, 1989)

### III. SUPPLEMENTAL DATA SETS

Wind and atmospheric pressure data from National Oceanographic and Atmospheric Administration (NOAA) weather buoys stationed off the California coast and sea level data from tide stations operated by the National Ocean Service (NOS) were utilized in this study. The geographical locations of these instruments are summarized in Figure 8.

#### A. WIND STRESS DATA

Wind data was available from the Monterey Bay buoy and the Cape San Martin buoy located to the north and south of site P1 respectively. Strong correlation between the data sets suggested local wind forcing at P1 could be taken from either source. The local stress was derived from wind data at the Monterey Bay buoy following the method of Large and Pond (1981). The reader is referred to Tisch (1990) for gap filling techniques and wind level correction schemes employed. Once all data gaps were filled and wind speed corrected to the 10 m level, surface stress components were calculated according to

$$\overrightarrow{\tau_x} = \rho_a C_D |\vec{V}| u$$

$$\overrightarrow{\tau_y} = \rho_a C_D |\vec{V}| v$$

where  $\overrightarrow{\tau_y}$  and  $\overrightarrow{\tau_x}$  are the northward and eastward components of wind stress,  $\rho_a$  is the atmospheric density,  $C_D$  is the drag coefficient, and  $|\vec{V}|$  is the magnitude of the velocity with the u - component east and the v - component north.

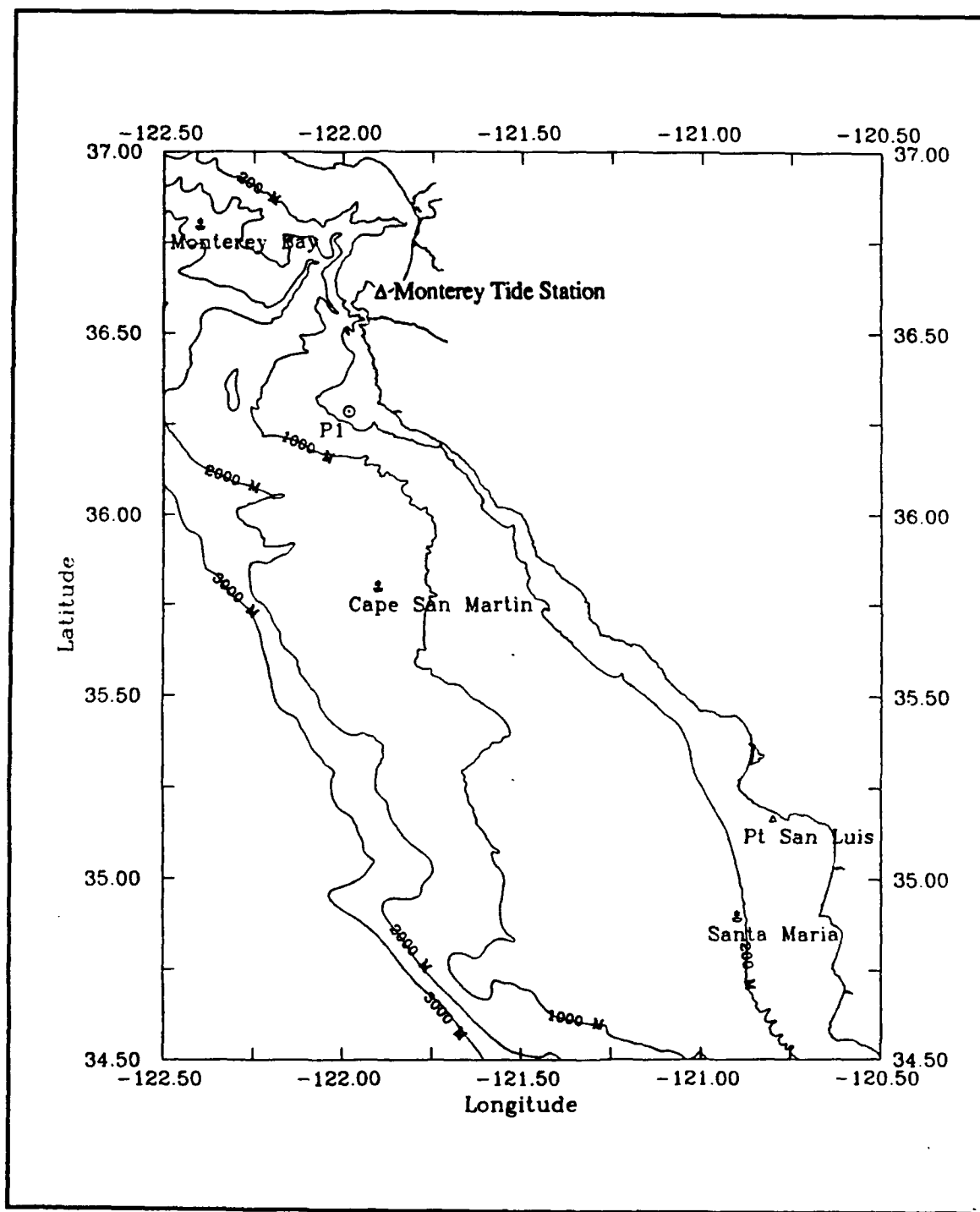


**Figure 8. Chart of California coast indicating geographic positions of NOAA buoys and tide stations.**



## **B. HYDROGRAPHIC DATA**

The determination of the water characteristics, particularly the stratification, was essential to accurately model the flow field. Several hydrographic surveys were conducted in the vicinity of mooring P1 in support of related activities of the NPS Oceanography Department. Data were collected from the surface to the near bottom using a Neil Brown Instruments System Mark III CTD. The reader is referred to Tisch (1990) for a detailed description of CTD data acquisition techniques and procedures.

## **C. SYNTHETIC SUBSURFACE PRESSURE**

Synthetic subsurface pressure (SSP), also known as adjusted sea level (ASL), was calculated as the algebraic sum of the atmospheric pressure and the local sea level converted to decibars (Brown et al., 1985). This procedure partially corrects for the inverse barometer effect so that the remaining pressure fluctuations are primarily due to oceanic phenomenon. The calculation was made at two coastal sites, Monterey Bay and Port San Luis. Atmospheric pressure used for Monterey Bay was based on the average of Monterey Bay and Cape San Martin, and for Port San Luis, the average of Santa Maria and Port San Luis. The reader is referred to Tisch, (1990) for gap filling procedures and data conversion techniques. To obtain the alongshore difference in SSP the two-year mean value was removed for each station and the Monterey Bay data was subtracted from the Port San Luis data. The sign convention is such that a (+) SSP difference implies a poleward pressure gradient and a (-) SSP difference, an equatorward pressure gradient. Since the two stations were not geophysically leveled, the true

mean difference in SSP height is unknown, however, trends and fluctuations in  $\Delta$ SSP should be well represented by the technique.

## **IV. DATA PROCESSING**

### **A. DATA FILTERING**

After all data was downloaded into the Vax computer each data set was filtered using methods originally developed by Oregon State University (Denbo et al., 1984). Current data at 15 minute intervals was first low passed (LP) filtered using a Cosine-Lanczos filter. This filter utilized a one half power period of 2.9 hours (or 8.4 cpd) which allowed any signal with a period exceeding 3.6 hours to pass unattenuated. A centered 25 point segment of the record was used to produce each LP data point. After LP filtering each record was interpolated to transform 15 minute data records to 60 minute intervals with each data point falling on an even hour. To eliminate tidal signals, the current data was then low pass filtered (LLP) using a Cosine-Lanczos filter with a constant 121 point segment and had a half power period of 46.59 hours. The data were subsampled to transform the 60 minute data to 6 hour intervals with each data point falling on an even 6 hour mark. (Sielbeck, 1991)

Since the wind data were recorded at 60 minute intervals, only the LLP filtering was accomplished. The data were then subsampled to six hour intervals as with the current data. A sample from the SC-ADCP data set (Figure 9) shows the result of filtering.

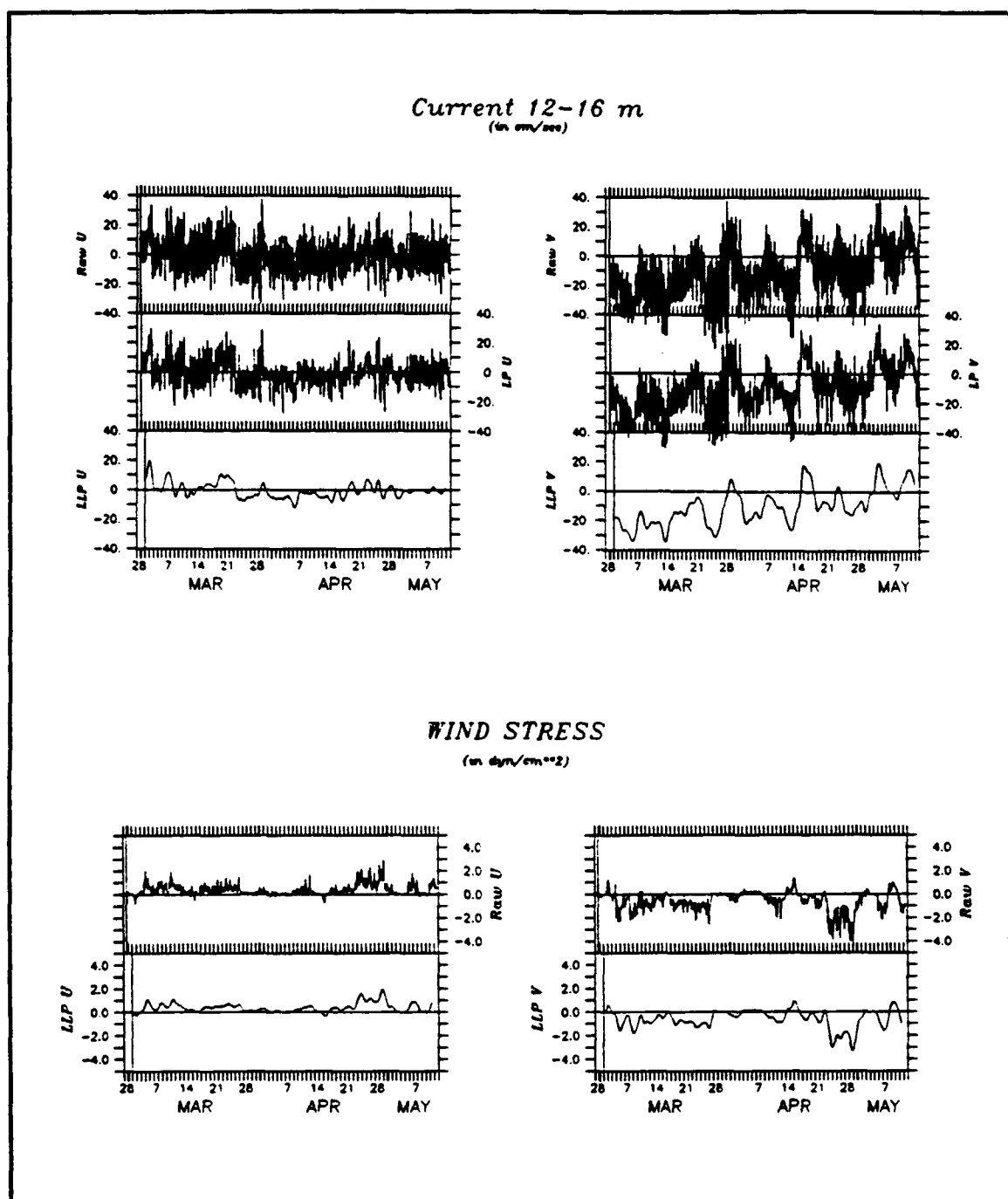


**Figure 9.** Example of filtering technique: Raw data for each component is passed through a low pass (LP) filter and plotted at hourly marks. Hourly data is then passed through a low pass (LLP) filter and plotted at six-hourly marks.

## B. SPECTRAL ANALYSIS

To quantify the graphical presentations in Chapter IV, spectral analysis was performed using the spectral processing package PROSPECT developed by the Woods Hole Oceanographic Institution. This software package was written in Fortran 77 and designed to run on the VAX 11/780 computer. It performs spectral analysis of equally-spaced time series.

The following discussion details the basic operations required to estimate coherence and phase functions. This discussion utilizes theory following Bendat and Piersol (1986) and operations performed by PROSPECT. The current and wind stress data sets consist of 283 equally spaced points of six-hourly LLP data. The data sets were divided into three pieces of 92 points each. To suppress sidelobe leakage, a Hanning taper was applied to each block of data. The Fast Fourier Transform (FFT) was computed for each block and in order to reduce the variance increase caused by tapering, the FFT was computed for a 50 % overlapped record.

The auto spectra density estimate is given as

$$\hat{G}_{xx}(f_k) = \frac{2}{n N \Delta t} \sum_{i=1}^n |X_i(f_k)|^2 \quad k = 0, 1, \dots, \frac{N}{2}$$

where  $n$  is the number of blocks of data,  $N$  is the number of data values, and  $\Delta t$  is the time step. The cross spectral density estimate for each pair of blocks is computed as

$$\hat{G}_{xy}(f_k) = \hat{C}_{xy}(f_k) - i\hat{Q}_{xy}(f_k)$$

where  $\hat{C}_{xy}(f_k)$  is the cospectrum, and  $\hat{Q}_{xy}(f_k)$  is the quadrature spectrum. Subscripts (x,y) indicate this is the cross spectrum between two time series  $C_x(t)$  and  $C_y(t)$ .

The ordinary coherence function between two stationary records can then be determined by

$$\hat{\gamma}_{xy}(f) = \sqrt{\frac{|\hat{G}(f)_{xy}|^2}{\hat{G}(f)_{xx} \hat{G}(f)_{yy}}}$$

and the phase angle by which series x leads series y at the frequency (f) is determined by

$$\hat{Q}_{xy}(f) = \text{Tan}^{-1} \left[ \frac{\hat{Q}_{xy}(f)}{\hat{C}_{xy}(f)} \right]$$

The calculations for the significance level follows Halpern, (1973). A 95 % confidence level was used as input into PROSPECT. The significance level ( $\rho^*$ ) represents the coherence value which is exceeded by 5 % of the coherence estimates when correlating two random value series. The significance level is given by

$$\rho^* = \left( 1 - (1 - p)^{\left( \frac{2}{v - 2} \right)} \right)^{\frac{1}{2}}$$

where  $v$  is the estimated degrees of freedom and  $p$  is the probability such that  $100(1-p)$  % of the coherence values will be greater than  $\rho^*$  when the series is uncorrelated.

## V. OBSERVATIONS

### A. SPATIAL AND TEMPORAL CHARACTERISTICS

To illustrate the vertical structure of the current as it responds to local forcing at P1 during the deployment of the SC-ADCP, wind stress and current velocities are presented in stick vector format with north oriented up (Figure 10). All data have been LLP filtered as described in Chapter IV and the local wind stress and current from every other bin is plotted as a function of time using six-hourly marks.

The current exhibited a high degree of correlation with the local wind stress. Both wind stress and current were strongly polarized in the equatorward direction. Equatorward wind stress forcing produced currents whose vertical structure was highly sheared with velocities on the order of  $35 \text{ cm s}^{-1}$  seen in the near surface bins decreasing to  $5 - 10 \text{ cm s}^{-1}$  in the bottom bins. There was also a pronounced time lag in the response of the water column with depth as the effects of wind forcing translated itself deeper into the water column. This was readily evident in the 21 - 28 March equatorward wind event. This type of response however, appeared to be limited to the first half of the time record. The strongest wind event of the record occurred during 24 April - 02 May with wind stress magnitudes as great as  $3.0 \text{ dyn cm}^{-2}$ , however, it did not produce a strong equatorward current like the earlier equatorward wind events. Possible mechanisms to account for this will be addressed in the discussion section.



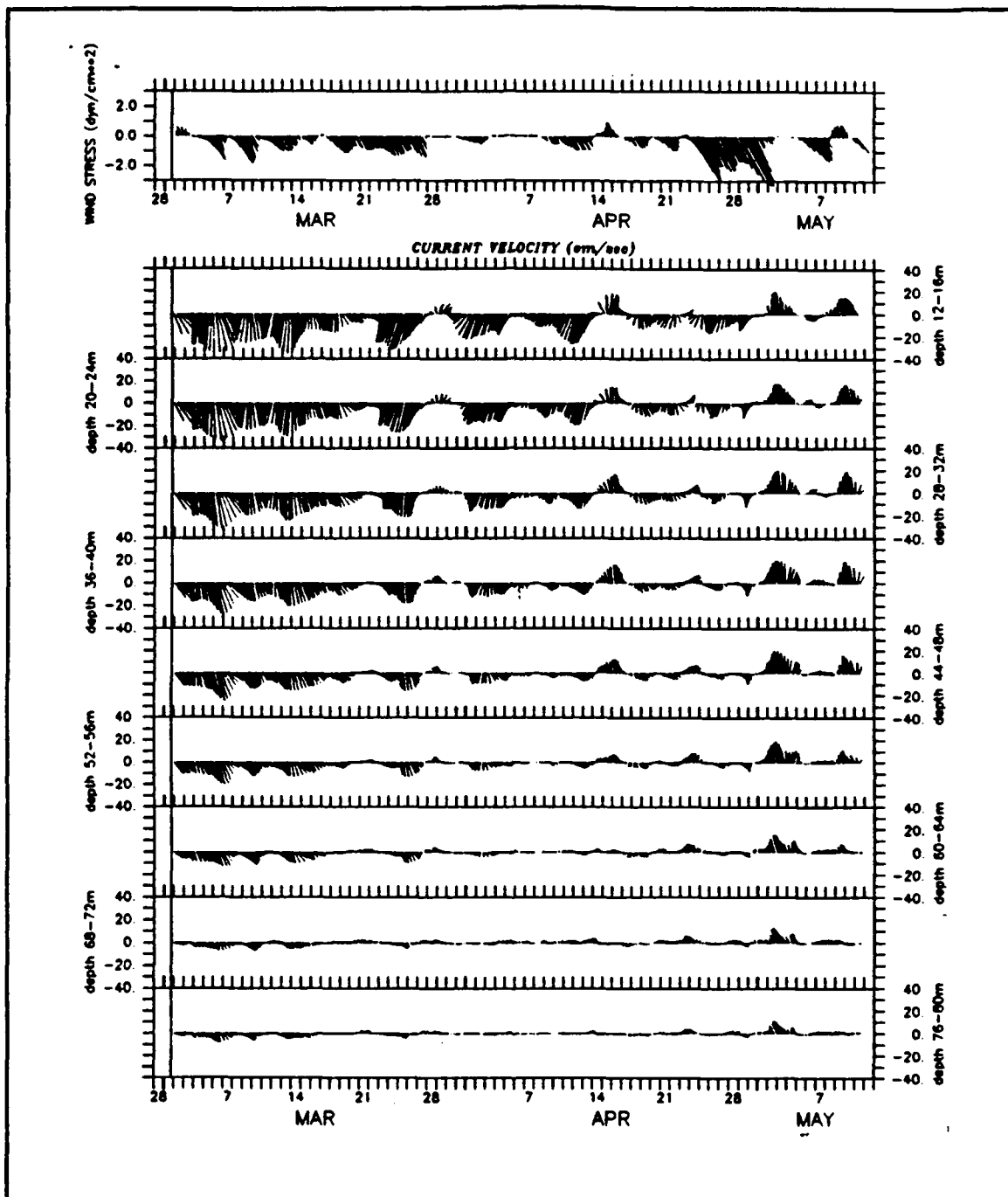
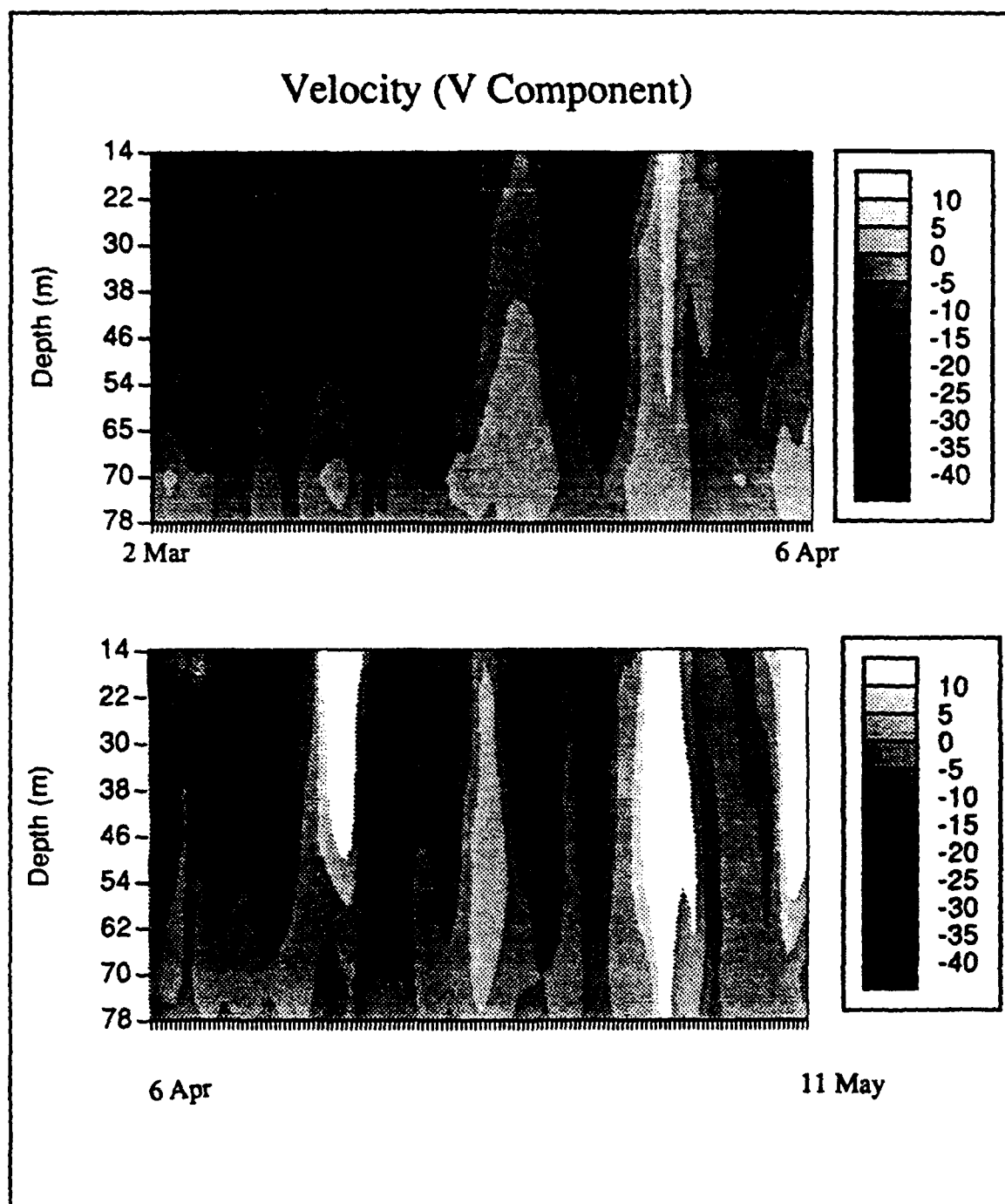


Figure 10. Time series, in stick vector format, of the low-passed filtered local wind stress taken from the Monterey Bay NOAA buoy and current velocity from the SC-ADCP at mooring P1: The direction of the vector indicates direction of flow, the length of the vector represents magnitude. Velocities are in  $\text{cm s}^{-1}$ , and north is toward the top of the page.

Interspersed with the equatorward wind events were relaxations (periods of no wind) and wind reversals. There were four distinctive poleward current responses in the record which occurred 28 - 29 March, 14 - 16 April, 02 - 05 May, and 08 - 09 May with each corresponding to a relaxation or wind reversal. The resulting vertical structure was more uniform than in the equatorward events, and did not show any observable time lag in the vertical. This was most clearly seen in the latter two events where poleward current magnitudes up to  $10 \text{ cm s}^{-1}$  were present throughout the column. The response of the water column also appeared to be more energetic later in the time series. Extensive research concerning the barotropic response of the continental shelf water was conducted during CODE. The reader is referred to Kosro (1987), Winant et al. (1987) and Huyer (1987) for detailed discussion of similar responses to wind relaxations.

The  $v$  - component plot (Figure 11) clearly showed the vertically sheared nature of the equatorward wind stress events and the trend of decreased equatorward current with time. The barotropic nature of the poleward relaxation events were also evident and as time progressed the tendency for a more energetic response was observed. The  $u$  - component plot (Figure 12) indicated that offshore flow during equatorward events was highly sheared and confined to the upper 30 m of the water column while a more constant magnitude ( $0 - 5 \text{ cm s}^{-1}$ ) onshore "return" flow encompassed the remaining water column to the bottom.

The vertical shear values in  $\text{cm s}^{-1}$  were calculated as vertical differences in the magnitude of the current at each successively deeper bin (Figure 13). The results highlight the shear structure of the  $v$  component that resulted from equatorward wind forcing and relaxation events. The current response to the



**Figure 11.** Time series of  $v$  current component from the SC-ADCP at 80 m depth: Velocity values are represented by contours at  $5 \text{ cm s}^{-1}$  intervals, as indicated by the scale on the right. The contours are estimated from 6 - hourly values of 8 - m intervals in the water column.

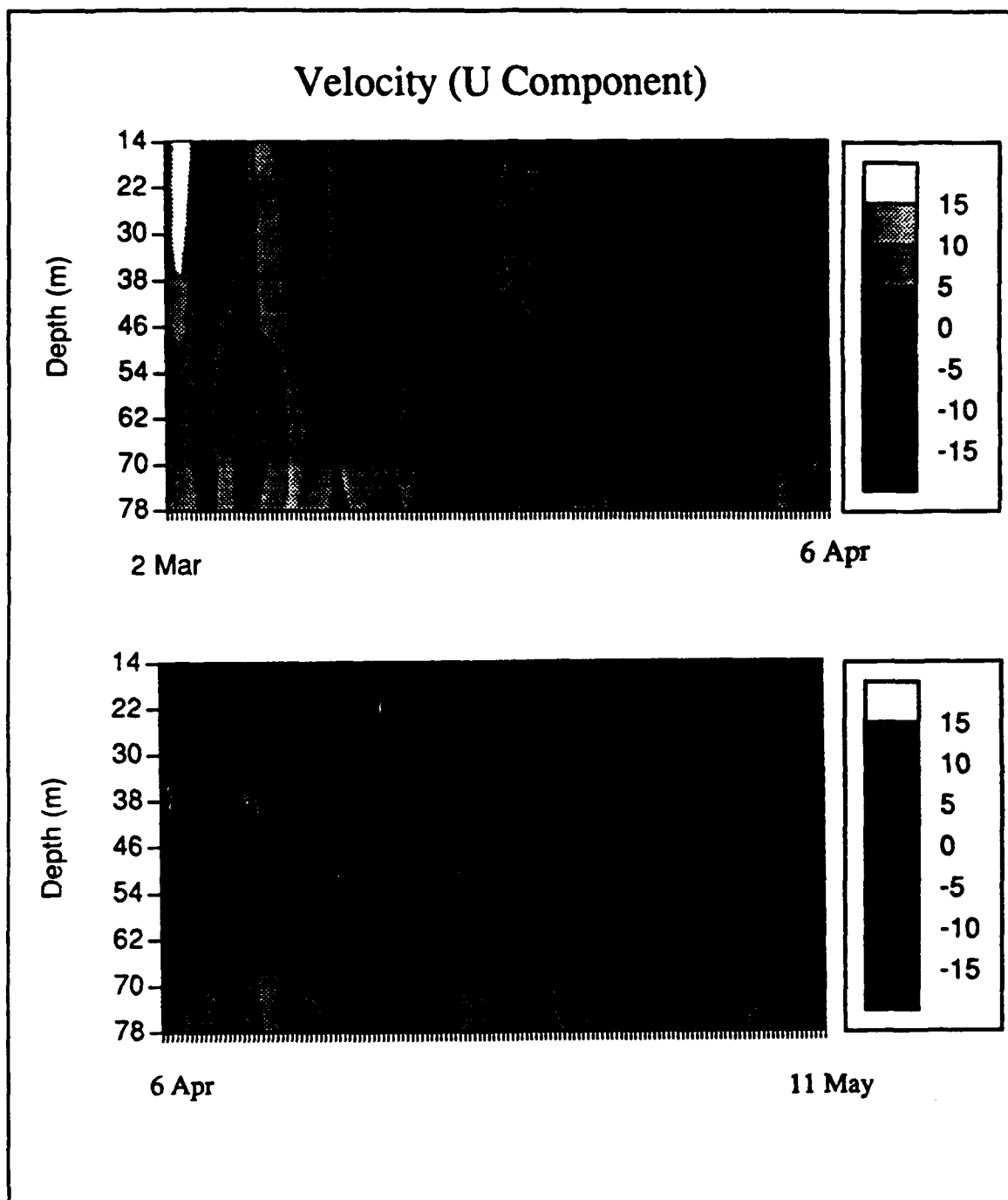


**Figure 12.** Time series of u current component from the SC-ADCP at 80 m depth: Velocity values are represented by contours at  $5 \text{ cm s}^{-1}$  intervals, as indicated by the scale on the right. The contours are estimated from 6 - hourly values of 8 - m intervals in the water column.

equatorward wind event of 21 - 28 March exhibited shear on the order of  $1.5 \text{ cm s}^{-1} \text{ m}^{-1}$  in the upper depth bins, near zero at mid-depth, and increasing shear to the near bottom. In contrast, the shear observed during the relaxation of 02 - 05 May exhibited a different structure. From the near surface bin, to mid-depth, the shear was near zero. It then increased rapidly to a maximum of  $1.5 \text{ cm s}^{-1} \text{ m}^{-1}$  at 68 - 72 m, then rapidly to zero. The wind reversal of 14 - 16 April produced a current response similar the 02 - 05 May event from mid-depth to the bottom, however, a shear of  $1.0 \text{ cm s}^{-1} \text{ m}^{-1}$  was present in the near surface which was not seen in the May relaxation event.

The  $u$  - component shear plot (Figure 14), provides insight on the vertical structure of the water column as it responded to upwelling favorable equatorward winds. Two equatorward wind stress events that occurred during 21 - 28 March and 07 - 14 April produced large shear, on the order of  $1.5 \text{ cm s}^{-1} \text{ m}^{-1}$  in the near surface, a minimum at mid-depth with shear near zero, and minimal shear, less than  $0.5 \text{ cm s}^{-1} \text{ m}^{-1}$ , from mid-depth to the bottom.

These shear plots suggested most of the water column was under the influence of frictional forces, which induced shear in the water column. These forces were acting on both the surface currents, via the surface wind stress, and on the near bottom currents, via bottom friction.

## B. EQUATORWARD EVENTS

To examine the response of the water column to equatorward wind forcing in more detail, four daily averaged current profiles were chosen for additional analysis (Figure 15). Each profile was computed at least one day into a well developed equatorward wind event, and possessed similar characteristics. The  $v$  -

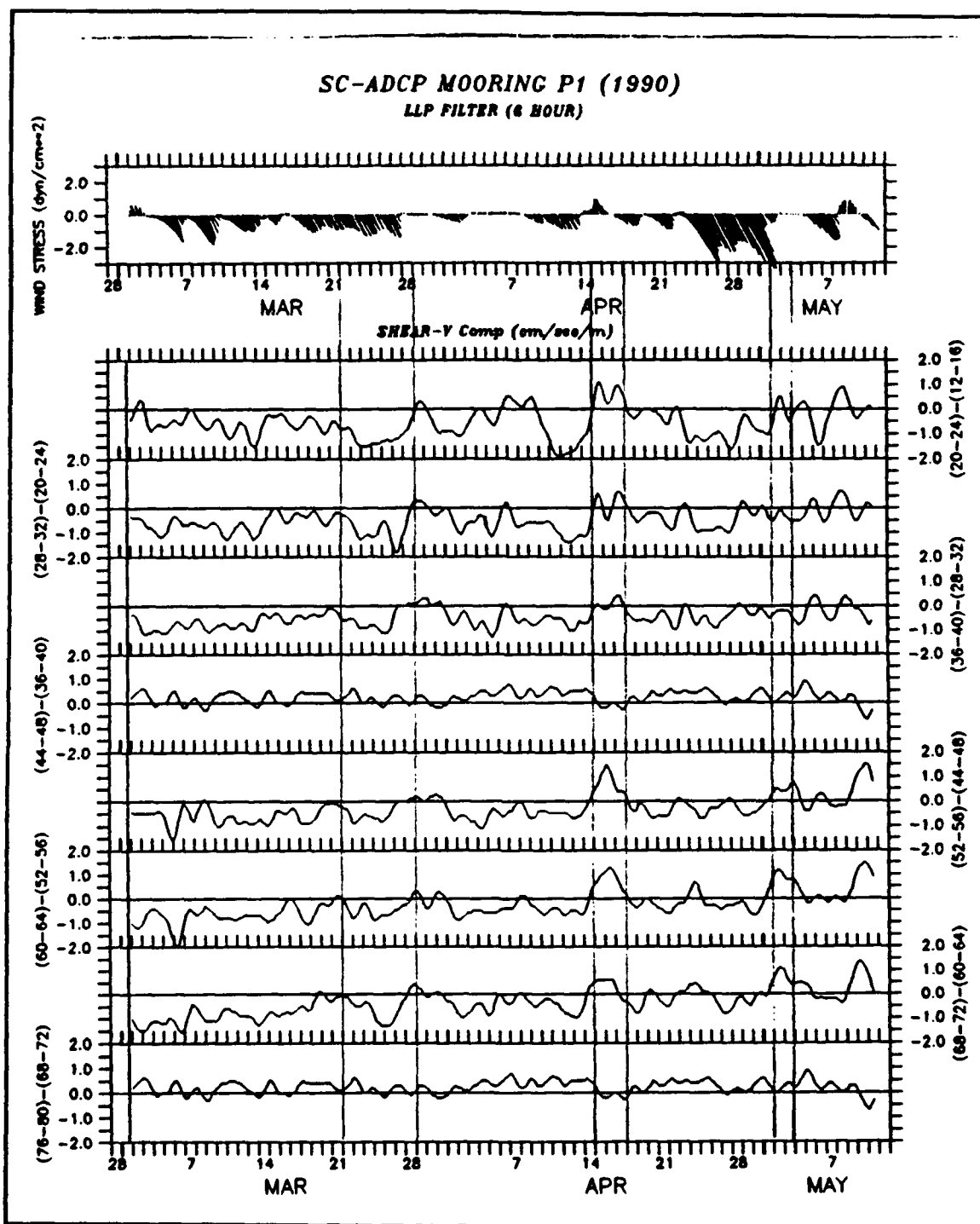


**Figure 13. Time series of vertical shear for v current component:** Values of shear are calculated by differencing each successive depth bin. The units on the y - axis are  $\text{cm s}^{-1}\text{m}^{-1}$ . Vertical lines indicate current events discussed in the text.

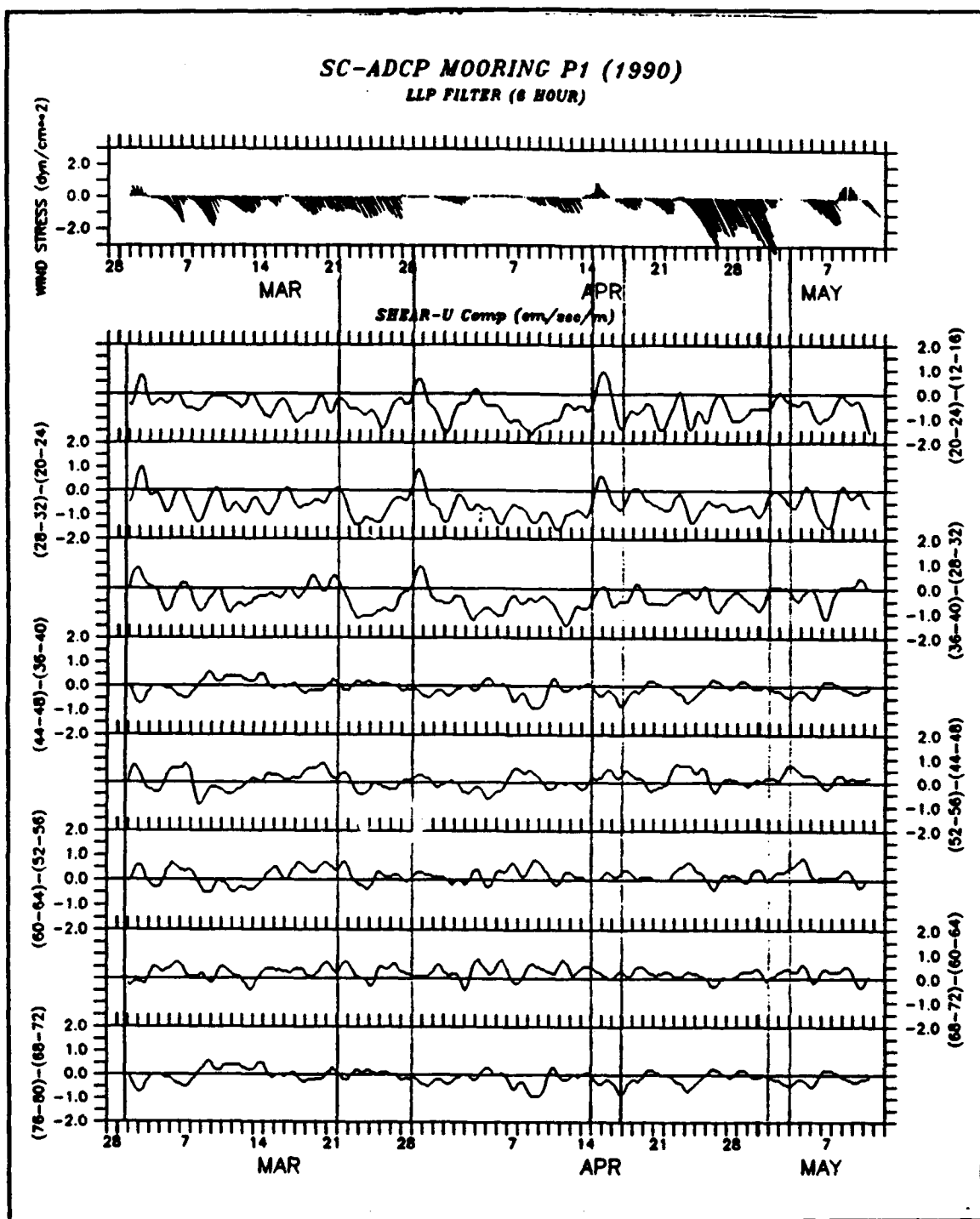


**Figure 14. Time series of vertical shear for u current component: Values of shear are calculated by differencing each successive depth bin. The units on the y - axis are  $\text{cm s}^{-1}\text{m}^{-1}$ . Vertical lines indicate current events discussed in the text.**

component in each profile had a magnitude of about  $30 \text{ cm s}^{-1}$  at the surface, decreasing with depth, and is everywhere equatorward. The temporal trend of decreasing equatorward flow was evident when comparing the 7 - 10 March and 7 - 12 April profiles, particularly in the lower portion of the profiles. The current at 68 - 72 m of 7 - 10 March was on the order of  $10 \text{ cm s}^{-1}$  while the magnitude of the current on 7 - 12 April at the same depth had decreased to near zero.

Examining the  $u$  - component for each event showed that the transition from an offshore flow to an onshore flow generally occurred at about 30 m. The current was sheared below the transition depth and became less sheared with increasing depth. These profiles suggest a wind-driven offshore flow in the upper (30 m) layer and a compensatory onshore flow below. Similar results of offshore flow in a thin surface layer with onshore flow in a thicker interior layer are observed in Huyer (1983).

The vertical structure of the same four events were projected on a horizontal plane as hodographs (Figure 16). The current measured at each bin was represented by a dotted vector. The wind stress, represented by a solid vector, was increased by a factor of 10 to facilitate comparison with the current. The hodographs were similar for all four events. Local wind forcing caused a near surface current to develop to the right of the wind stress vector with velocities on the order of  $20 - 25 \text{ cm s}^{-1}$ . The magnitude of the current was greatest in the near surface bins and exhibited a general decrease with increasing depth while veering counter-clockwise. The lowest magnitudes on the order of  $5 - 10 \text{ cm s}^{-1}$  occurred near the bottom.



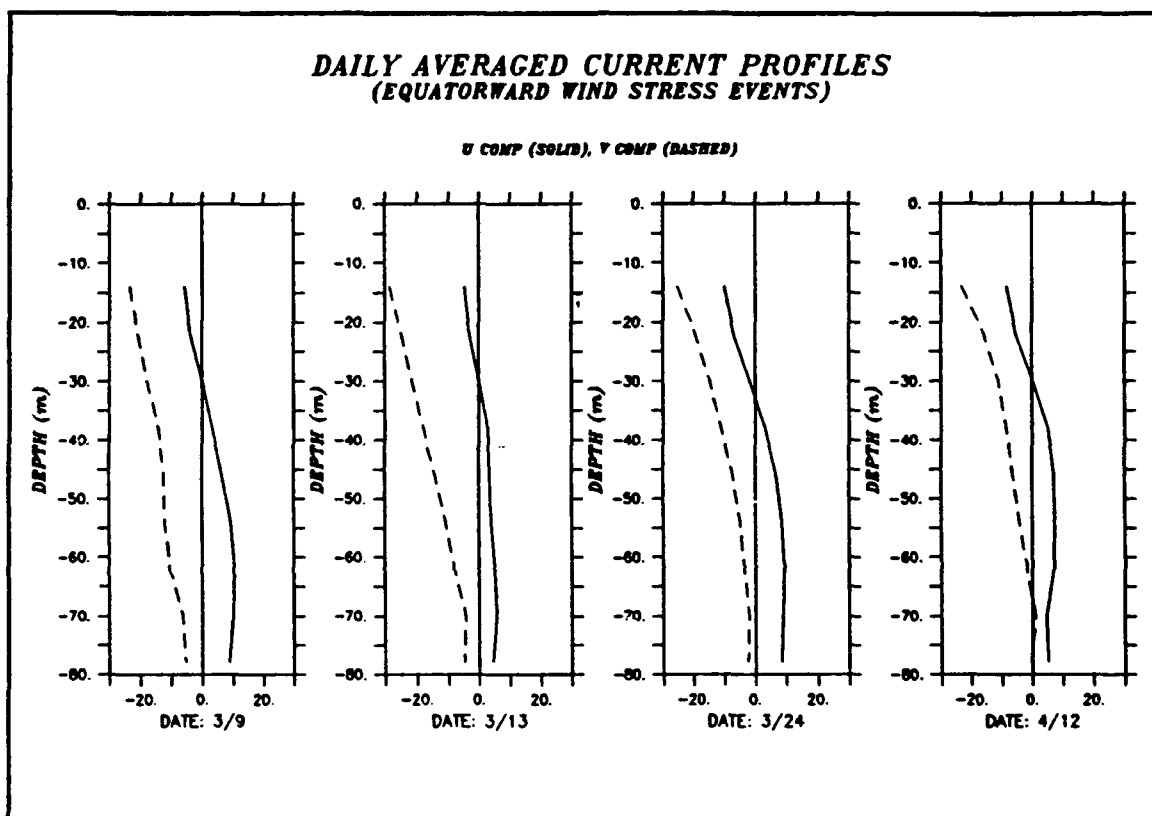


**Figure 15.** Daily averaged equatorward wind forced current profiles in component format: The u component of current is represented by a solid line, and the v component by a dashed line. Velocity values are in  $\text{cm s}^{-1}$  and were measured from 14 m to 80 m.

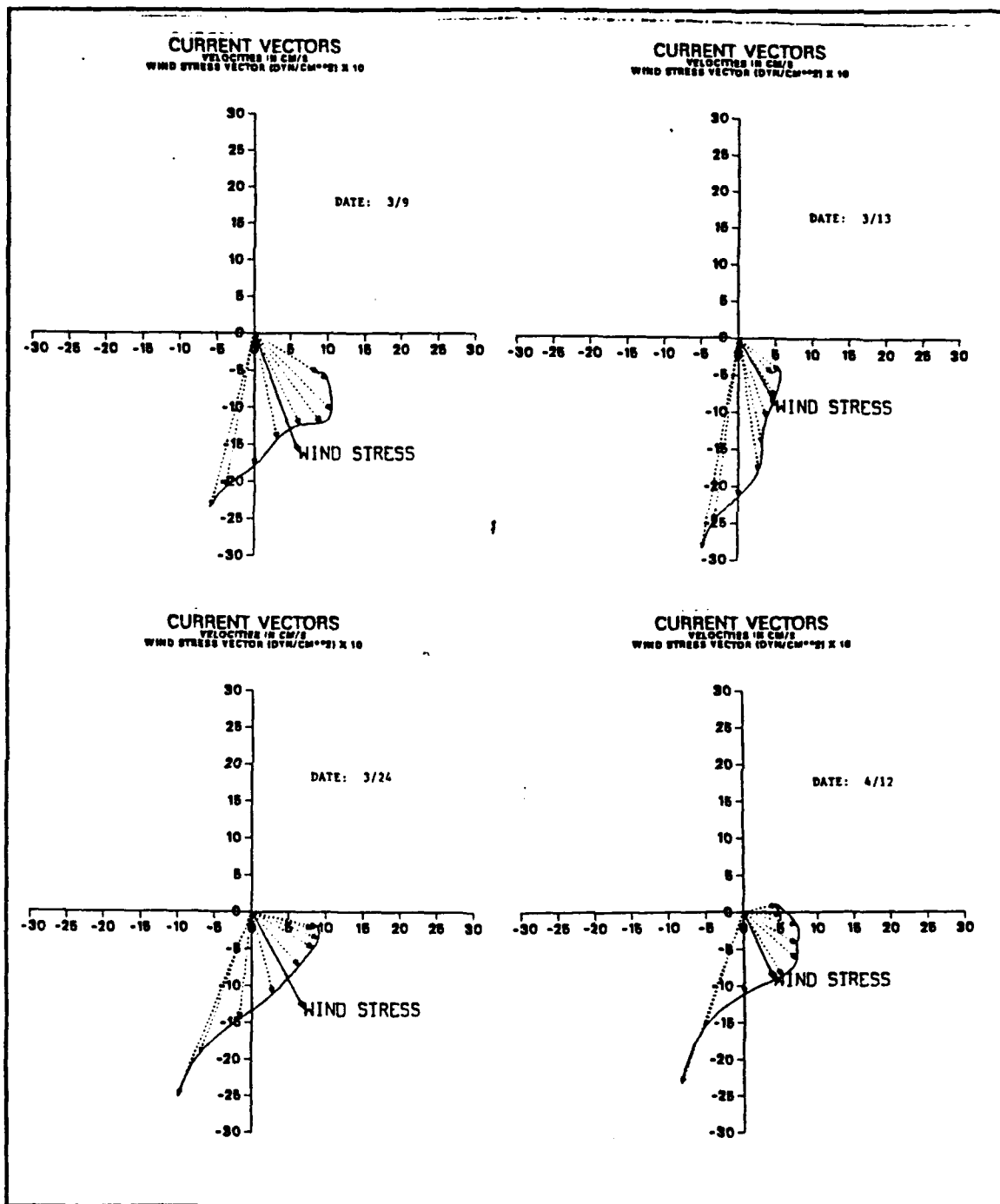
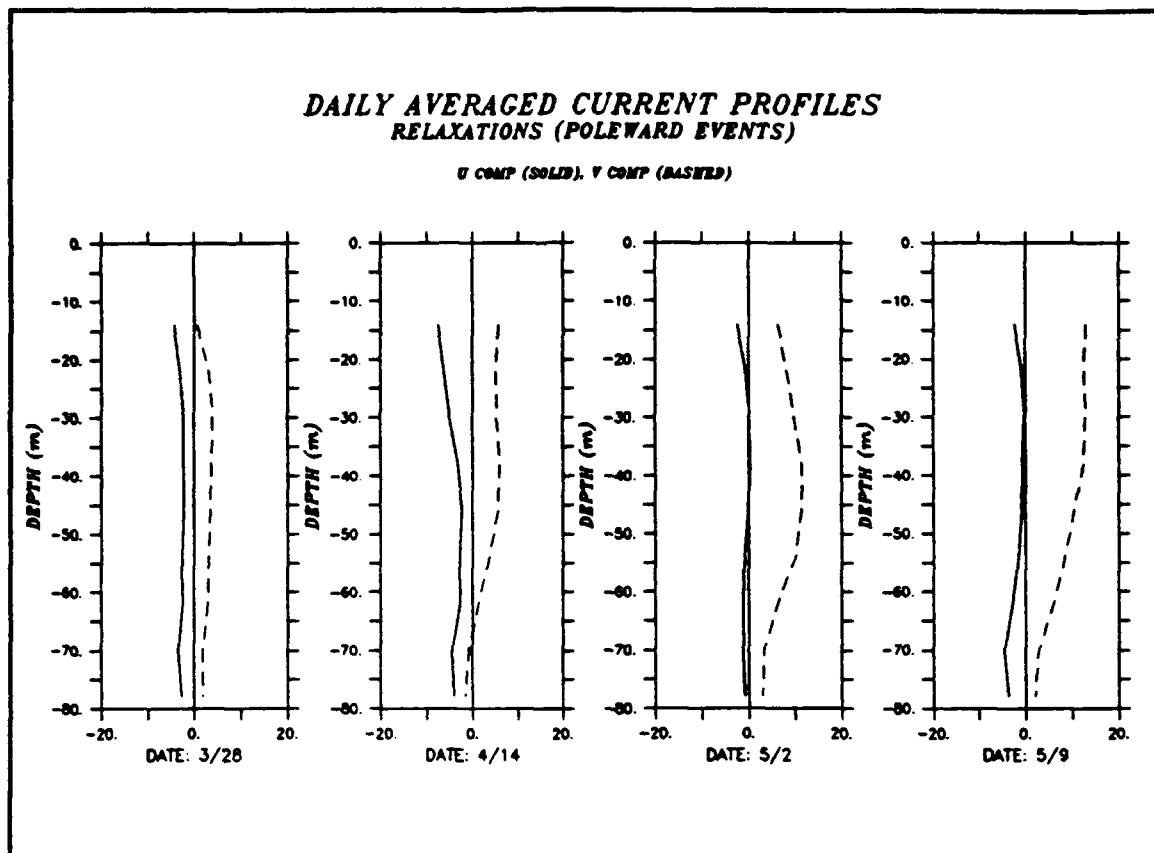


Figure 16. Daily averaged equatorward wind forced current profiles in hodograph format: The vertical current values at each depth between 14 and 80 m are projected on a horizontal plane. Current magnitude and direction are indicated by dashed vectors. Wind stress is increased by a factor of 10 for clarity and is represented by a solid vector. Velocities are in  $\text{cm s}^{-1}$ .

### C. POLEWARD EVENTS

The response of the water column during relaxations and wind reversals was significantly different than that observed during equatorward wind forcing. Four daily averaged current profiles are presented in the same format as the equatorward events, in order to examine the differences in current structure (Figure 17). The lack of strong equatorward wind forcing resulted in poleward alongshore current with magnitudes ranging from 2 - 3 cm s<sup>-1</sup> on 28 - 29 March to 10 cm s<sup>-1</sup> on 02 - 05 May and 08 - 09 May. The across-shore response showed a trend towards increasing offshore flow with increasing depth, which was more evident as the strength of the poleward alongshore flow increased with time. These profiles suggest the classical case of a uniform upper layer flow which backs to the left in an Ekman spiral once the bottom influence is felt. As the *v* - component slowed down due to the effect of the bottom friction, the Coriolis force, which is proportional to the current velocity, decreased. The pressure gradient which was driving the current is not balanced and the current will then swing left (off-shore) until the vector sum of the Coriolis and friction forces can balance the pressure induced current (Pond and Pickard, 1983). Using the depth of the Ekman spiral as an estimate of the height of the bottom boundary, values on the order of 50 - 60 m were inferred. This is consistent with the results of Lentz and Trowbridge (1991) who indicate that the bottom mixed layer can exceed 50 m in northern California coastal upwelling regions during periods of weak stratification.



**Figure 17. Daily averaged wind relaxation current profiles in component format:** The u - component of current is represented by a solid line, and the v - component by a dashed line. Velocity values are in  $\text{cm s}^{-1}$  and were measured from 14 m to 80 m.

The same events presented in hodograph format (Figure 18), showed no relation between the current structure and classical Ekman forcing. Most of the flow was oriented poleward, with a decrease in magnitude and backing to the left as a function of depth. The surface flow was not oriented to the right of the wind stress. The vectors became stronger and more northerly (as opposed to alongshore) with time.

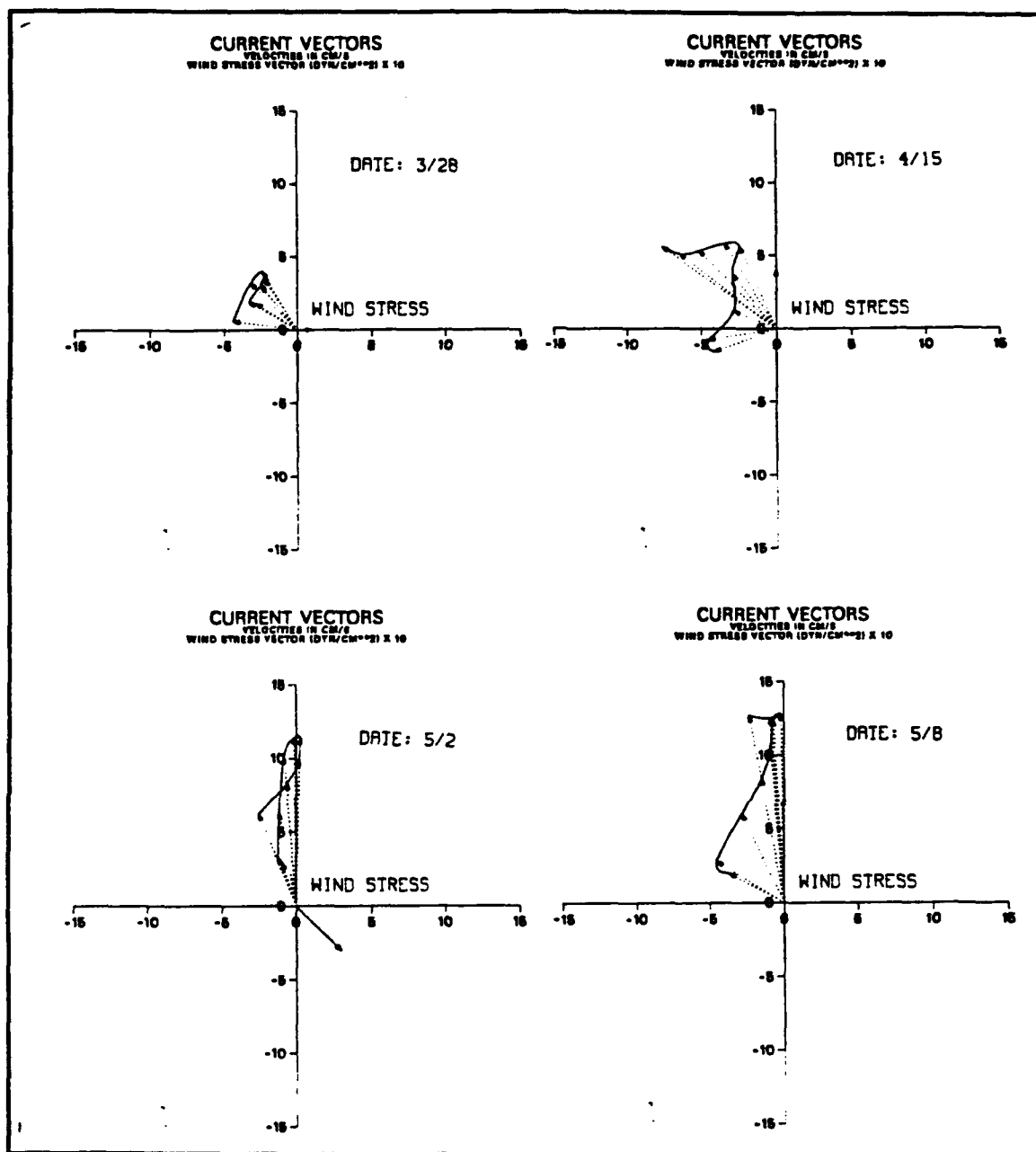


**Figure 18. Daily averaged wind relaxation current profiles in hodograph format:** The vertical current values at each depth between 14 and 80 m are projected on a horizontal plane. Current magnitude and direction are indicated by dashed vectors. Wind stress is increased by a factor of 10 for clarity and is represented by a solid vector. Velocities are in  $\text{cm s}^{-1}$ .

#### D. COHERENCE AND PHASE

To quantify the observations of strong visual correlation between alongshore wind stress ( $\tau_y$ ) and the v - component, coherence and phase were calculated for  $\tau_y$  and current in both the near surface and the mid-depth bins (Figure 19). Strong coherence (above the significance level of 0.73) between  $\tau_y$  and the 12 - 16 m depth bin were observed at frequencies lower than 0.1 cph.  $\tau_y$  and current were in phase at 0.01 cph and as the frequency increased to 0.1 cph,  $\tau_y$  leads the current. The coherence between  $\tau_y$  and the v - component at 52 - 56 m was similar except for a lack of coherence in the lowest frequency bin.  $\tau_y$  was in phase with the current up to 0.07 cph at which point  $\tau_y$  began to lead the current. There is significantly less coherence between  $\tau_y$  and the u - component at either depth. Coherence at the 12 - 16 m level was only above the significance level at 0.9 cph with the current leading  $\tau_y$ . Deeper in the water column the coherence between  $\tau_y$  and less coherence between  $\tau_y$  and the u - component at either depth. Coherence at the 12 - 16 m level was only above the significance level at 0.9 cph with the current leading  $\tau_y$ . Deeper in the water column the coherence between  $\tau_y$  and the u - component was high at low frequencies (0.01 - 0.02 cph), with the u - component roughly 180° out of phase with  $\tau_y$ .

The vertical structure of the current itself was examined with the coherence and phase between the shallowest bin at 14 m compared with progressively deeper bins. The coherence in the v - component plot (Figure 20) between 14 m and 46 m was near unity at all periods longer than about 4 days. Below 46 m there was a rapid fall-off in coherence with increasing vertical separation and below 62 m the v - component currents were uncorrelated with the 14 m bin. The correlation between the 14 m bin and progressively deeper bins in the u -

component plot (Figure 21) diminished at much shallower depths and below the 30 m level, the current was uncorrelated. The results of the spectral analysis illustrate that different structure occurred in the upper and lower part of the water column, in spite of the lack of density stratification.

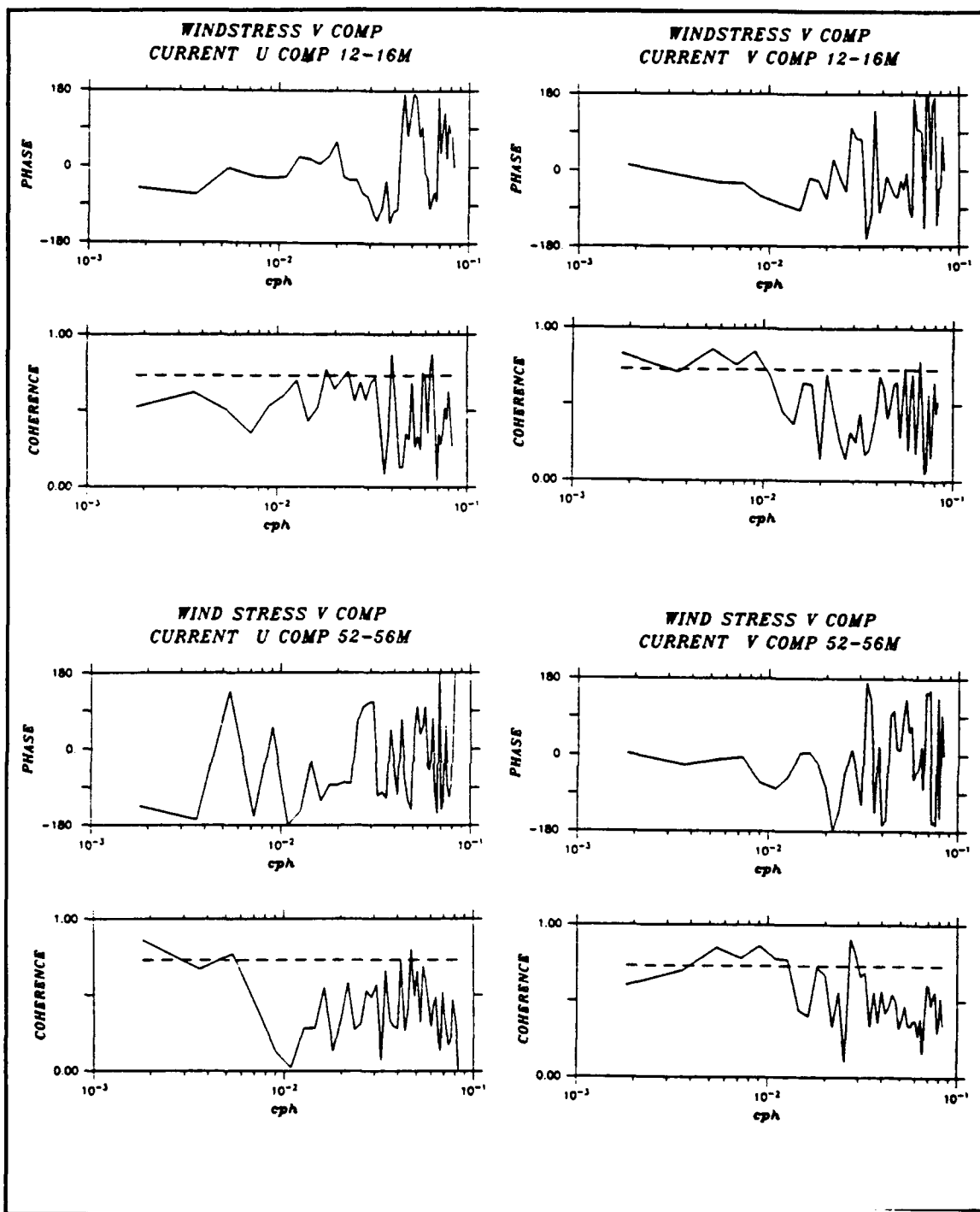


Figure 19. Coherence and phase between alongshore components of wind stress ( $\tau_y$ ) and the u and v current components at 12 - 16 m and 52 - 56 m depth: The significance level is indicated by a dashed line.



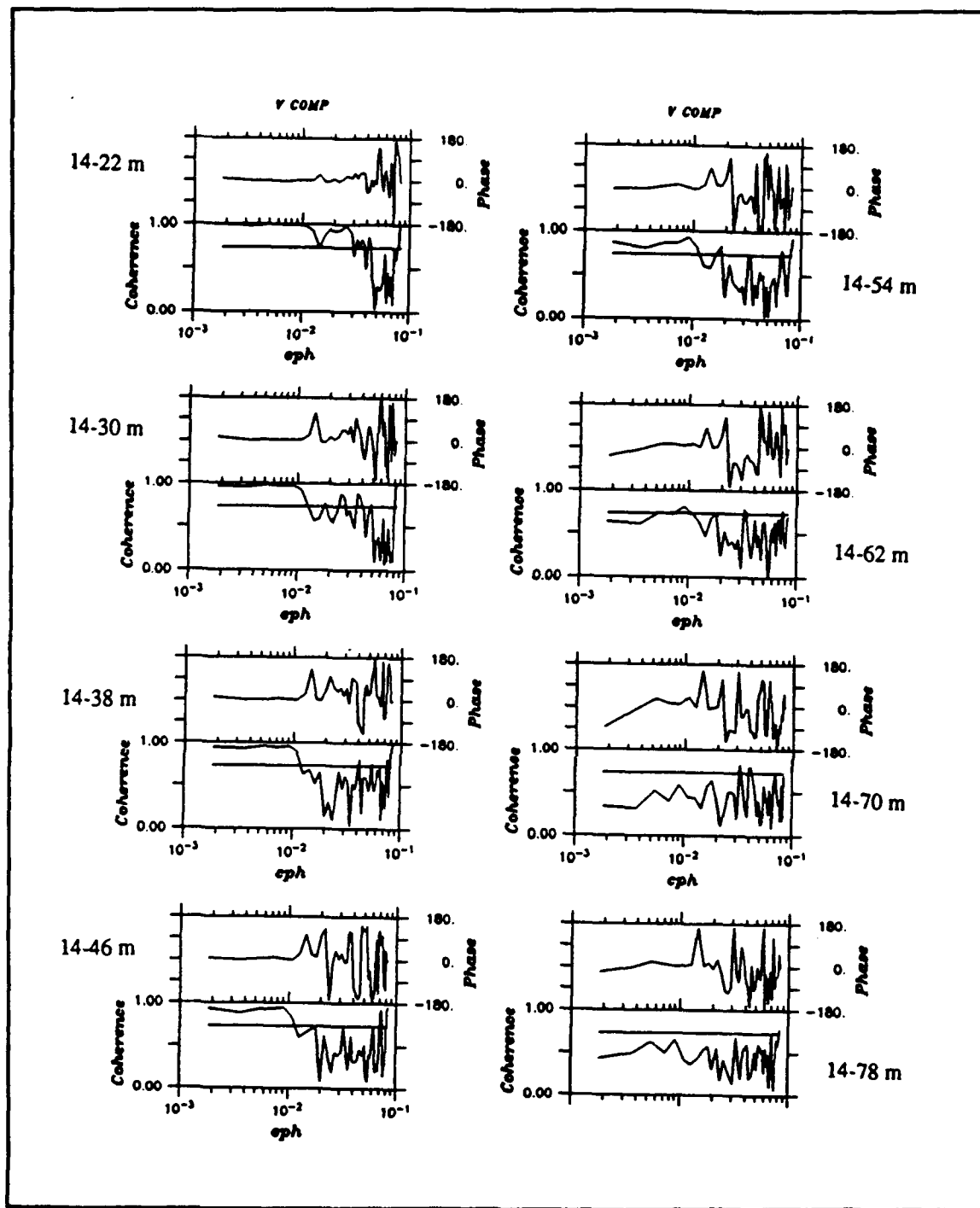
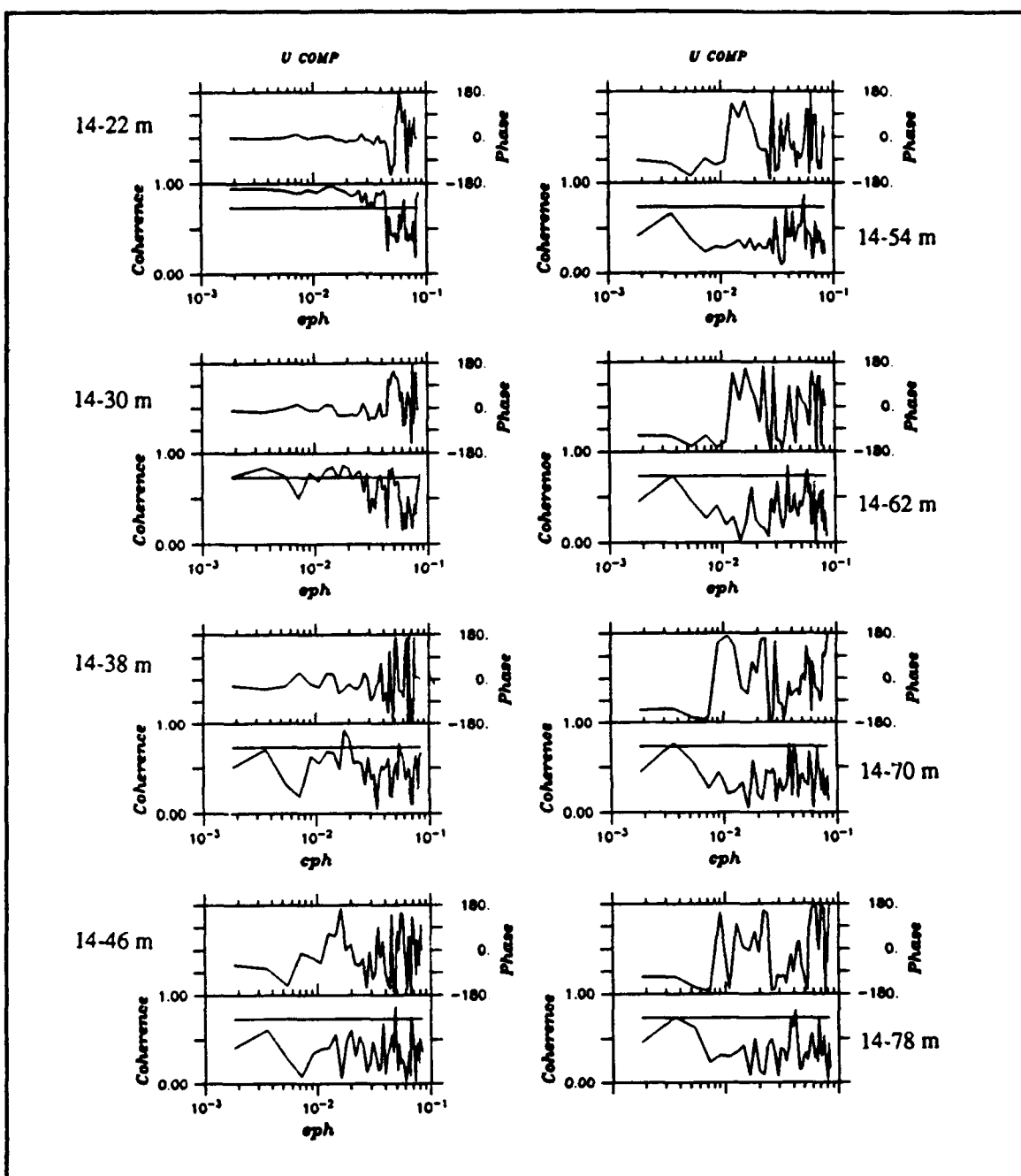


Figure 20. Coherence and phase for v current components at increasing depths: The depth bin near the surface (14 m) is compared with each successively deeper bin (in 8 m increments down to 78 m). The significance level is indicated by a solid line.



**Figure 21.** Coherence and phase for u current components at increasing depths: The depth bin near the surface (14 m) is compared with each successively deeper bin (in 8 m increments down to 78 m). The significance level is indicated by a solid line.

## VI. THEORETICAL MODEL

To describe the current off Point Sur a theoretical model forced by observed wind stress was developed. The model is an adaptation of the elementary wind forced current system near a coast model developed by Ekman (1905) and Csanady (1982). The following assumptions were made in the model: a long straight coast is oriented parallel to the  $y$  - axis; steady wind stress blows parallel to the coast with no variation in either direction; homogeneous ocean; constant eddy coefficient, and water depth greater than the Ekman depth. The requirement for a homogeneous fluid seemed justified based on two separate CTD surveys conducted on 02 May in the vicinity of the SC-ADCP. These surveys showed only weak stratification in the water column (Figure 22). It is assumed that surface heating in May was insufficient to stratify the water column in the presence of mixing by wind forcing and tidal currents. The assumption of a homogeneous ocean then will apply equally well earlier in the record when the CTD observations were made.

Steady equatorward wind stress will deflect the water in the near surface to the right, away from the coast. This Ekman transport will create a surface slope perpendicular to the coast, and an alongshore flow develops throughout the water column which is in geostrophic balance with the across-shore pressure gradient force. An adjustment drift in an across-shore  $u$  - component allows the alongshore flow to develop. As the alongshore current reaches the sea floor, the effects of friction will slow the current creating a bottom Ekman layer with enhanced across-shore velocities relative to the middle part of the water column.

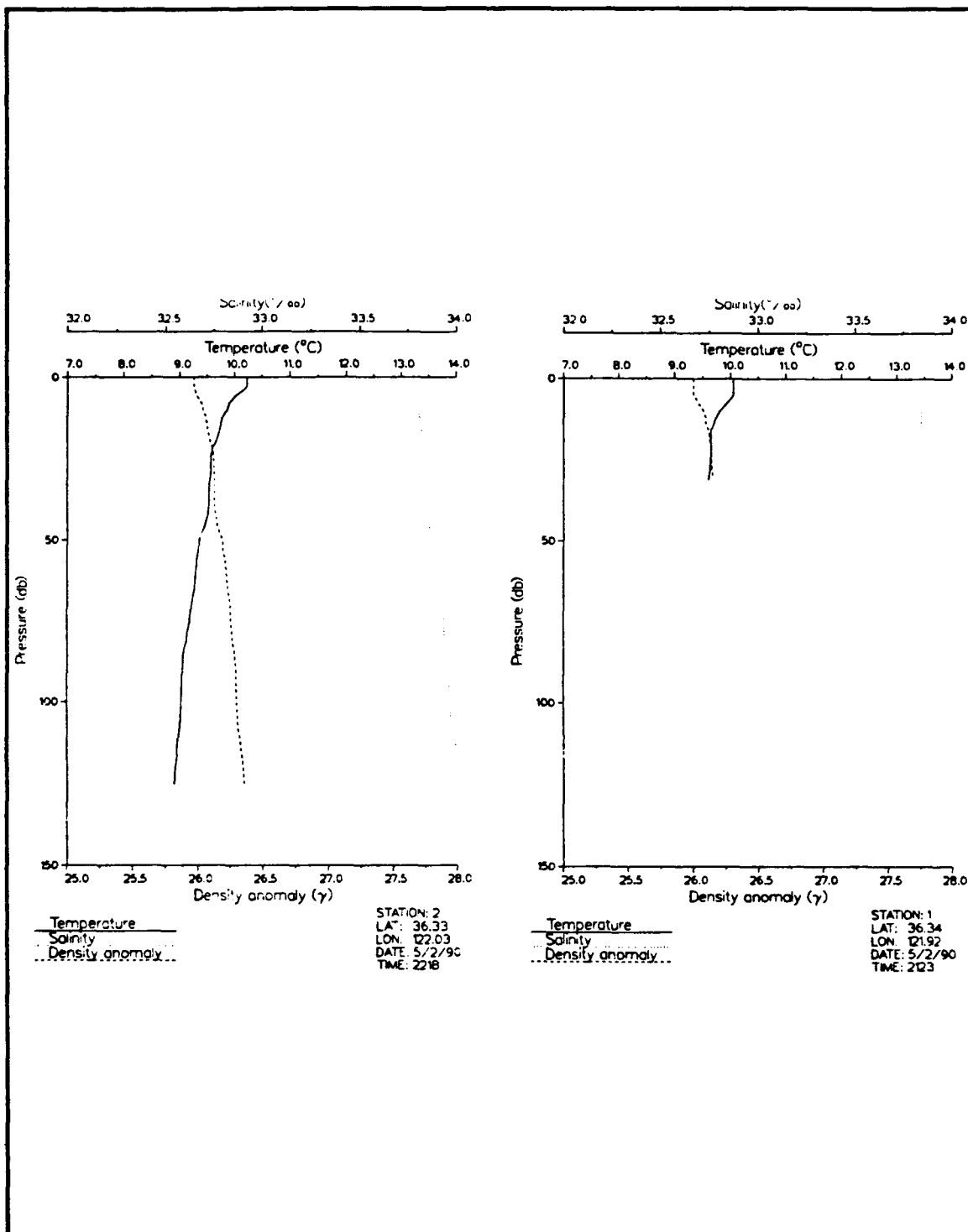


**Figure 22. CTD surveys of site P1: CTD casts were made on 02 May in the vicinity of P1.**

Following Ekman (1905), the resulting flow regime will consist of the surface and bottom Ekman layers superimposed upon the mostly geostrophic interior component (Figure 23a). The characteristics of each flow component can be identified in the accompanying hodographs. The wind stress creates a surface Ekman regime (labeled a in Figure 23b). The interior component is represented by vector (c) and will flow parallel to the coast. The bottom Ekman component (d) will develop in response to the frictional drag acting on the interior component. When the water depth varies as a function of the Ekman depth (Figure, 23c), there is a pronounced effect on the vertical structure of the current. If water depth ( $d$ ) / Ekman depth ( $D$ ) is less than 0.5 there is a loss of the surface and bottom Ekman layers and the total flow in the water column is directed parallel to the coast.

#### A. GOVERNING EQUATIONS

Since the interior and bottom components develop because of the surface Ekman flow near the coast, the surface component will be derived first followed by the interior and bottom components. It is assumed, as in Ekman (1905), that the surface layers do not feel the bottom initially, which is the usual frictionless development of the problem. It is only some time later, after geostrophic adjustment, that bottom friction becomes important. The model approach is different in that Ekman (1905) specified a surface slope rather than allowing the wind to develop it. Csanady (1982), however, in allowing the set-up by the wind to evolve properly, did not include bottom friction. This model essentially combines the two approaches and allows the wind to force the alongshore coastal current with the bottom Ekman spiral included as well.

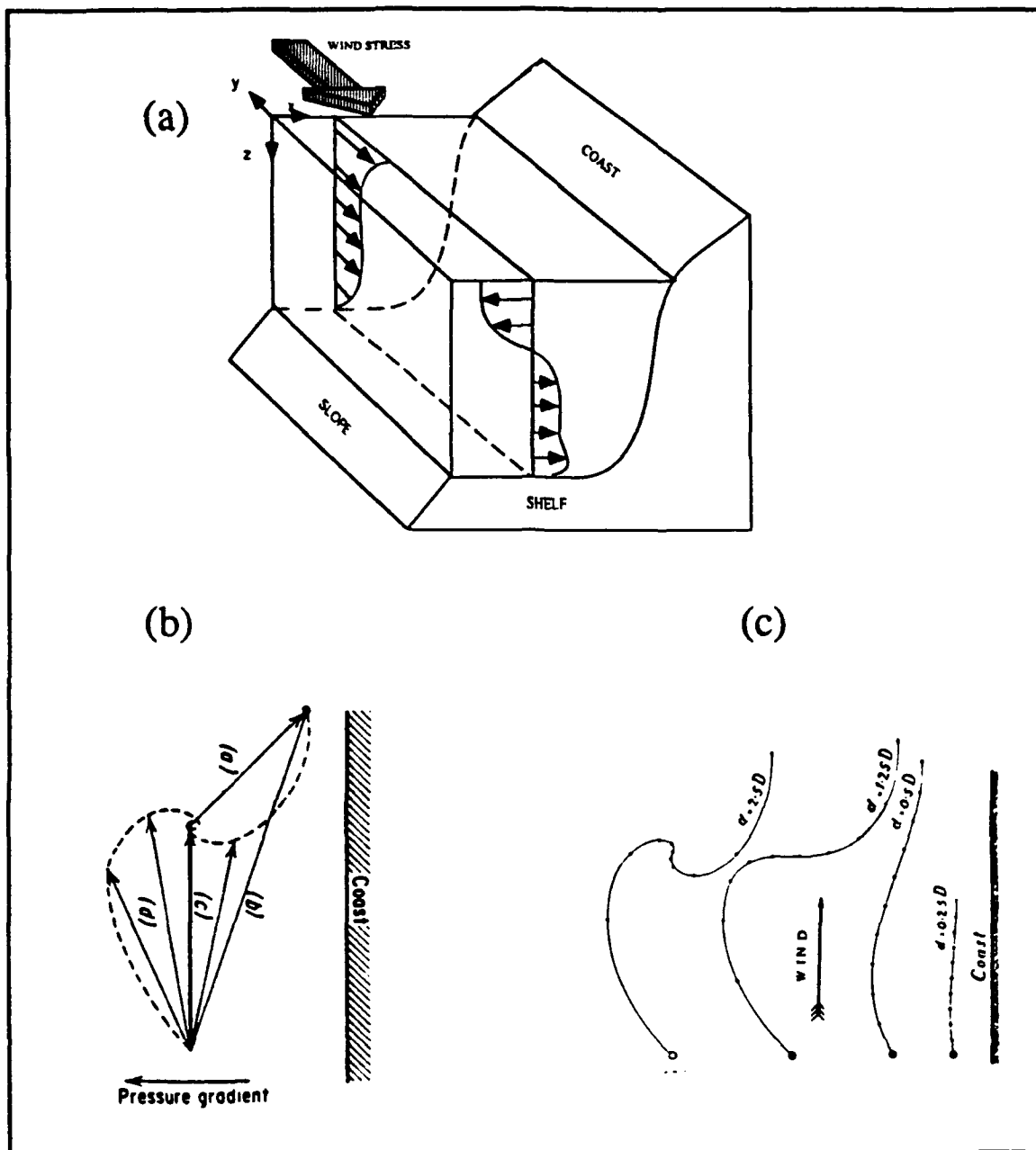


**Figure 23. Theoretical dynamic coastal current regime accompanying alongshore wind:** (a) The coastal theoretical wind driven current regime showing the  $u$  and  $v$  - component flow is presented in the top schematic. (b) The theoretical current structure is presented (left) in hodograph format, with the vectors representing velocity direction and magnitude. (from Neumann and Pierson, 1966). (c) A series of hodographs (right) are given where the vectors also represent velocity direction and magnitude and where the water depth is a function of Ekman depth (from Ekman, 1905).

## 1. Surface Component

The derivation of the of the surface wind forced component, or surface Ekman current, was done by Ekman (1905), and assumes an infinitely deep ocean. Ekman (1905), stipulates that the finite depth assumption causes small deviations from the mean value of the angle between the wind and the infinite depth case, as long as the bottom depth (H) is more than twice the Ekman depth (D). The motion occurring can be considered as it would in an infinitely deep ocean. Assuming initially a maximum Ekman depth on the order of 30 - 50 m (Brink, 1983) and a measured shelf depth of 84 m at mooring P1, the derived Ekman current based on an infinitely deep ocean should yield acceptable results.

As the Ekman equations are well known and widely used in the Oceanography community, this section will focus on the assumptions used to develop the Ekman equations from the equations of motion following Pond and Pickard (1983) and Ekman (1905). Beginning with the equations of motion

$$\begin{aligned} \frac{\partial u}{\partial t} + u \frac{\partial u}{\partial x} + v \frac{\partial u}{\partial y} + w \frac{\partial u}{\partial z} = -\alpha \frac{\partial p}{\partial x} + fv \\ + \frac{\partial}{\partial x} \left( A_x \frac{\partial u}{\partial x} \right) + \frac{\partial}{\partial y} \left( A_y \frac{\partial u}{\partial y} \right) + \frac{\partial}{\partial z} \left( A_z \frac{\partial u}{\partial z} \right) \end{aligned} \quad (1a)$$

$$\begin{aligned} \frac{\partial v}{\partial t} + u \frac{\partial v}{\partial x} + v \frac{\partial v}{\partial y} + w \frac{\partial v}{\partial z} = -\alpha \frac{\partial p}{\partial y} - fu \\ + \frac{\partial}{\partial x} \left( A_x \frac{\partial v}{\partial x} \right) + \frac{\partial}{\partial y} \left( A_y \frac{\partial v}{\partial y} \right) + \frac{\partial}{\partial z} \left( A_z \frac{\partial v}{\partial z} \right) \end{aligned} \quad (1b)$$

$$\begin{aligned} \frac{\partial w}{\partial t} + u \frac{\partial w}{\partial x} + v \frac{\partial w}{\partial y} + w \frac{\partial w}{\partial z} = - \alpha \frac{\partial p}{\partial z} - g \\ + \frac{\partial}{\partial x} \left( A_x \frac{\partial w}{\partial x} \right) + \frac{\partial}{\partial y} \left( A_y \frac{\partial w}{\partial y} \right) + \frac{\partial}{\partial z} \left( A_z \frac{\partial w}{\partial z} \right) \end{aligned} \quad (1c)$$

where  $A_x$ ,  $A_y$ , and  $A_z$  are the respective eddy coefficients with the specific volume anomaly  $\alpha = 1 / \rho$ .

Equations (1a), (1b), and (1c) contain non-linear terms and generally are not explicitly solvable. By scaling these equations utilizing rough estimates of the size of each, neglecting the non-linear terms, and only considering frictional forcing acting in the vertical direction, it is possible to neglect components of equations (1a), (1b), and (1c) leaving the remaining terms to describe the actual motion. Considering only the horizontal equations of motion, equations (1a) and (1b) become,

$$fv = \alpha \frac{\partial p}{\partial x} - A_z \frac{\partial^2 u}{\partial z^2} \quad (2)$$

$$fu = - \alpha \frac{\partial p}{\partial y} - A_z \frac{\partial^2 v}{\partial z^2} \quad (3)$$

There are two causative forces for motion in equations (2) and (3), the distribution of mass (density) which gives rise to pressure terms and the wind friction terms. If the velocity is considered having two parts, one associated with the horizontal pressure gradient and the other with momentum transferred by vertical friction, each can be solved for separately and then reconstructed. Taking the  $u$  - component equation (2)



$$fv = f(v_g + v_e) = \alpha \frac{\partial p}{\partial x} - A_z \frac{\partial^2}{\partial z^2}(u_g + u_e) \quad (4)$$

where

$$fv_g = \alpha \frac{\partial p}{\partial x}$$

$u_g, v_g$  are Ekman velocity components

and

$$fv_e = -A_z \frac{\partial^2(u_g + u_e)}{\partial z^2}$$

$u_e, v_e$  are Ekman velocity components associated with vertical shear friction

As the water is assumed homogeneous and there is no initial surface slope, the pressure terms are equivalent to zero and therefore  $u_g$  and  $v_g$  are zero. Similar arguments apply to the  $v$  - component equation. The resulting Ekman equations are:

$$fv_e + A_z \frac{\partial^2 u_e}{\partial z^2} = 0 \quad (5)$$

$$-fu_e + A_z \frac{\partial^2 u_e}{\partial z^2} = 0 \quad (6)$$

The solutions to equations (5) and (6) are well known (Ekman, 1905; Neumann and Pierson, 1966; Pond and Pickard, 1983) and yield

$$u = V_0 e^{\left(\frac{\pi}{D}\right)z} \cos\left(\frac{\pi}{4} - \frac{\pi}{D}z\right) \quad (7)$$

$$v = V_0 e^{\left(\frac{\pi}{D}\right)z} \sin\left(\frac{\pi}{4} - \frac{\pi}{D}z\right) \quad (8)$$

where

$$D = \text{Ekman Depth} = \pi \sqrt{\frac{2A_z}{\rho f}} \quad (9)$$

and

$$V_0 = \text{Surface Current Velocity} = \frac{\tau_y}{\sqrt{\rho A_z f}}$$

• Equations (7) and (8) are the  $u$  and  $v$  - component currents for the surface Ekman layer. From these equations it is observed that at  $z = 0$ ,

$$u = V_0 \cos 45^\circ$$

$$v = V_0 \sin 45^\circ$$

or that the surface current will develop oriented  $45^\circ$  to the right of the stress in the Northern Hemisphere. By varying  $z$  the Ekman Spiral will be produced for the pure wind driven current.

The Ekman current has a maximum speed at the surface and decreases with increasing depth. If equations (7) and (8) are integrated over the Ekman depth ( $D$ ), the important transport equations are given as

$$T_x = \frac{\tau_y}{\rho f} \quad \text{and} \quad T_y = 0 \quad (10)$$

All the transport in the Ekman layer due to the alongshore wind stress is in the across-shore direction. This has important implications for coastal upwelling as described next.

## 2. Interior Component

Surface Ekman drift in the presence of a coast will create pressure forces in the interior of the fluid. Following the derivation of Csanady (1982), the interior component will be shown to consist of an alongshore geostrophic flow and an "adjustment drift" current in the across-shore direction. The horizontal transport equations are

$$\frac{\partial U}{\partial t} - fV = c^2 \frac{\partial \zeta}{\partial x} + F_x - B_x \quad (11)$$

$$\frac{\partial V}{\partial t} + fU = c^2 \frac{\partial \zeta}{\partial y} + F_y - B_y \quad (12)$$

$$\frac{\partial U}{\partial x} + \frac{\partial V}{\partial t} = - \frac{\partial \zeta}{\partial t} \quad (13)$$

where  $c^2 = gH$ ,  $(F_x, F_y)$  are the kinematic surface wind stress components, and  $(B_x, B_y)$  are the kinematic bottom stress components.

Differentiating (11) with respect to  $y$ , (12) with respect to  $x$ , subtracting (12) from (11), and substituting (13) into the resulting equation yields

$$\frac{\partial}{\partial t} \left( \frac{\partial V}{\partial x} - \frac{\partial U}{\partial y} \right) = f \frac{\partial \zeta}{\partial t} + \frac{\partial}{\partial x} (F_y - B_y) - \frac{\partial}{\partial y} (F_x - B_x) \quad (14)$$

This is the depth integrated analog of the linearized potential vorticity equation. With the spatial variability of the wind stress and bottom stress ignored, and the motion starting from rest, ( $z = 0$  at  $t = 0$ ), equation (14) becomes

$$\frac{\partial V}{\partial x} - \frac{\partial U}{\partial y} = f \zeta \quad (15)$$

Differentiating (11) with respect to  $x$  and (12) with respect to  $y$ , summing and substituting into (13) yields

$$\frac{\partial^2 \zeta}{\partial t^2} - c^2 \nabla^2 \zeta + f^2 \zeta = 0 \quad (16)$$

Transports are now found by assuming a coast parallel to the  $y$  - axis, with alongshore wind in the (+)  $y$  direction imposed at  $t = 0$ . Neglecting bottom friction, the boundary condition at  $t = 0$ , is

$$\begin{aligned} F_x &= 0 & B_x &= 0 \\ F_y &= u_*^2 & B_y &= 0 \end{aligned}$$

Substituting into equations (11) and (12)

$$\frac{\partial U}{\partial t} - fV = -c^2 \frac{\partial \zeta}{\partial x} \quad (17)$$

$$\frac{\partial V}{\partial t} + fU = u_*^2 \quad (18)$$

Imposing the boundary condition at the coast,  $U = 0$ , and starting the motion from rest equation (17) and (18) yield

$$V = u_*^2 t \quad (x = 0) \quad (19)$$

$$\frac{\partial \zeta}{\partial x} = f t \frac{u_*^2}{c^2} \quad (20)$$

Equation (19) represents the flow that would result if no rotation were present. The fluid near the coast simply accelerates downwind. Equation (20) shows that the developing sea surface slope  $\frac{\partial \zeta}{\partial x}$  is a function of the wind duration, magnitude and the free wave speed  $c^2 = gH$ .

To establish the pressure field, the full solution of the *impulsively forced* problem, equation (16), is found using Laplace Transform methods (Crépon, 1967) the result for the free surface elevation is

$$\zeta = u_*^2 \int_0^t J_0 \left[ f \sqrt{t^2 - \frac{x^2}{c^2}} \right] Y \left( t + \frac{x}{c} \right) dt \quad (21)$$

where  $J_0$  is a Bessel function and  $Y(\lambda)$  is the Heavyside function ( $Y = 1, \lambda > 0, Y = 0, \lambda < 0$ ). A long time after the imposition of the wind stress equation (21) may be expressed as

$$\zeta = \frac{u_*^2}{fc} \left[ (ft) e^{x/R} - \frac{\sqrt{2}}{\pi} \cos \frac{(ft - \frac{\pi}{4})}{\sqrt{ft}} + \dots \right] \quad ft \gg 1 \quad (22)$$

steady                  oscillatory

which is the pressure field described by a flow confined to a coastal band of scale width  $R$ . The steady amplitude will increase linearly with time and the oscillatory part will decay with time.

The non-oscillatory part of (22) is:

$$\zeta = \frac{u_*^2}{c} t e^{x/R} \quad (23)$$

where  $x$  is the distance from the coast and  $R$  is the external Rossby radius of deformation given as

$$R = \frac{\sqrt{gH}}{f}$$

The alongshore transport is found by differentiating  $\zeta$  with respect to  $x$

$$\frac{\partial \zeta}{\partial x} = \frac{1}{R} t \frac{u_*^2}{c} e^{x/R} \quad (24)$$

and substituting into equation (17) at  $x = 0$  and  $U = 0$ .

This yields 
$$V = u_*^2 t e^{x/R} \quad (25)$$

where  $R = c/f$ . Using equation (25) and (18) gives the integrated across-shore transport

$$U = \frac{u_*^2}{f} (1 - e^{x/R}) \quad (26)$$

Equations (23) and (25) with

$$fV = c^2 \frac{\partial \zeta}{\partial x}$$

show that the alongshore transport  $V$  is in geostrophic balance with the pressure field, not only at the coast but everywhere in the coastal band of scale width  $R$ . Far from the coast,  $V$  goes to zero as the sea surface goes to zero. There is also significant across-shore transport  $U$ , over most of the coastal band except very near the coast where  $x/R \ll 1$ . The  $U$  transport builds up according to the time scale  $f^{-1}$ , which at this latitude is 20 hours, and since there is no along-shore pressure gradient,  $U$  is not in geostrophic balance. Near the coast where  $U$  is approximately zero the wind will only accelerate the water alongshore. Far from the coast  $U = \frac{u_*^2}{f}$ , the Coriolis force associated with the Ekman drift balances the wind stress and only surface, Ekman flow will develop. In between, the flow transitions smoothly between the two states (Figure 24).

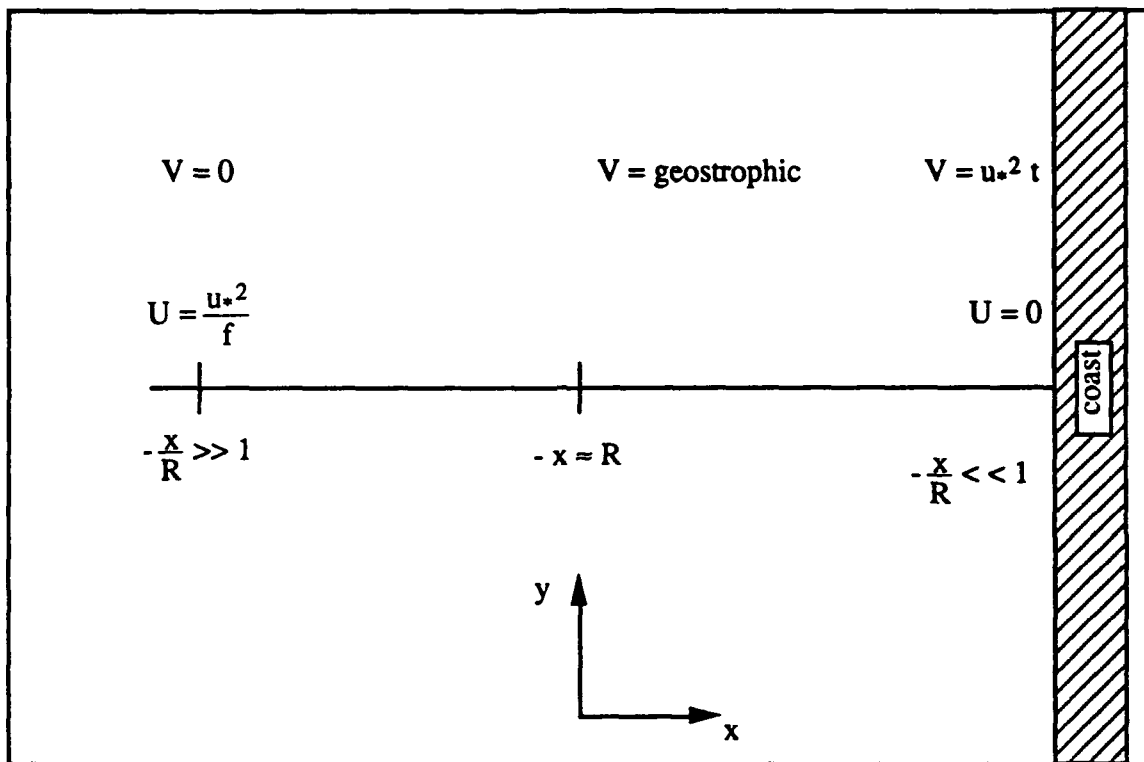


**Figure 24. Coastal transport schematic:** Alongshore transport ( $V$ ) is in geostrophic balance within the coastal band from the coast to  $-x/R \gg 1$ . There is also significant across-shore transport ( $U$ ) over most of the coastal band except very near the coast where  $-x/R \ll 1$ .



The solutions to the previous equations have yielded the local sea level gradients

$$\frac{\partial \zeta}{\partial x} ; \frac{\partial \zeta}{\partial y}$$

which are the depth independent forcing terms of equations (16) and (17).

At this point the interior velocity distribution will be considered and the local solutions examined for equations (16) and (17). These solutions  $u(z,t)$  and  $v(z,t)$  which depend parametrically on  $x$  are written as

$$u = u_1(t) + u_2(z,t) \quad (27)$$

$$v = v_1(t) + v_2(z,t) \quad (28)$$

where  $u_1(t)$  and  $v_1(t)$  is a solution to equation (16) and (17) with the stress gradient terms deleted.

$$\frac{\partial u_1}{\partial t} - f v_1 = -g \frac{\partial \zeta}{\partial x} \quad (29)$$

$$\frac{\partial v_1}{\partial t} + f u_1 = -g \frac{\partial \zeta}{\partial y} \quad (30)$$

Earlier it was shown that the global solution yielded depth-integrated transports  $U$  and  $V$ . Equations (27) and (28) will also apply to the transports, so with the components  $u_1(t)$  and  $v_1(t)$  independent of depth, the equations for the interior velocity distribution become

$$u_1 = \frac{1}{H} (U - U_2) \quad (31)$$

$$v_1 = \frac{1}{H}(V - V_2) \quad (32)$$

To solve for the interior velocity, two steps are involved. The frictionally induced transport ( $U_2$  and  $V_2$ ) must be calculated. The pressure induced interior velocities are then solved by subtracting ( $U_2$  and  $V_2$ ) from the total transport components ( $U$  and  $V$ ). The frictionally induced transport components (the Ekman transport), are derived from the global solutions to equations (16) and (17) as

$$fV = 0$$

$$fU = F$$

$$\frac{\partial U}{\partial x} + \frac{\partial V}{\partial y} = 0$$

which are satisfied by

$$U_2 = \frac{u_*^2}{f}$$

$$V_2 = 0$$

where  $F = u_*^2$

Solving for  $u_1$  and  $v_1$  from equations (29) and (30) yield the pressure field induced velocities

$$u_1 = -\frac{u_*^2}{fH} e^{x/R} \quad (33)$$

$$v_1 = \frac{u_*^2}{H} t e^{x/R} \quad (34)$$

Equations (33) and (34) are functions of  $\exp(x/R)$  which determines the coastal decay scale length. This is the region where wind stress acting alongshore indirectly produces a current in its own direction. For site P1, moored 5 km off the coast,  $\exp(x/R) = \exp(5/330) = 1.0$ , so P1 is well within the coastal band where these dynamics apply. Therefore  $u_1$  is simply the adjustment drift and  $v_1$  is the geostrophic transport generated by the wind stress acting over time ( $t$ ). Referring to equation (30) and taking  $\frac{\partial \zeta}{\partial y} = 0$ , the alongshore geostrophic component must be generated by an appropriate across-shore motion during a spin-up period which occurs on a time scale  $f^{-1}$ . This equates to a spin-up time on the order of about 20 hours at  $36^\circ 20' N$  latitude.

After initial set-up, the magnitude of  $v_1$  will increase as long as forcing continues. In the frictionless case, the current acceleration can be infinite however, when bottom friction is introduced, the surface stress will at some point be balanced by bottom stress and the current will no longer accelerate. In this case the bottom stress ( $B_y$ ) will be equivalent to surface stress ( $\tau_y$ ) and is given by

$$\tau_y = B_y = v^2 C_D \quad (35)$$

where  $v$  is the near bottom velocity in the alongshore direction and  $C_D$  is the drag coefficient. Observed LLP values of the  $v$  - component in the deepest depth bin are on the order of  $10 \text{ cm s}^{-1}$ , however, to obtain a more accurate estimation of the  $v$  - component, including tidal contributions, unfiltered (15 min) current data were analyzed. Typical near-bottom maximum  $v$  - component values of order  $20 \text{ cm s}^{-1}$  were observed throughout the record. This range of velocities, when used with a surface stress of  $1.0 \text{ dyn cm}^{-2}$  in equation (35) yields a range of values for  $C_D$  from  $2.5 - 10 \times 10^{-3}$ . These values are slightly higher than the  $C_D$  used by Trowbridge and Lentz (1991), but within the range of values reported in Table 2 of Grant et al. (1983).

### 3. Bottom Component

In order to develop a more realistic model of the shelf flow, a bottom Ekman spiral is allowed to form (Ekman, 1905; Pond and Pickard, 1983). Assuming a constant  $A_z$ , the current flowing over the sea floor will generate an Ekman spiral above the bottom to a height  $D$  equal to the depth of the surface Ekman spiral however, the bottom spiral backs counter-clockwise with depth, rather than clockwise. The Ekman equations (5) and (6) will still apply but the boundary conditions will be different. At the bottom the velocity must vanish, ( $u = 0, v = 0$ ) and must reach a constant value some distance above the frictional layer. Assuming this layer, above the frictional layer, is in geostrophic balance it is then independent of  $z$ . Taking  $u = 0$  and  $v = v_g$  in the geostrophic region the solution to (5) and (6) with the new boundary currents gives

$$u_b = \frac{u_*^2 t}{H} e^{x/R} [(e^{-\pi z/D}) \sin(\pi z/D)]$$

$$v_b = \frac{u_*^2 t}{H} e^{x/R} [(e^{-\pi z/D}) \cos(\pi z/D)]$$

where D is the bottom Ekman layer height defined by (9) as before and z is now the height above the bottom.

#### 4. Solutions

The total solution will be the sum of the surface, interior, and bottom layers:

$$u(x, z, t) =$$

$$V_0 e^{\left(\frac{\pi}{D}\right)z} \cos\left(\frac{\pi}{4} - \frac{\pi}{D}z\right) - \frac{u_*^2}{H} t e^{x/R} - \frac{u_*^2 t}{H} e^{x/R} [(e^{-\pi(H-z)/D}) \sin(\pi(H-z)/D)] \quad (36a)$$

(surface Ekman)      (adjustment drift)      (bottom Ekman)

$$v(x, z, t) =$$

$$V_0 e^{\left(\frac{\pi}{D}\right)z} \sin\left(\frac{\pi}{4} - \frac{\pi}{D}z\right) - \frac{u_*^2}{H} t e^{x/R} - \frac{u_*^2 t}{H} e^{x/R} [(e^{-\pi(H-z)/D}) \cos(\pi(H-z)/D)] \quad (36b)$$

(surface Ekman)      (geostrophic)      (bottom Ekman)

The u and v - component equations will consist of contributions from both surface and bottom Ekman components. The u - component will also contain an adjustment drift contribution and the v - component, a geostrophic contribution in the interior. Where the bottom Ekman part has been re-written so that z is positive downward from the surface as it is in the surface Ekman layer.

## B. RESULTS

The initial input variables for the governing equations were chosen based on observations taken from the 08 - 09 March equatorward wind event. The surface stress is computed by averaging the wind stress between 08 and 09 March. The initial choice of  $A_z$  is computed from the solution of (9) using a value of  $D$  estimated as the zero crossing point (about 30 m) in the  $u$  (across-shore) velocity component. This is based on two-dimensional upwelling theory which stipulates that offshore transport due to alongshore wind stress must be balanced by onshore transport below the Ekman layer (Brink, 1983). Using this procedure a value of  $A_z = 4.5 \times 10^{-3}$  was computed. The initial duration of the wind event was chosen as 20 hours (the required initial spin-up time) but longer values may be appropriate.

The hodograph of the resulting theoretical vertical velocity field clearly shows the current structure of the three flow regimes (Figure 25). With the wind stress acting along the (-)  $y$  axis parallel to the coast, a near surface Ekman layer develops to the right of the wind stress vector. As this Ekman layer is superimposed on the alongshore pressure driven velocity field, the magnitude of the current does not go to zero with depth rather, it approaches the magnitude of the geostrophic interior current. The usual clockwise turning of the Ekman spiral is also suppressed by the geostrophic component. Thus the uniform interior current is represented by a bunching of the current vectors at mid-depth in the general direction of the wind stress at a magnitude of  $20 - 25 \text{ cm s}^{-1}$ . As the interior current begins to feel the bottom, friction causes a decrease in magnitude and the current vectors respond to this and veer counter-clockwise. The deepest

vector plotted is at 78 m to match observations, although the theoretical hodograph does back to zero at the bottom.

The theoretical results are compared with the observed results in the component plot (Figure 26). The model reproduced the general structure of the current quite well. The  $v$  - component is equatorward throughout the water column and the  $u$  component transitions from off-shore to on-shore in the near

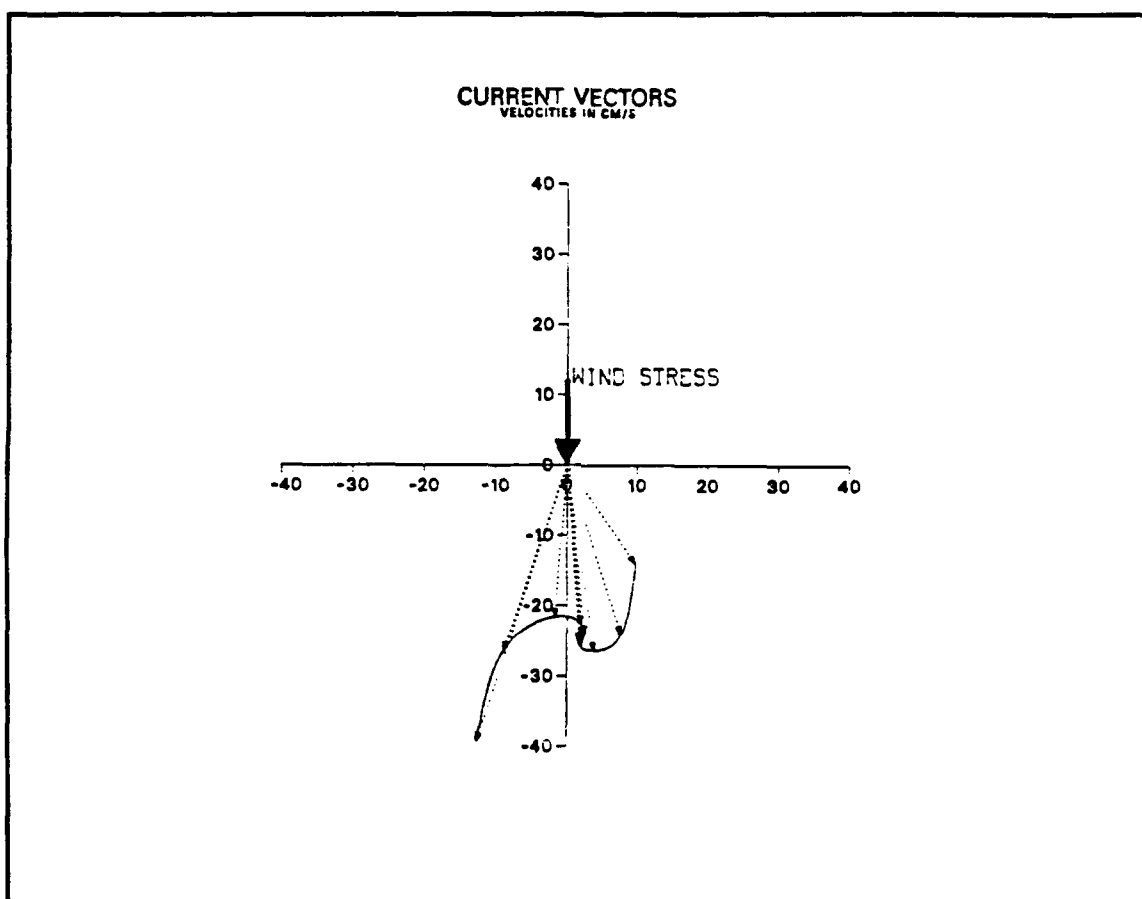


**Figure 25.** Theoretical current structure: Current direction and magnitude, at depth increments of 8 m starting at the surface, are represented by dashed vectors and presented in hodograph format. The wind stress is indicated by a thick vector pointing down with the magnitude increased by a factor of 10 for comparison. The units of wind stress are  $\text{dyn cm}^{-2}$ , and the units of velocity are in  $\text{cm s}^{-1}$ .

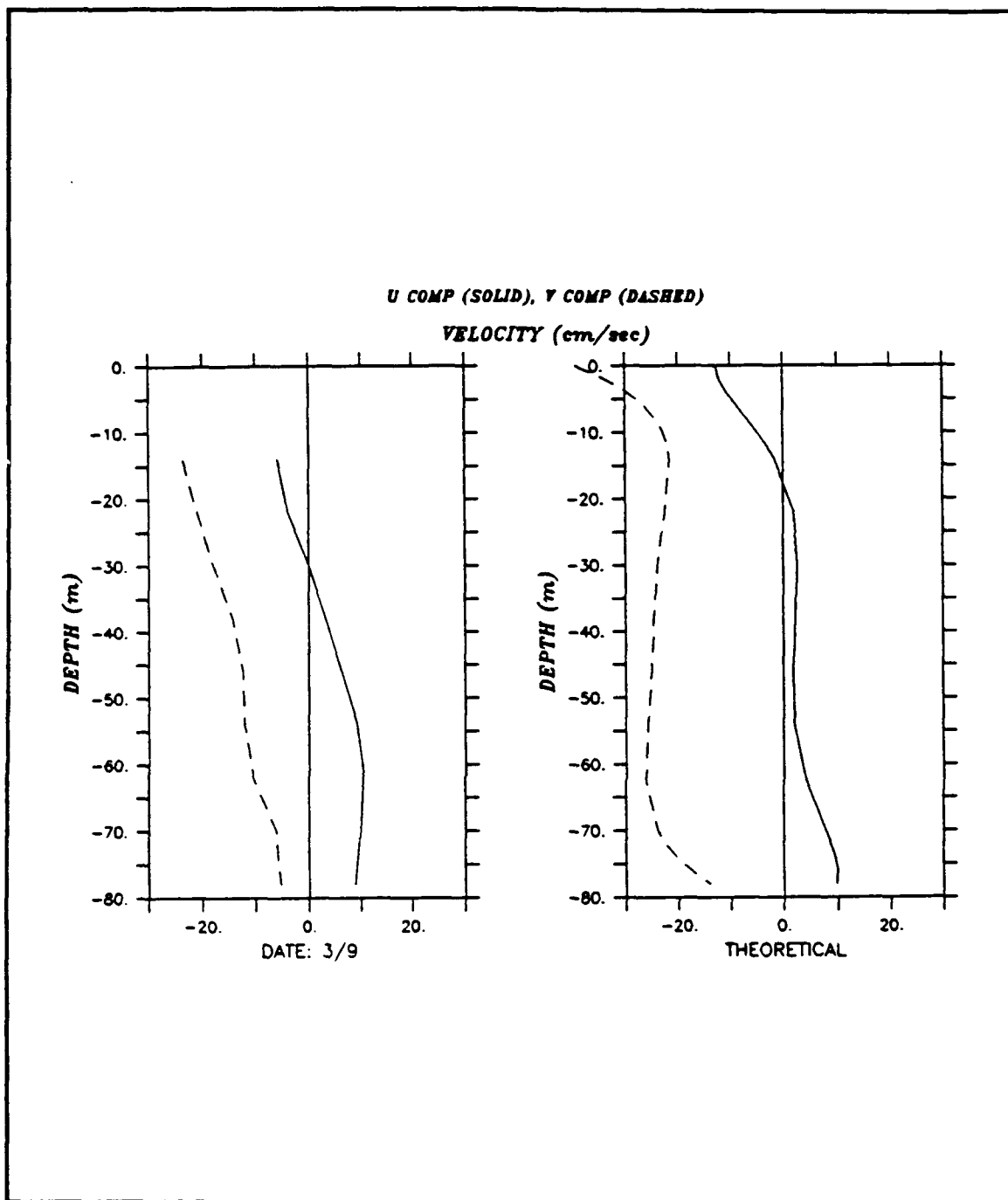


**Figure 26. Theoretical current vs observed current:** The theoretical current is based on inputs taken from the 9 March observations and is compared with the observed current structure on the same date. The u - component is represented by a solid line the v - component by a dashed line. Theoretical current components are plotted from the surface to 80 m (8 m increments).



surface, both with about the right magnitude. The  $u$  and  $v$  - components of the model however, do not possess all the characteristics of the observed flow. The observed  $u$  and  $v$  - components do not possess the constant magnitude interior regime that is present in the model, and both are sheared in the interior portion of the water column.

The initial solution of the model was based on an estimate of a constant  $A_z$ . As  $A_z$  is a property of the ambient conditions of the water column rather than the fluid itself, the initial estimate may vary. Complicated bathymetry in the vicinity of P1 and the lack of stratification in the water column indicate that a larger value of  $A_z$  may be more appropriate. Utilizing  $A_z$  as a tuning parameter for the model, the solutions to the governing equations (36a and 36b) were repeated for different values of  $A_z$ , all else being the same. Figure 27 is a component plot of the theoretical current showing the effect of increasing  $A_z$  from  $2.1 \times 10^{-3}$  to  $26.4 \times 10^{-3} \text{ m}^2 \text{ s}^{-1}$ . By increasing  $A_z$ , more velocity is diffused into the interior with an associated loss of the constant velocity interior signatures of the  $u$  and  $v$  components observed in the initial model. Note also that the transition depth between off-shore and on-shore flow stabilizes at 25 - 30 m, which means that this cross over point is actually a poor indicator of the Ekman depth ( $D$ ) when bottom stress is included in the model and the water is not very deep.

A value of  $A_z$  of  $12.6 \times 10^{-3} \text{ m}^2 \text{ s}^{-1}$  was chosen as input for the best-fit solution because it most accurately represented the  $u$  - component and greater values of  $A_z$  caused shoaling of the transition level between off-shore and on-shore flow. Substituting this value of  $A_z$  into the governing equations results in the hodograph presented in Figure 28. The vectors now back smoothly counter-clockwise with depth as the surface and bottom Ekman layers merge into one

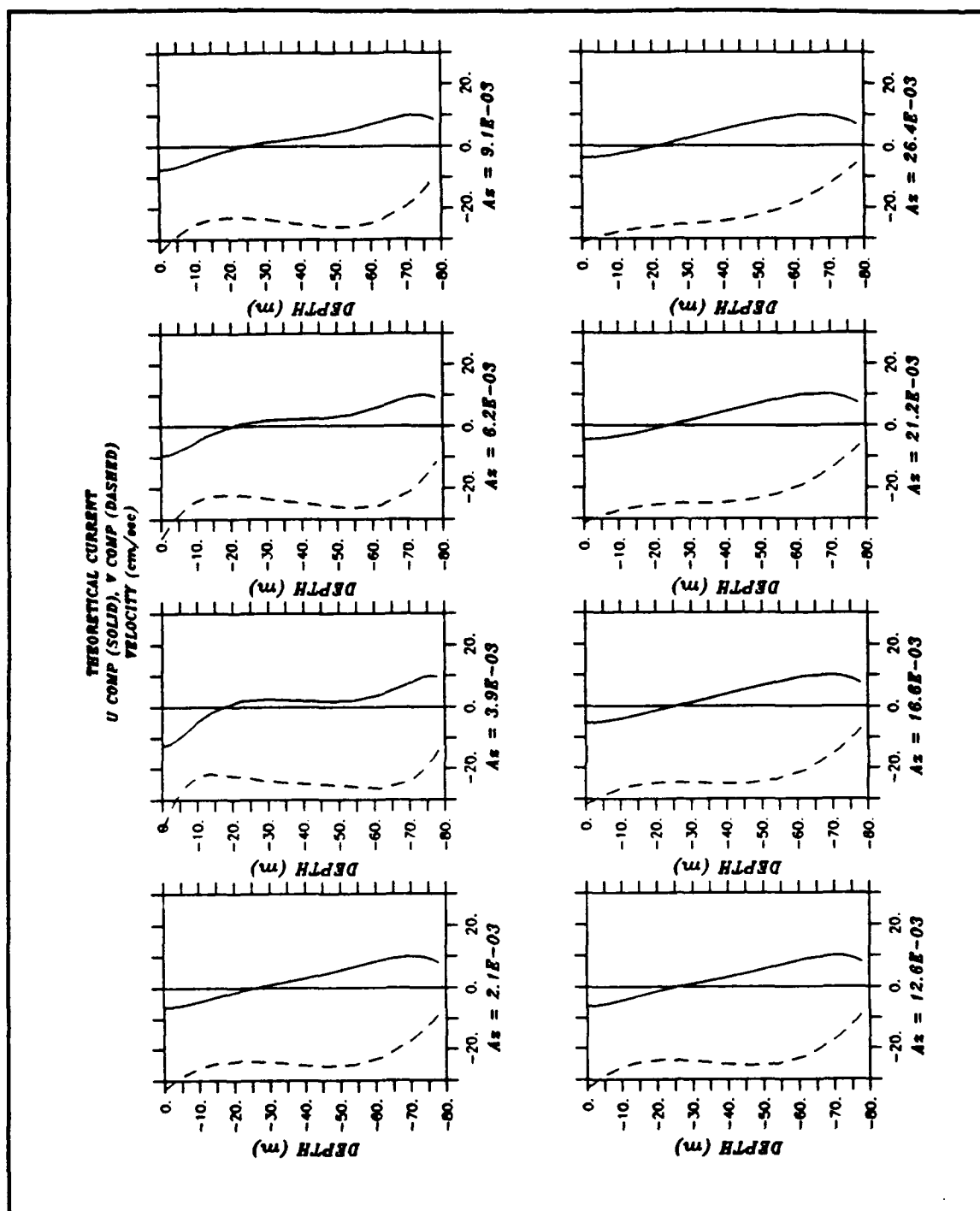


Figure 27. Solutions to governing equations utilizing variations of eddy viscosity ( $A_z$ ): Values of  $A_z$  are in  $m^2 s^{-1}$ . The  $u$  - component is represented by a solid line, the  $v$  component by a dashed line. Velocity is in  $cm s^{-1}$ .

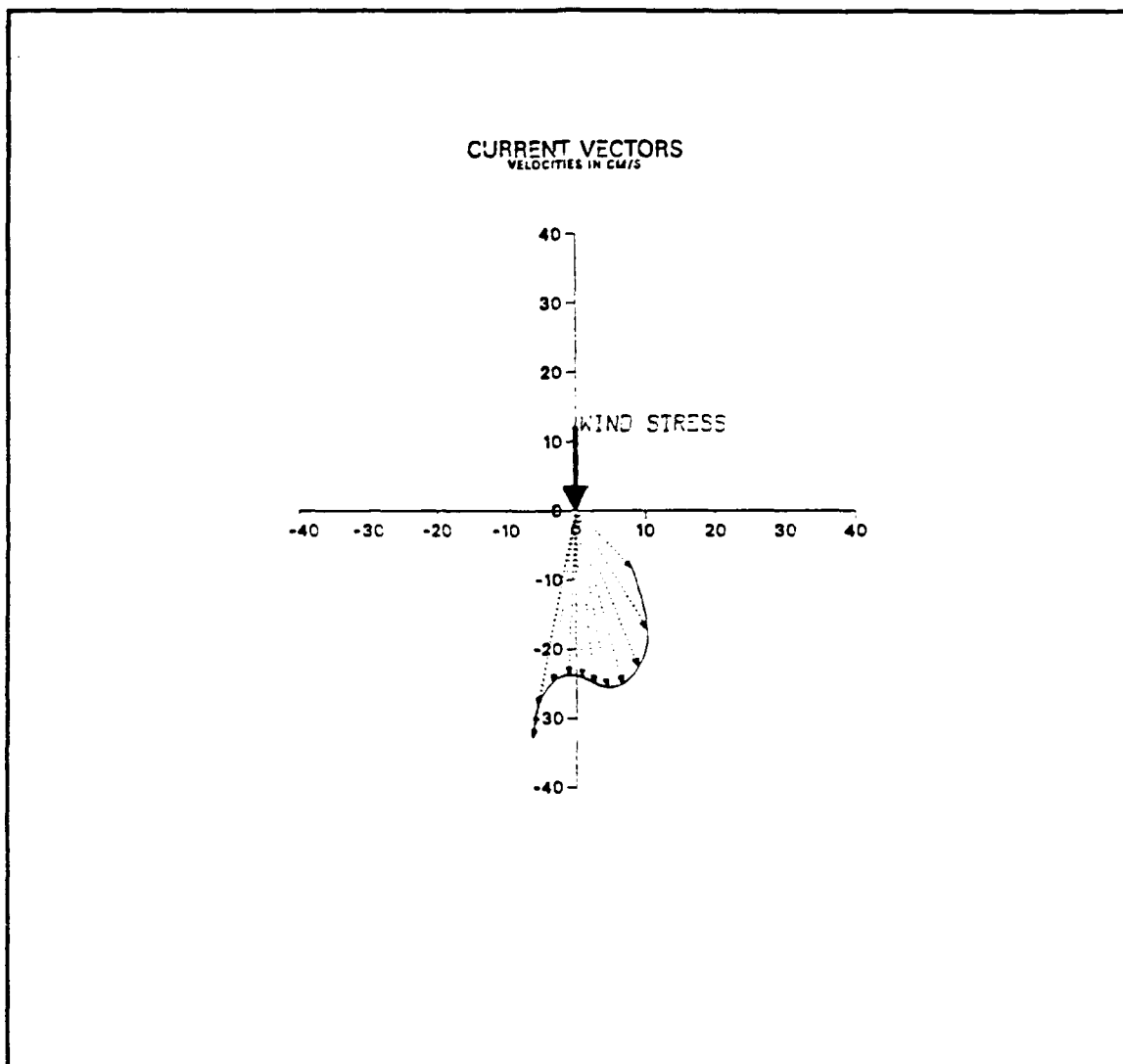
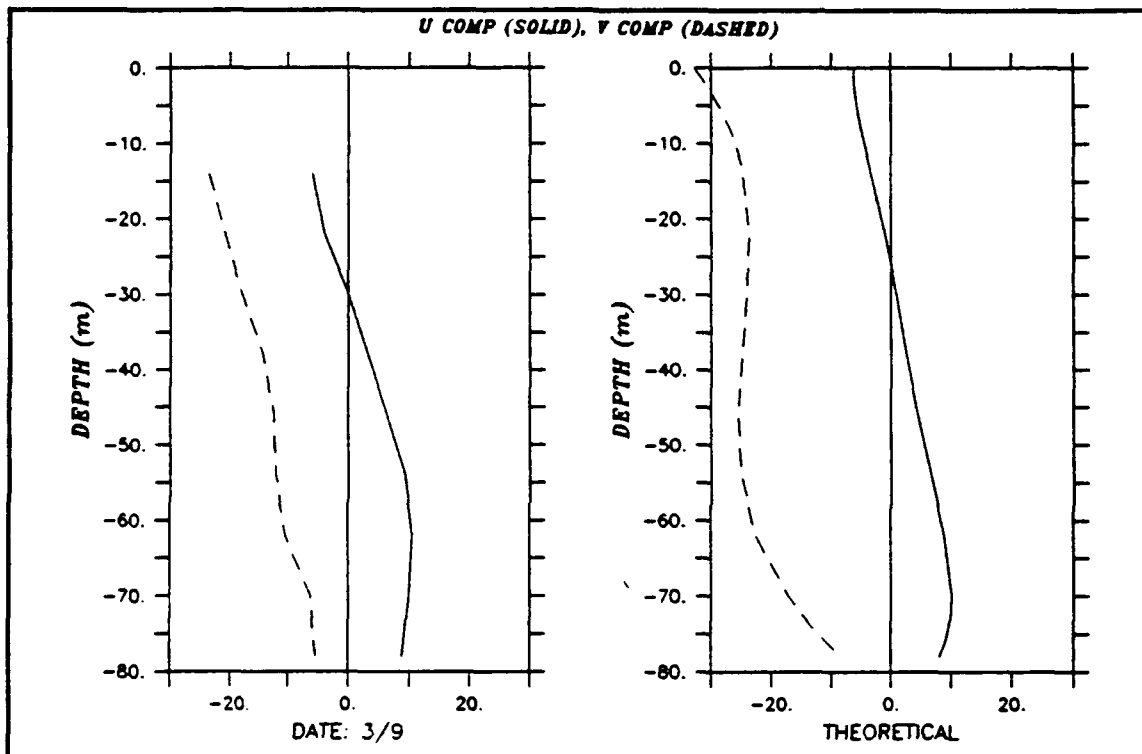


Figure 28. Theoretical current structure: The theoretical current is solved for based on inputs taken from 9 March observations utilizing a value for  $A_z = 12.6 \times 10^{-3} \text{ m}^2 \text{ s}^{-1}$ .

another. The current structure resembles Ekman's theoretical hodograph for a water depth =  $1.25 D$ , (Figure 23c) The plots of the theoretical and observed current for 9 March (Figure 29) indicate that the larger value of  $A_z$  provides a better approximation of the actual current. The transition depth and general shape of the  $u$  - component in the theoretical current is approximately the same as the observed current. The vertically integrated across-shore transport is not balanced, however, it is not used as a criteria for model comparison because: 1) it is quite sensitive to the choice of coordinate system, and 2) it is not clear that the observed across-shore transport should necessarily be balanced near a coastal promontory such as Point Sur. Cold upwelling filaments are often observed there (Breaker and Mooers, 1987) which presumably requires alongshore convergence or divergence and an associated across-shore transport. The theoretical  $v$  - component more closely resembles the profile of the observed current than the curve found using  $A_z = 4.5 \times 10^{-3}$ , but still exhibits less shear than the observed current.

Utilizing  $A_z = 12.6 \times 10^{-3} \text{ m}^2 \text{ s}^{-1}$  and taking the duration and magnitude of the wind stress from each of the four equatorward events as inputs to the governing equations, the other equatorward wind stress events were calculated (Figure 30). The general characteristics of each event are reproduced well. The nature of the theoretical plots is such that velocity components up to the surface are calculated. As a result the model not only depicts the current structure but also has a hindcast capability for filling in the missing data in the near surface bins. The accompanying hodographs of the theoretical and observed currents (Figure 31) also illustrate this capability. The model predicts surface values ranging from  $20 - 35 \text{ cm s}^{-1}$  for these wind events.



**Figure 29. Theoretical current vs observed current:** The theoretical current is based on inputs taken from the 9 March observations with an increased value for  $A_z = 12.6 \times 10^{-3} \text{ m}^2 \text{ s}^{-1}$  substituted and is compared with the observed current structure on the same date. The u component is represented by a solid line the v component by a dashed line. Theoretical current components are plotted from the surface to 80 m in 8 m increments.

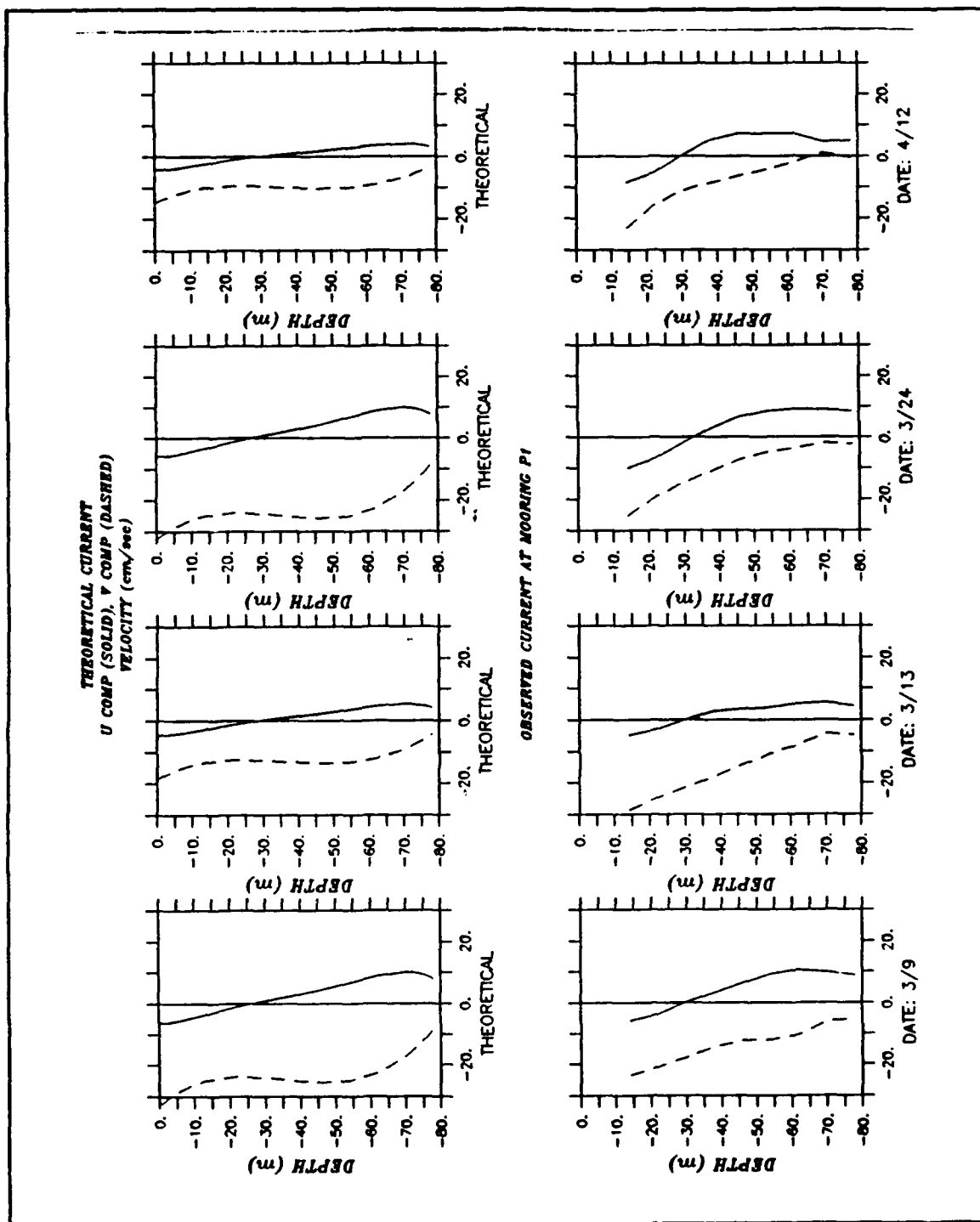


Figure 30. Theoretical current vs observed current: Theoretical current is based on inputs taken from the equatorward wind stress observations and compared with the observed current values from the same time frame. The u component is represented by a solid line the v component by a dashed line.

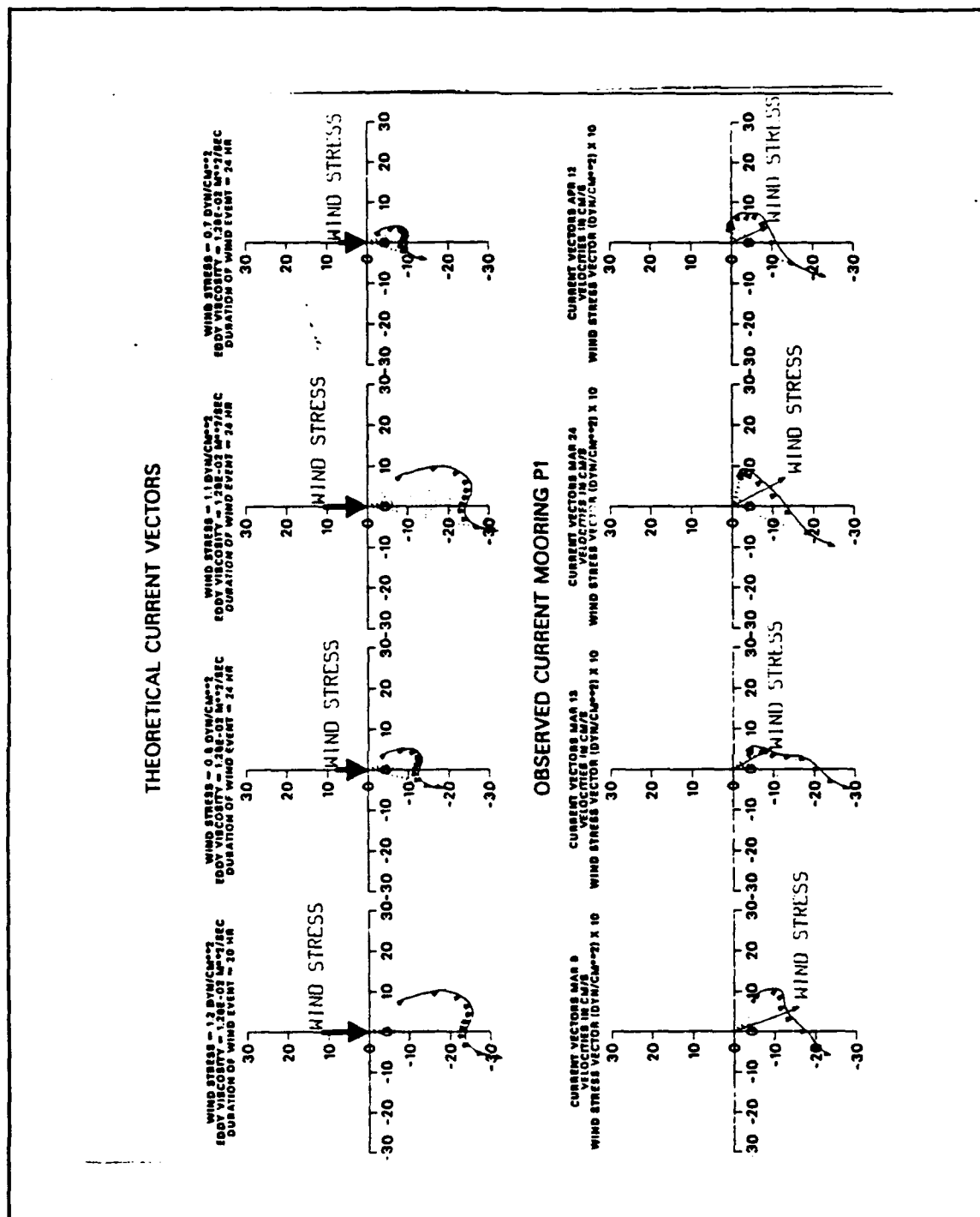


Figure 31. Theoretical current vs observed current hodographs: Theoretical current is based on inputs taken from the equatorward wind stress observations and compared with the observed current values in a series of hodographs from the same time frame.

## VII. DISCUSSION

### A. MODEL RESULTS

#### 1. Features

The simple wind driven coastal model reproduced the main features of the coastal current regime surprisingly well considering the complexity of the measurement site. It was particularly adept at describing the cross-shelf component of flow. The modeled transition from offshore to onshore flow occurred at approximately the 30 m level and the magnitude of the adjustment drift, at  $10 \text{ cm s}^{-1}$ , was very similar to the observations. The magnitude of the interior alongshore component was sensitive to the duration of the wind stress. Using  $t = 24 \text{ h}$  in the model produced surface ( $20 - 25 \text{ cm s}^{-1}$ ), and interior velocities that agreed with the observations. Beyond this, the surface stress was apparently balanced by the bottom stress and further accelerations did not occur. The interior portion of the  $v$  - component of the model was constant for all the equatorward wind events. Also, the constant magnitude interior flow was more pronounced when using smaller values of the wind stress. The sheared interior flow in the  $v$  - component could not be reproduced without using  $A_z$  coefficients that were too large to be realistic.

#### 2. Causative factors for observed model discrepancies

The discrepancies existing between model results and the observed current may possibly be due to variations in the assumptions utilized in deriving the governing equations of the model. Physical factors which were not included, but which may be important are discussed.



*a. Slight baroclinic effects and variable  $A_z$*

These two effects are actually interrelated. Slight stratification causes no appreciable difference from the homogeneous case (Neumann and Pierson, 1966). A well mixed upper layer over a strong thermocline responds differently, primarily due to a much greater  $A_z$  in the well mixed layer than in the stratified and lower layer below. In this case, the upper layer will "slide" over the lower layer, and the surface velocity and angle of deflection will be greater than in the unstratified case. No evidence was seen for this in early spring off Point Sur, and the assumption of a homogeneous ocean is believed to be good.

*b. Nonuniform wind stress*

The presence of spatial variability in alongshore forcing ( $\tau_y$ ) imply the assumptions made in equation (9.5)

$$\begin{aligned}F_x &= 0 \\F_y &= u_*^2\end{aligned}$$

and utilized in developing the interior current components along an infinitely long straight coast were not strictly valid. Alongshore variation in  $\tau_y$  will caused alongshore pressure gradients to develop and introduce varying  $v$  - component forcing ( $F_y \neq u_*^2$ ). These variations influence the observed current structure and cannot be reproduced by the simplified model. The effects of a non uniform-wind stress field will be discussed in detail in section B.

*c. Bathymetric considerations*

The continental shelf off Point Sur is neither straight or flat. The bottom depth shoaled to 55 m depth just 0.5 km to the southeast, in a rough-bottomed region known as "the rock pile." The bottom contours were not parallel to the coastline, making a choice of coordinate systems difficult. The

coordinate system was selected with  $u$  - east and  $v$  - north, recognizing that true "alongshore" flows, in the large-scale sense, would be partially mapped into the  $u$  - component. This affected the  $u$  and  $v$  - component plots but not the magnitude or sense of rotation of the hodographs. Across-shore transports were very sensitive to this problem and are not calculated. Considering the simplistic case of continental shelf bathymetry increasing with depth as a function of distance from the coast, the across-shore adjustment drift would also experience changes in vorticity not accounted for in the model.

*d. Remote influences*

The contributions of remote influences on the observed currents in the vicinity of Point Sur were not included in the model results. These influences include the presence of long, wind forced, coastal trapped waves propagating poleward along the shelf and slope; mesoscale variability over the shelf; and the presence of alongshore pressure gradients due to factors other than coastal trapped waves. A unique feature of these data relative to the CODE results is that most of the current variability can be accounted for via the local, rather than remote wind forcing. This is perhaps because the short record obtained from P1 lends itself to analysis of the higher wind-forced frequencies, which tend to be more locally forced (Denbo and Allen, 1987; Winant et al., 1987). There may also be a significant difference in the alongshore scales of the wind field between CODE and Point Sur regions. To be apparent, remote forcing must necessarily be occurring more than a coherence scale away from the observation site (Davis and Bogden, 1989). Off Point Sur, this coherence break in the wind field occurs at Point Conception, a sharp change in coastline orientation, which may also represent a dynamical break in the alongshore current structure as well.

Most of the mesoscale variability in the CCS is topographically constrained to the continental slope region and farther offshore, and does not impact the mid-shelf region. While there are exceptions (Lentz, 1987), mesoscale eddies were apparently not important during the short deployment of the SC-ADCP off Point Sur.

Other causes of alongshore pressure gradients include variability in the alongshore component of the wind stress, differential upper layer heating, and large-scale oceanic influences. These factors are discussed subsequently in connection with an anomalous equatorward wind event which did not elicit the expected response in the SC-ADCP currents.

## **B. ANOMALOUS EQUATORWARD WIND EVENTS**

To highlight the difficulty in modeling the current structure on the continental shelf using a simple wind forced model, this section focuses on the unusual response to an equatorward wind event during 24 April - 02 May. The magnitude of this event was about  $3.0 \text{ dyn cm}^{-2}$ , however, the current response was different from similar wind forced events observed elsewhere in the data set. To examine the respective current structures, enlarged stick vector plots for this event and an earlier equatorward wind event during 20 - 26 March are shown (Figure 32). The 20 - 26 March event has a large near surface magnitude (35 cm

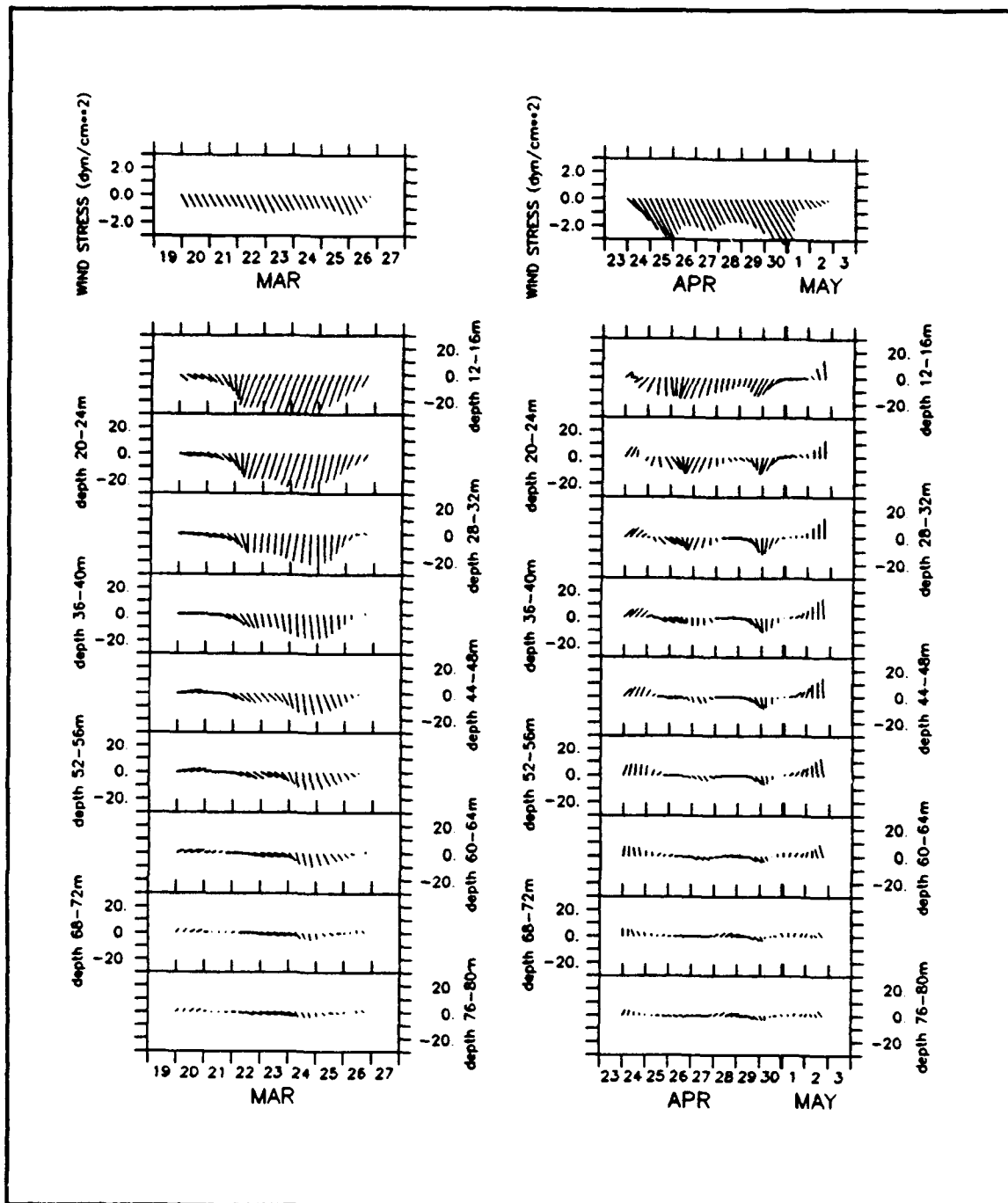


Figure 32. Time series showing equatorward wind stress events during 20 - 26 March and 24 April - 02 May: The vector direction and length correspond to current direction and magnitude respectively with north up. Velocities are in  $\text{cm s}^{-1}$ .

$\text{s}^{-1}$ ), and a highly sheared response, with the current magnitude decreasing to  $5 \text{ cm s}^{-1}$  at 76 - 80 m. The vertical structure is time-lagged with the surface currents leading the bottom current. In contrast, surface currents during the 24 April - 02 May event were  $15 \text{ cm s}^{-1}$  and did not penetrate beyond 60 - 64 m. Below this, currents were weak ( $10 \text{ cm s}^{-1}$ ) and variable, often near zero.

### **1. Poleward pressure gradient**

A poleward pressure gradient growing stronger with time is a possible mechanism to account for the lack of current response to the large equatorward wind event of 24 April - 02 May. To examine this hypothesis the difference in SSP between Monterey Bay and Port San Luis ( $\Delta\text{SSP}$ ) is presented along with the local wind stress data from the Monterey Bay buoy in Figure 33. A linear least squares fit to the  $\Delta\text{SSP}$  data is indicated by a dashed line. A trend of increasing  $\Delta\text{SSP}$  is observed over time. Of particular note is the large magnitude (+)  $\Delta\text{SSP}$  that occurs in conjunction with the equatorward wind event of 24 April - 02 May. The positive  $\Delta\text{SSP}$  indicates higher sea level at Port San Luis than at Monterey Bay. This infers a poleward pressure gradient which will oppose the equatorward alongshore wind stress.

### **2. Alongshore variability in the alongshore wind stress**

The observed increase in the poleward pressure gradient may be attributed to 1) alongshore variability in  $\tau_y$ , 2) greater upper layer heating to the south than the north as the spring season arrives, 3) the presence of coastal trapped waves at various frequencies. The anomalously large wind event of 24 April - 02 May suggest that this particular event may be related to a geographically localized synoptic scale event. If so, a large gradient in alongshore wind stress could be generated and subsequently contribute to the set-up

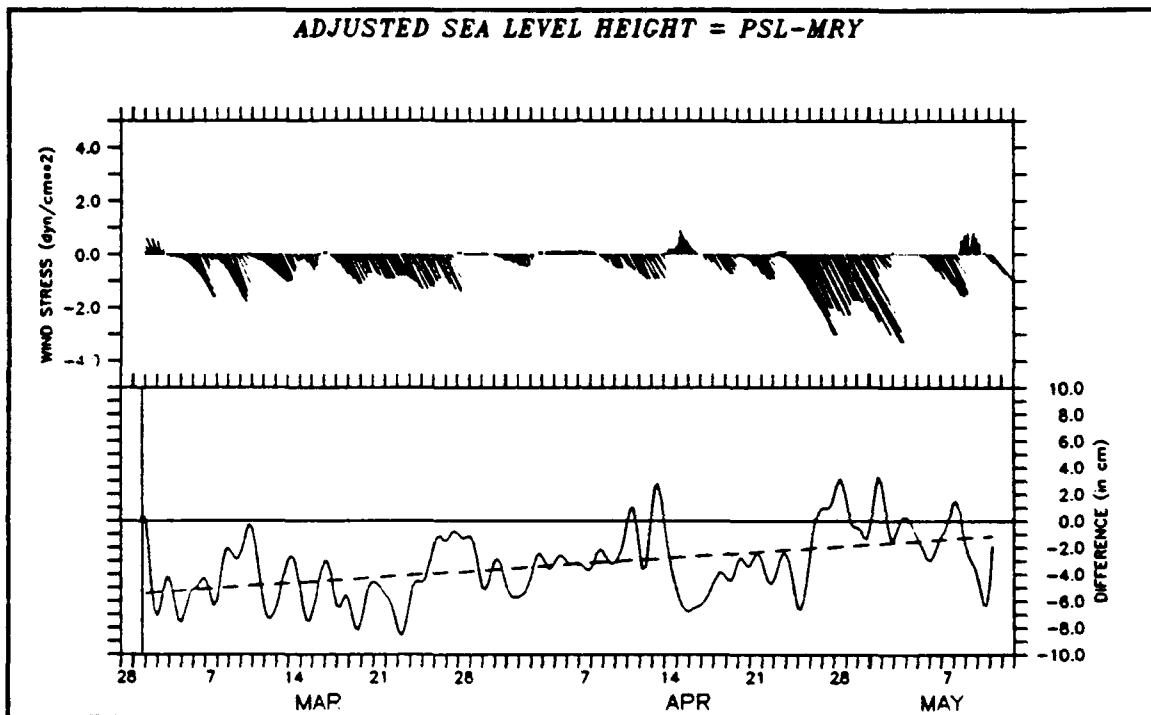


**Figure 33.  $\Delta\text{SSP}$  vs wind stress:**  $\Delta\text{SSP}$  is computed as the difference in SSP between Port San Luis (PSL) and Monterey Bay. Positive values indicate higher SSP at PSL. Differences are measured in cm.

of a poleward pressure gradient. This would violate one of the fundamental assumptions of the model, of constant alongshore wind stress, and would prohibit the model from reproducing the results.

Alongshore wind stress data from the Monterey Bay NOAA buoy and the Santa Maria NOAA buoy, located 200 km to the south near Port San Luis are presented in Figure 34. Taking the difference in  $\tau_y$  (Santa Maria - Monterey Bay) and superimposing  $\Delta SSP$  (Figure 35) shows that the greatest magnitude difference in  $\tau_y$  occurs in conjunction with the largest positive  $\Delta SSP$ , which supports the idea that the 24 April - 02 May wind event had a smaller alongshore extent than the earlier wind events. Other variations in  $\Delta SSP$ , including the increasing trend are unrelated to  $\frac{\partial \tau_y}{\partial y}$  and must be due to other processes.

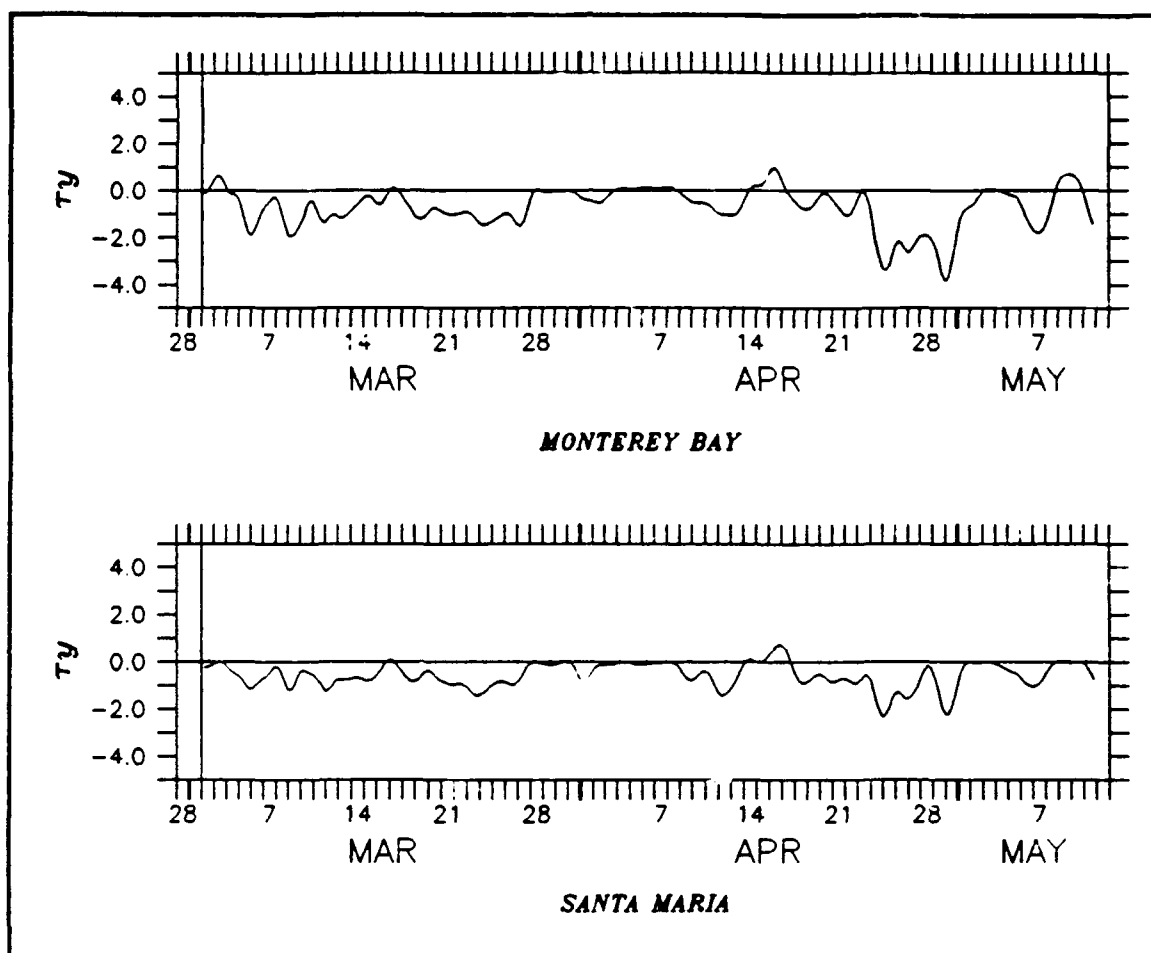
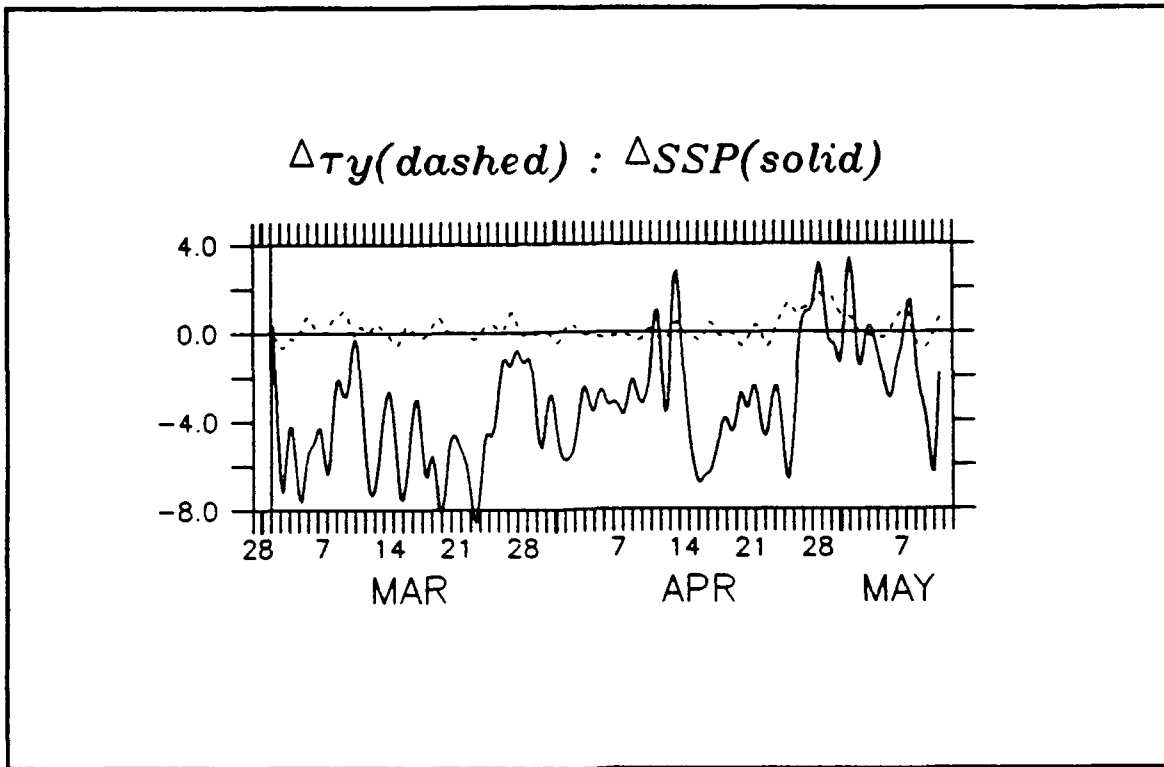


Figure 34. Alongshore component of the wind stress at Monterey Bay and the wind stress at Santa Maria: The wind stress is measured in  $\text{dyn cm}^{-2}$ .





**Figure 35.**  $\partial\tau_y/\partial y$  vs  $\Delta SSP$ :  $\partial\tau_y/\partial y$  is the difference between the alongshore component of the wind stress at Monterey Bay and at Santa Maria. Positive values indicate stronger wind stress at Monterey Bay.

## VIII. CONCLUSIONS AND RECOMMENDATIONS

### A. CONCLUSIONS

The purpose of this study was to observe the circulation on the continental shelf off Point Sur, California using a SC-ADCP. The SC-ADCP proved to be a reliable and accurate instrument for measuring current data. The instrument retrieved 100 percent of the available current data from deployment on 28 February through recovery on 11 May 1990.

The SC-ADCP was moored on the 84 m isobath with the transducer head at 80 m. The mooring was on a relatively flat area, however, a substantial rock pile shoaling to 55 m was 500 m to the southeast creating very complicated bathymetry. An ensemble of 170 one second pings were averaged every 15 minutes and recorded on a cassette tape. At a vertical resolution of 4 m, twenty depth bins were computed per ensemble. Prior to averaging, each ping was converted into earth coordinates thus producing three velocity components. The mooring geometry provided a stable platform for the SC-ADCP. As a result of negligible tilt, current data accuracies of  $0.5 - 1.0 \text{ cm s}^{-1}$  were attained to the near surface. Due to side lobe bias introduced at the near surface, the top 15 m of the current profile was discarded.

Low passed filtered data indicate high coherence between local wind forcing, taken from the Monterey Bay NOAA buoy, and current measured at the SC-ADCP. During equatorward wind events, current response was vertically sheared and lagged with near surface magnitudes up to  $35 \text{ cm s}^{-1}$ . A notable exception occurred late in the record when the largest magnitude wind event ( $3.0 \text{ dyn}$

$\text{cm}^{-2}$ ) failed to produce a comparable response in the water column. Analysis of the  $v$  - current component indicated a trend toward decreasing equatorward flow throughout the record. Adjusted sea level (ASL) differences suggested the trend may be due to a building poleward pressure gradient as evidenced by a higher ASL south of P1. Relaxations and wind reversals produced more barotropic poleward responses on the order of  $10 \text{ cm s}^{-1}$  in the water column. Possibly due to an increasing poleward pressure gradient, these responses are observed to increase in frequency and magnitude as the record progresses.

A simple wind forced theoretical model adapted from Ekman (1905) and Csanady (1982) was used to describe the flow in the coastal regime. The model consisted of surface and bottom boundary layers superimposed on a mostly geostrophic interior flow driven by set-up and set-down of the sea surface near the coast. Essential features of the model including the magnitude, direction, and sense of rotation of the current vectors with depth were reproduced well when forced by the actual surface wind stress and realistic vertical eddy coefficients.

Differences existing between model results and the observed current may possibly be due to variations in the assumptions utilized in deriving the governing equations of the model. Remote influences can also affect and influence the observed currents and thus not be reflected in the model results.

## **B. RECOMMENDATIONS**

This study utilized SC-ADCP data to describe the current structure of the flow along the central California continental shelf. The SC-ADCP at P1 provided exceptional temporal and vertically spatial coverage, however, at the expense of horizontal coverage. A better understanding of the horizontal spatial variability of the shelf flow could be obtained by mooring several SC-ADCPs on the

continental shelf or scheduling concurrent hydrographic and shipboard surveys in the vicinity of the mooring. It would also be useful to moor the instruments for more than four months, to compare the statistical confidence in the wind-forced events and allow the discrimination of lower frequencies. This would also allow a more rigorous analysis of remote forcing from the south. Additional measurements in other seasons would allow analysis of summer stratification, the fall transition, and the onset of winter cooling.

Regarding the positioning of the SC-ADCP for future deployments, consideration should be given to the alignment of the instrument along constant lines of latitude as done with established moorings P2 and P3. As the vertical structure of typical continental shelf currents is likely to change most rapidly in the across-shelf rather than the along-shelf direction (Beardsley and Lentz, 1987) the alignment of the instruments along the same latitude would aid in the analysis of the across-shelf variability in flow structure.

## REFERENCES

- Beardsley, R.C., and S.J. Lentz, The Coastal Ocean Dynamics Experiment Collection: an Introduction, *J. Geophys. Res.*, **89**, 1455-1463, 1987.
- Beardsley, R.C., C.E. Dorman, C.A. Friehe, L.K. Rosenfeld, and C.D. Winant, Local atmospheric forcing during the Coastal Oceans Dynamics Experiment 1. a description of the marine boundary layer and atmospheric conditions over a Northern California upwelling region, *J. Geophys. Res.*, **92**, 1467-1488, 1987.
- Bendat, J.S. and A.G. Piersol, *Random Data Analysis and Measurement Procedures*, 2nd Ed., John Wiley & Sons, Inc., N.Y., 566 pp., 1986.
- Breaker, L.C. and C.N. Mooers, Oceanic variability off the central California coast, *Prog. Oceanog.*, **17**, 61-135, 1986.
- Brink, K.H., The near-surface dynamics of coastal upwelling, *Prog Oceanog.*, **12**, 223-257, 1983.
- Brown, W.S., N.R. Pettigrew, and J.D. Irish, The Nantucket Shoals Flux Experiment (NFSE79). Part II: The structure and variability of across-shelf pressure gradients., *J. Phys. Oceanogr.*, **15**, 749-771, 1985.
- Chelton, D.B., Seasonal variability of alongshore geostrophic velocity off central California, *J. Geophys. Res.*, **89**, 3473-3486, 1984.
- Chelton, D.B., A.W. Bratkovich, R.L. Bernstein, and P. M. Kosro, Poleward flow off central California during the spring and summer of 1981 and 1984, *J. Geophys. Res.*, **93**, 10,604-10,620, 1988.
- Crépon, M., Hydrodynamique marine en regime impulsif, *Cah. Oceanogr.*, **19**, 847-880., 1967.
- Csanady, G.T., *Circulation in the Coastal Ocean*, D. Reidel Publishing Co., Dordrecht, Holland, 279 pp., 1982.
- Davis, R.E. and P.S. Bogden, Variability on the California shelf forced by local and remote winds during the Coastal Ocean Dynamics Experiment, *J. Geophys. Res.*, **94**, 4763-4783, 1989.

- Denbo, D.W., K. Lolain, J.S. Allen, A. Huyer, and R.L. Smith, Current meter observations over the continental shelf off Oregon and California February 1981 - January 1984, Data Report 112, Ref. 84-12, College of Oceanography, Oregon State University, Corvallis, Oregon, 1984.
- Denbo, D.W. and J.S. Allen, Large-scale response to atmospheric forcing of shelf currents and coastal sea level off the west coast of North America: May - July 1981 and 1982, *J. Geophys. Res.*, **92**, 1757-1782, 1987.
- Ekman, V.W., On the influences of the earth's rotation on ocean-currents, *R. Swedish Aca. of Sci.*, Vol. 2, No. 11, 1-53, 1905.
- Grant, W.D., A.J. Williams, III, S.M. Glenn, Bottom stress estimates and their prediction on the northern California continental shelf during CODE-1: the importance of wave-current interaction, *J. Phys. Oceanogr.*, **14**, 506-527, 1984.
- Halpern, D., Measurements of near-surface wind stress over an upwelling region near the Oregon coast, *J. Phys. Oceanogr.*, **6**, 108-112, 1976.
- Hickey, B.M., The California Current System - hypothesis and facts, *Prog. Oceanogr.*, **8**, 191-279, 1979.
- Huyer, A., Coastal upwelling in the California Current System, *Prog. Oceanogr.*, **12**, 259-284, 1983.
- Huyer, A., P.M. Kosro, J. Fleishbein, S. Ramp, T. Stanton, L. Washburn, F. Chavez, and T. Cowles, Currents and water masses of the coastal transition zone off northern California, June to August 1988, *J. Geophys. Res.*, **96**, 14,809-14,832, 1991.
- Johns, W.E., Near-surface current measurements in the Gulf Stream using an upward-looking Acoustic Doppler Current Profiler, *J. Atmos. and Ocean. Tech.*, **5**, 602-613, 1988.
- Kosro, P.M., Structure of the coastal current field off northern California during the Coastal Ocean Dynamics Experiment, *J. Geophys. Res.*, **92**, 1637-1654, 1987.
- Large, W.G., and S. Pond, Open ocean momentum flux measurements in moderate to strong winds, *J. Phys. Oceanogr.*, **11**, 324-326, 1981.
- Lentz, S.J., A heat budget for the northern California shelf during CODE 2, *J. Geophys. Res.*, **92**, 14491-14509, 1987.
- Lentz, S.J., and J.H. Trowbridge, The bottom boundary layer over the northern California shelf, *J. Phys. Oceanogr.*, **21**, 1186-1201, 1990.

- McCreary, J.P., P.K. Kundu, and Shenn-Yu Chao, On the dynamics of the California Current system, *J. Mar. Res.*, **45**, 1-32, 1987.
- Nelson, C.S., Wind stress and wind stress curl over the California Current, *Tech. Rep. NMFS-SSRF-714*, Nat. Oceanic and Atmos. Admin., Wash. D.C., 1977.
- Neumann, G., and W.J. Pierson, Jr., *Principals of Physical Oceanography*, Prentice-Hall, Inc., Englewood Cliffs, N.J. 545 pp., 1966.
- Pond, S., and G.L. Pickard, *Introductory Dynamical Oceanography*, 2nd Ed., Pergamon Press Inc., Elmsford, N.Y. 329 pp., 1983.
- Pettigrew, N.R., Direct measurements of the flow of western Mediterranean deep water over the Gibraltar sill, *J. Geophys. Res.*, **94**, 18,089-18,093, 1989.
- RD Instruments, *Acoustic Doppler Current Profilers Principals of Operation: A Practical Primer*, RD Instruments Inc., San Diego, Ca., 36 pp., 1989.
- Reid, J.L., G.I. Roden, and J.G. Wyllie, Studies of the California current system, *Calif. Coop. Oceanic Fish. Invest. Prog. Rep. 7-1-56 to 1-1-58*, Mar. Resour. Comm., Calif. Dep. of Fish and Game, Sacramento, Ca., pp. 27-56, 1958.
- Sielbeck, S.L., Bottom trapped waves at tidal frequencies off Point Sur California, Master's Thesis, Naval Postgraduate School, Monterey, California, 71 pp., 1990.
- Schott, F., Medium-range vertical acoustic Doppler current profiling from submerged buoys, *Deep-Sea Res.* **33**, 1279-1292, 1986.
- Schott, F., and W., Johns, Half-year-long measurements with a buoy mounted Acoustic Doppler Current Profiler in the Somali Current, *J. Geophys. Res.*, **92**, 5169-5176, 1987.
- Tisch, T.D., Seasonal variability of the geostrophic velocity and water mass structure off Point Sur, California, Master's Thesis, Naval Postgraduate School, Monterey, California, 148 pp., 1990.
- Telephone Conversation between T. Anderson, Naval Postgraduate School, Monterey, California and J. McNabb, RD Instruments Inc., San Diego, California, 24 September 1991.
- Wickham, J.B., A.A. Bird, and C.N.K. Moorers, Mean and variable flow over the central California continental margin, 1978 - 1980, *Cont. Shelf Res.*, **7**, 827-849, 1987.

Winant, C.D., R.,C, Beardsley, and R.E. Davis, Moored wind, temperature, and current observations made during Coastal Ocean Dynamics Experiments 1 and 2 over the northern California continental shelf and upper slope, *J. Geophys. Res.*, **92**, 1569-1604, 1987.



## INITIAL DISTRIBUTION LIST

	No. Copies
1. Defense Technical Information Center Cameron Station Alexandria, Virginia 22304-6145	2
2. Library, Code 52 Naval Postgraduate School Monterey, California 93943-5100	2
3. Chairman, (Code OC/Co) Department of Oceanography Naval Postgraduate School Monterey, California 93943-5100	1
4. Professor Steven R. Ramp, (OC/Ra) Department of Oceanography Naval Postgraduate School Monterey, California 93943-5100	1
5. Professor P.C. Chu, (OC/Cu) Department of Oceanography Naval Postgraduate School Monterey, California 93943-5100	1
6. LT Christopher L. Abbott NOCC/JTWC Guam PSC 489 FPO AP 96540-0051	1
7. Commander Naval Oceanography Command Stennis Space Center Mississippi 39529-5000	1
8. Dr T. Kinder Office of Naval Research Code 1122CS 800 N. Quincy Street Arlington, Virginia 22217	1